UNIVERSIDAD NACIONAL AUTÓNOMA DE MÉXICO
MAESTRÍA EN CIENCIAS (ASTROFÍSICA)

BAR PATTERN SPEED ESTIMATES USING THE TREMAINE-WEINBERG METHOD IN MaNGA GALAXIES

TESIS

QUE PARA OPTAR POR EL GRADO DE:
MAESTRO EN CIENCIAS (ASTROFÍSICA)

PRESENTA:
LUIS ALBERTO GARMA OEHMICHEN

DIRECTOR DE TESIS:
HÉCTOR MANUEL HERNÁNDEZ TOLEDO
INSTITUTO DE ASTRONOMÍA - UNAM

CIUDAD UNIVERSITARIA CD. MX., JULIO, 2018

Dedico esta tesis a la Universidad Nacional Autónoma de México, al Instituto de Astronomía y a la Facultad de Ciencias por la formación que me han dado. A mi tutor Héctor Hernández, por guiarme y asesorarme en todo momento. A Mariana Cano, Ocatavio Valenzuela y Erik Aquino, por las valiosas reuniones de trabajo. A mis padres Cristina y Carlos, por apoyarme toda la vida. A mi novia Amairani, por motivarme siempre a ser mejor persona. A todas mis amistades, por el camino que hemos recorrido juntos

Es gracias a ustedes que es posible el presente trabajo.
Gracias.

Declaración de autenticidad

Por la presente declaro que, salvo cuando se haga referencia específica al trabajo de otras personas, el contenido de esta tesis es original y no se ha presentado total o parcialmente para su consideración para cualquier otro título o grado en esta o cualquier otra Universidad. Esta tesis es resultado de mi propio trabajo y no incluye nada que sea el resultado de algún trabajo realizado en colaboración, salvo que se indique específicamente en el texto.

Luis Alberto Garma Oehmichen. Ciudad de México, 2018

Resumen

The difficulty to measure the bar pattern speed (Ω_{bar}), has been one of the main challenges for understanding the role of stellar bars in the galaxies dynamical evolution. Based on the continuity equation, the Tremaine & Weinberg (1984) (hereafter TW) method is the only direct method to measure Ω_{bar}. In recent years, the number of galaxies analysed with the TW method has increased dramatically, thanks to the arrive of Integral Field Spectroscopic surveys. In this thesis, we used the TW method in a sample of 15 MaNGA galaxies and re-analyse 3 CALIFA galaxies (Aguerri et al., 2015) in order to find systematic errors in our methodology. Since it is known that an important uncertainty in the TW method come form the position angle (PA) estimates, we used both a photometric PA from an isophote analysis to the SDSS r-band images, and a kinematic PA from the stellar velocity maps. In cases where the difference between both PA's is significant, we discuss the possible origin. Additionally, we identified and discuss two more sources of error: The pseudo-slits length error, and the centering error that also arise from the geometric nature of the method. We measure from the stellar velocity field the rotation curves using *velfit* which is able to model the non-axisymmetric motions produced by the bar Spekkens & Sellwood (2007). Comparing Ω_{bar} with the angular velocity curve we measure the corotation radius and the parameter $\mathcal{R}$, defined as the ratio between corotation and the bar radii. We identified 1 slow, 9 fast and 8 ultra-fast rotating bars, and did not find at this level a trend with their morpholgical type. However, these numbers may change given the quoted uncertainties. We also observe a trend where Ω_{bar} decreases as the bar length increases, independently of how bars were classified. Our result are in agreement with previous results, suggesting that bars form as fast rotators.

La dificultad para medir la velocidad de patrón de barra (Ω_{bar}) a sido uno de los principales desafíos para un mejor entendimiento del papel de las barras en la evolución dinámica de las galaxias. Basado en la ecuación de continuidad, el método de Tremaine & Weinberg (1984) (TW) es el único método directo para medir Ω_{bar}. En años recientes, el número de galaxias analizados con el método de TW ha incrementado dramaticamente, gracias a la llegada de catastros con Espectroscopía Integral de Campo. En ésta tesis utilizamos el método de TW en una muestra de 15 galaxias de MaNGA y re-analizamos 3 galaxias de CALIFA (Aguerri et al., 2015) para encontrar errores sistemáticos en nuestra metodología. El método es bien conocido por sus incertidumbres con el ángulo de posición (PA), por lo que utilizamos un PA fotométrico proveniente de un análisis de isofotas en imagenes en la banda r de SDSS, y un PA cinemático obtenido de los mapas de velocidad estelar. Adicionalmente, identificamos y discutimos otras dos fuentes de error: el error por longitud de pseudo-rendija, y el error de centrado que también surgen de la naturaleza geométrica del método. Medimos las curvas de rotación estelar usando *velfit* que es capáz de modelar los movimientos no-axisimétricos producidos por la barra (Spekkens & Sellwood, 2007). Comparando Ω_{bar} con la curva de velocidad angular, medimos el radio de corrotación y el parametro $\mathfrak{R}$, definido como la razón entre el radio de corrotación y el radio de la barra. En nuestra muestra encontramos 1 barra lenta, 9 rápidas y 8 ultra rápidas, y no observamos ninguna tendencia con el tipo morfológico. Sin embargo, estos números pueden cambiar debido a la incertidumbres citadas. También observamos que Ω_{bar} disminuye conforme la longitud de la barra aumenta, independientemente de como hayan sido clasificadas. Nuestros resultados concuerdan con observaciones previas sugiriendo que las barras se forman como rotores rápidos.

Glossary

Ω_{bar}	Bar pattern speed
TW	Tremaine - Weinberg method: Used to determine the bar pattern speed
PA	Position Angle: Angle measured relative to the north celestial pole
PA_{ph}	Photometric position angle
PA_{kn}	Kinematic position angle
LOS	Line of sight
KI	Kinematic integral: The LOS velocity weighted by the surface brightness integral of the TW method
PI	Photometric integral: The position weighted by the surface brightness ingtegral of the TW method
IFS	Integral Field Spectroscopy: An observational technique used to acquire spectra of a 2-dimensional region of the sky.
IFU	Integral Field Unit: Instrument used to divide the sky plane into a continuous arrayor cells
SDSS	Sloan Digital Sky Survey
MaNGA	Mapping Nearby Galaxies at Apache Point Observatory
CALIFA	Calar Alto Legacy Integral Field Area Survey
LOS	Line of sight
ZVL	Zero velocity line
V_{sys}	Systemic velocity
ϵ	Elipticity

R_{CR}	Corrotation Radius: Radius where the bar pattern speed equals the disc angular velocity
$\mathrm{R}_{bar,1}$	Bar radius measured with the isophote with maximum ellipticity
$\mathrm{R}_{bar,2}$	Bar radius measured with the isophote where the PA has changed 5° with respect $\mathrm{R}_{bar,1}$
$\mathrm{R}_{bar,1}^{dep}$	Deprojected value of $\mathrm{R}_{bar,1}$
$\mathrm{R}_{bar,2}^{dep}$	Deprojected value of $\mathrm{R}_{bar,2}$
$\mathcal{R}$	Adimensional parameter used to classify the bar as a slow, fast or ultra fast rotator
PDF	Probability distribution function
$\delta\Omega_{Cen}$	Centering error
$\delta\Omega_{PA}$	Position angle error
$\delta\Omega_{Len}$	Pseudo slit length error
L_0	Maximum pseudo slit length that can be fitted inside the MaNGA or CALIFA hexagon while preserving the symmetry
$\Omega_{bar,0}$	Bar pattern speed measured using the maximum pseudo slit length L_0

Índice general

Capítulo 1

Introduction

1.1. Galaxy morphological classification

The most common way to classify galaxies is by their morphology [1] in three groups: Elipticals (E), Spirals (S) and Irregulars (Irr) (Hubble, 1926). Elliptical and lenticular galaxies are usually called “early”type galaxies while spiral and irregular are called “late”type. This nomenclature was used by Hubble to refer to their position in his fork diagram as can be seen in figure 1, and not their evolutionary stage.

1.1.1. Early type galaxies

The fraction of elliptical galaxies in the local universe is $\sim 10\,\%$ in low density regions and raises to $\sim 40\,\%$ in the center of galaxies clusters (Binney & Tremaine, 2008). Their light is distributed smoothly and do not present much substructure, so it is difficult to determine where they end. Elliptical galaxies are mostly composed by old stars, given them their yellowish color. They are also classed by their ellipticity, where an E0 is almost circular and E7 is the most flattened. They are mostly supported by their stellar random motions.

Lenticular galaxies are usually treated as an intermediate between spiral and elliptical galaxies. Just like ellipticals, they are composed mostly by old stars and dust, however they are supported by more ordered stellar motions. Like spirals, lenticular galaxies have a stellar disc, a bulge and sometimes a bar, however they lack spiral arms. They are rare in low density environments, but compose roughly half of the galaxies in clusters (Binney & Tremaine, 2008). In the Hubble classification scheme they are called S0 or SB0 if they present a bar. For a review in the properties of lenticular galaxies see: Aguerri et al. (2005).

A common problem when classifying early type galaxies are the projection effects.

---

[1] However, galaxies can also be classified by their star formation rate, nuclear activity, their position in the color-magnitude diagram, stellar angular momentum, environment, etc

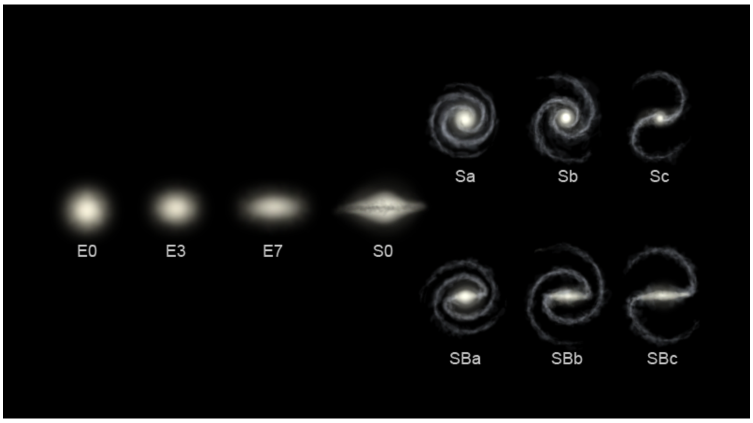

Figure 1: Hubble fork diagram. Early type galaxies can be found at the left of the diagram, while late types are located at the right

Face-on lenticular galaxies are pretty similar to elliptical galaxies. However, in recent years, these galaxies have been reclassified in two families: Slow Rotators and Fast Rotators. The first exhibit complex velocity fields, are relatively round, tend to be more massive, gas poor and metal rich. The Fast Rotators on the other hand, exhibit regular velocity fields, are more gas rich and still star forming Cappellari et al. (2007); Emsellem et al. (2011).

1.1.2. Spiral galaxies

The Spiral galaxy fraction is roughly $\sim 60\,\%$ in low density regions and decrees to $\sim 10\,\%$ in clusters (Binney & Tremaine, 2008). They can be described by 4 basic components. The first one is the disc, composed by stars, gas and dust rotating around the galaxy at velocities between 100 and 300 kms^{-1}. The disc can also host spiral arms, that are constantly forming new stars. The second component is the bulge at the center with a great concentration of old stellar populations. The third is an stellar halo, also composed mostly of old stars. Finally the dark matter halo given by the mass growth history of the galaxy.

In contrast with Elliptic galaxies, Spirals are continually forming young stars in the disc, given then their characteristic blue color. In the Hubble classification scheme, they are named S or SB if they contain a bar. Depending on how tightly wound the spiral arms are, a lower case letter is added (a, b, c or d) where a is the more tightly wound and d are very loosely wound.

1.1.3. Irregular galaxies

Irrgular galaxies are the ones that do not fit in the other classifications. Advancing in the spiral sequence Sa $\rightarrow$ Sd galaxies become less massive, less bright and lose their spiral structure (Binney & Tremaine, 2008). In irregular galaxies, gas dominates in mass, there is no spiral arm structure and the bulge is not centred.

1.2. Stellar bars

Bars are one of the most common stellar structures present in the central region of disc galaxies. Almost one third of nearby galaxies host bars larger than 4 kpc (Sellwood & Wilkinson, 1993; Menéndez-Delmestre et al., 2007). Small nuclear bars are usually hidden behind dust, so they are best seen in near-infrared where the bar fraction increases to $\sim 70\,\%$ (Eskridge et al., 2000; Whyte et al., 2002; Marinova & Jogee, 2007). The bar fraction is strongly dependent on the galaxy mass (or luminosity) (Méndez-Abreu et al., 2012; Erwin, 2018). Is not clear if this fraction remains constant (Jogee et al., 2004; Elmegreen et al., 2004) or decreases towards higher redshifts (Sheth et al., 2008; Melvin et al., 2014). Unlike the disc, where the stellar orbits are mostly circular, inside the bar region they become highly elongated and aligned with the rotating major axis. (Contopoulos & Papayannopoulos, 1980; Teuben & Sanders, 1985).

The presence of a bar highly influences the galaxy dynamics and secular evolution, promoting the redistribution of angular momentum, energy and mass between other galaxy components, such as the disk, the bulge and the dark matter halo. (Weinberg, 1985; Debattista & Sellwood, 1998; Athanassoula, 2003; Kormendy & Kennicutt, 2004; Sellwood, 2014). Some bar effects include the formation resonance rings (Schwarz, 1981; Buta & Combes, 1996; Rautiainen & Salo, 2000; Buta, 2017), gas inflow triggering star formation in the central regions(Hernquist & Mihos, 1995; Martinet & Friedli, 1997), and possibly fueling the active galactic nucleus (Laine et al., 2002). The bar itself evolves by buckling in the vertical direction (Martinez-Valpuesta et al., 2006) and by decelerating as its angular rotation rate becoming longer, stronger and slower (Martinez-Valpuesta et al., 2006).

Bars can be fully characterized by three observational parameters: the length, the strength and the pattern speed. The bar length R_{bar} can be estimated with a visual inspection (Martin, 1995), locating the maximum ellipticity in an isophote analysis of the galaxy (Wozniak et al., 1995; Laine et al., 2002; Marinova & Jogee, 2007), measuring the radius where the isophotoal position angle (hereafter PA) changes by $\Delta PA = 5°$ (Sheth et al., 2003; Erwin, 2005; Aguerri et al., 2009) or by Fourier decomposition of the surface brightness distribution (Ohta et al., 1990; Aguerri et al., 2000, 2003; Laurikainen et al., 2005).

The bar strength quantifies the influence of the bar in the galactic potential. It can be calculated using the bar ellipticity (Athanassoula, 1992; Abraham & Merrifield, 2000), estimating the bar torques (Buta & Block, 2001; Laurikainen & Salo, 2002), or by Fourier decomposition of the light (Aguerri et al., 2000; Laurikainen et al., 2005).

The pattern speed Ω_{bar}, defines how fast the bar rotates. In principle, Ω_{bar} has a physical upper limit. Studies of stellar orbits in barred potentials, show that self-consistent bars cannot extend outside the corotation resonance radius R_{CR} (i.e. the radius where the angular speed of the disc equals the bar pattern speed), since the stellar orbits become elongated perpendicular to the bar. In addition, the increasing density of resonances near corotation leads to chaos in phase space (Contopoulos & Papayannopoulos, 1980). The pattern speed is often parametrized with the dimensionless parameter $\mathcal{R} = \mathrm{R}_{CR}/\mathrm{R}_{bar}$. Since R_{CR} is the natural upper bound for R_{bar}, bars with $\mathcal{R}$ close to unity rotate as fast as nature allows. By convention, bars are defined as "fast" if $\mathcal{R} < 1.4$ and "slow" if $\mathcal{R} > 1.4$. Given the difficulties for measuring R_{bar} and Ω_{bar}, estimates of $\mathcal{R}$ are plagued by uncertainties. However, the vast majority of galaxies appear to be fast (Rautiainen et al., 2008; Corsini, 2011; Aguerri et al., 2015).

Several model-dependent methods have been developed to determine the bar pattern speed. Hydrodynamical simulations of individual galaxies can recover Ω_{bar} by matching the modeled and observed gas distribution and/or gas velocity field (Sanders & Tubbs, 1980; Hunter et al., 1988; Lindblad & Kristen, 1996; Rautiainen et al., 2008). The gravitational torque produced by the rotating bar causes gas to flow in the radial direction and accumulate in major resonances where the net torque vanishes (Buta & Combes, 1996). This has led to methods that rely on morphological features such as spiral arms (Puerari & Dottori, 1997; Aguerri et al., 1998), rings (Schwarz, 1981; Rautiainen & Salo, 2000; Patsis et al., 2003), or leading dust lanes(Athanassoula, 1992; Sánchez-Menguiano et al., 2015). Another approach is to measure directly the corotation radius by looking for a change of sign in the streaming motions of the gas (Font et al., 2011, 2017)

The only model-independent method for estimating Ω_{bar} is the so called Tremaine-Weinberg method (hereafter TW) from observations of a tracer which obeys the continuity equation (Tremaine & Weinberg, 1984). The stellar light distribution obeys the continuity equation, and thus, the TW method has been mostly used in early-type barred galaxies which are not obscured by the dust and have no star formation (Kent, 1987; Merrifield & Kuijken, 1995; Gerssen et al., 1999; Debattista et al., 2002; Aguerri et al., 2003; Corsini et al., 2003; Debattista & Williams, 2004; Corsini et al., 2007; Aguerri et al., 2015). Other tracers that have been used for the TW method are the mass distribution (Gerssen & Debattista, 2007; Aguerri et al., 2015) and gas tracers such as CO (Zimmer et al., 2004; Rand & Wallin, 2004) and Hα (Hernandez et al., 2005; Emsellem et al., 2006; Fathi et al., 2007; Chemin & Hernandez, 2009; Gabbasov et al., 2009; Fathi et al., 2009).

1.3. The Tremaine Weinberg method

The TW method requires a tracer that satisfies the continuity equation, like the stellar population within the galaxy or the mass distribution. Assuming the disc of the galaxy is flat and has a well-defined pattern speed Ω_{bar} the TW equation is:

$$\Omega_{bar} \sin i = \frac{\int_{-\infty}^{\infty} h(Y) \int_{-\infty}^{\infty} \Sigma(X,Y) V_{\parallel}(X,Y) \mathrm{d}X \mathrm{d}Y}{\int_{-\infty}^{\infty} h(Y) \int_{-\infty}^{\infty} X \Sigma(X,Y) \mathrm{d}X \mathrm{d}Y} \tag{1.1}$$

where i is the galaxy inclination, (X, Y) are the Cartesian coordinates in the sky plane, with the origin at the galaxy center, and the X-axis aligned with the line of nodes, which is defined as the intersection between the sky plane and the disc plane (i.e. disc major axis or disc PA). $\Sigma(X, Y)$ and $V_{\|}(X, Y)$ are the surface brightness and the line of sight (LOS) velocity of the tracer respectively. $h(Y)$ is an arbitrary weight function, that is usually given by a delta function $\delta(Y - Y_0)$, that corresponds to a slit in long-slit spectroscopy. For integral-field spectroscopy we can use the same weight function and refer to it as a pseudo-slit.

Merrifield & Kuijken (1995), noted that the integrals in equation 1.1 could be interpreted as luminosity-weighted means of the LOS velocity and position, so they normalized both integrals by total luminosity of the slit. In this sense, the integrals could be calculated at any reference frame, particularly in the galaxy center rest frame.

$$\Omega_{bar} \sin i = \frac{\langle V \rangle}{\langle X \rangle} \tag{1.2}$$

$$\langle V \rangle = \frac{\int_{-\infty}^{\infty} h(Y) \mathrm{d}Y \int_{-\infty}^{\infty} \Sigma(X, Y)(V_{\|} - V_{syst})(X, Y) \mathrm{d}X}{\int_{-\infty}^{\infty} h(Y) \mathrm{d}Y \int_{-\infty}^{\infty} \Sigma(X, Y) \mathrm{d}X} \tag{1.3}$$

$$\langle X \rangle = \frac{\int_{-\infty}^{\infty} h(Y) \mathrm{d}Y \int_{-\infty}^{\infty} X \Sigma(X, Y) \mathrm{d}X}{\int_{-\infty}^{\infty} h(Y) \mathrm{d}Y \int_{-\infty}^{\infty} \Sigma(X, Y) \mathrm{d}X} \tag{1.4}$$

We will refer to equation 1.3 as the kinematic integral (KI) and equation 1.4 as the photometric integral (PI). Plotting both integrals for several pseudo-slits produces a straight line with slope $\Omega_{bar} \sin i$.

Nevertheless, the TW method has some limitations and cannot be applied to all bared galaxies. For instance, in face-on galaxies the kinematic information tends to be poor, since the LOS velocities are closer to zero. On the other hand, for edge-on galaxies the photometric information is lost. The orientation of the bar should also be taken into account. If the bar is oriented towards the galaxy's minor or major axis both integrals tend to cancel out.

Although these integrals should be performed form $-\infty$ to ∞, they can be limited to X_{max} and Y_{max} if the axi-symmetric part of the disc is reached. Note however, that the axi-symmetric contribution of the disc to these integrals cancels out only if the slits are correctly aligned with the disc major axis. The sensibility of the TW method to the errors in the PA of the disc was first described by Debattista (2003), showing that in N-body simulations an error of 5° can produce errors as big as 50 % in Ω_{bar}. Figure 2 shows a simplified example of the method being applied to an ideal barred galaxy, but illustrates why errors associated with the disc PA tend to produce such big errors. Using a second estimation for the disc PA, coming from the galaxy kinematics could help constrain the errors. The geometric nature of the TW method leaves open the question if there are other important sources of error that have not been fully considered. In this work we paid special attention to two more sources of geometric error: the centering error and the pseudo-slit length error. In Chapter 4 we will see these errors can be as important as the PA error.

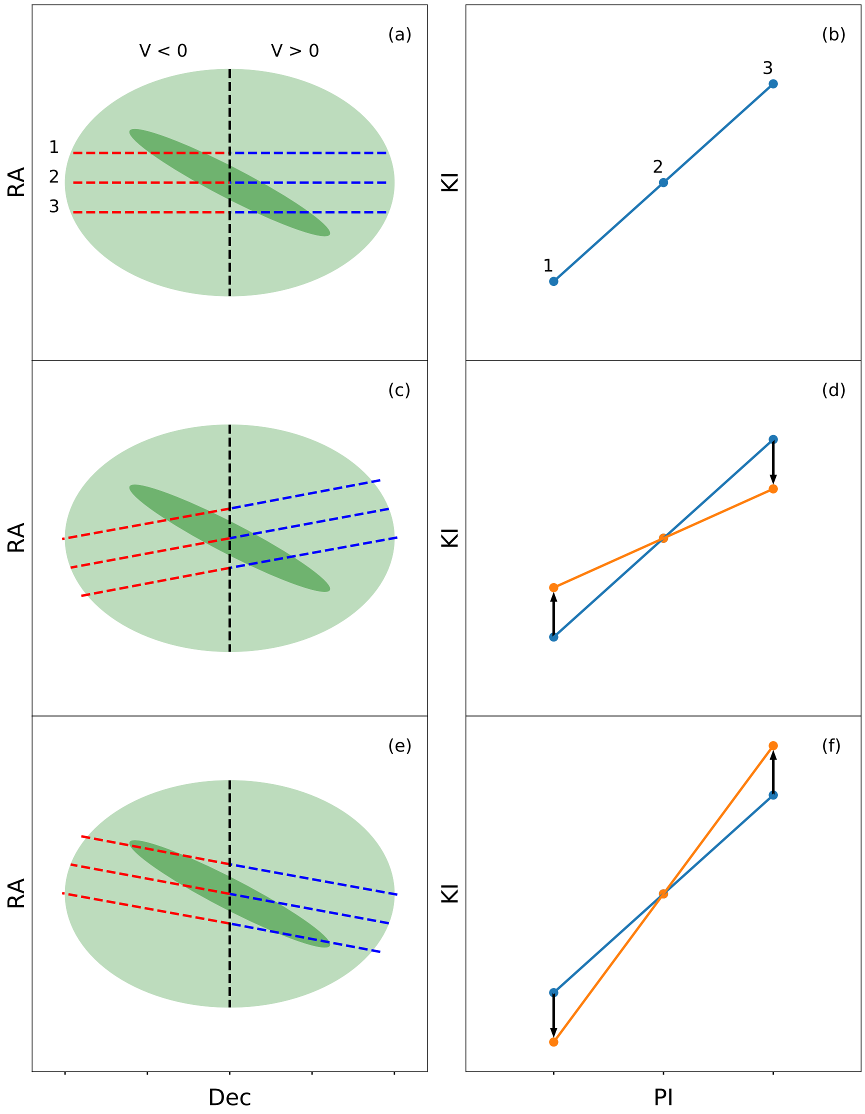

Figure 2: How the PA error arises. **(a)** A simplified inclined barred galaxy at its rest frame. The bar is denoted with a green ellipse. The LOS velocity is chosen to be negative on the left side and positive on the right side. 3 pseudo-slits are aligned with the major axis for the TW method. **(b)** The TW light-weighted integrals are plotted for each pseudo-slit. The symmetry of the integrals cancels out the axi-symmetric disc contribution. The resulting slope is $\Omega_{bar} \times \sin i$. **(c)** In this case, the pseudo-slits are not aligned correctly and the axi-symmetric contribution of the disc is no longer cancelled. The first pseudo-slit now weights more light from the negative velocity side. The opposite happens with the third slit. **(d)** The fictitious pattern speed produced by the disc affects the measurement of of Ω_{bar}. **(e)** Same as (c), but the PA error is oriented in the opposite direction. **(f)** Same as (d), but this time the first pseudo-slit weights more the positive velocity side. In general, the PA error is not symmetrical and is highly galaxy dependent.

1.4. Integral Field Spectroscopy, the MaNGA and the CALIFA surveys

Traditionally astronomical observation were done in two different ways. Photometry imaging using astronomical filters, or spectroscopy using optical fibers, or long slits. Both techniques have their own advantages but are mutually exclusive: Photometry images do not contain spectroscopic information and spectroscopy losses almost all spatial information.

In the last years a new observational technique called “Integral Field Spectroscopy” (IFS) has been proliferating, as it allows to study the spectra of a 2-dimensional region of the sky. The resulting data is a “data cube”, with 2 spatial dimensions and one spectral dimension (x, y, λ). To highlight its three-dimensional nature, the pixels in these images are called “spaxels” (spatial + pixel). An integral field spectrograph is composed of two parts: a spectrometer and an integral field unit (IFU) that divides the sky plane into a continuous array.

The power of spatially resolved spectroscopy has motivated various projects and surveys in the extragalactic astronomy community. Each one with different objectives and technical details. In this thesis we used data obtained from two surveys: The Mapping Nearby Galaxies at Apache Point Observatory (MaNGA) and the Calar Alto Legacy Integral Field Area Survey (CALIFA).

Both of these projects use a fiber-bundle IFU, consisting of optical fibers packed together in an hexagonal array. Because of the gaps between fibers, a continuous sample of the sky is not possible. To solve this problem, both surveys use a technique called ”dithering”, where the array is displaced after some integration time to cover the gaps that where not observed (Barden & Wade, 1988).

1.5. The MaNGA survey

MaNGA is one of the three core programs of the Sloan Digital Sky Survey IV (SDSS -IV) project (Blanton et al., 2017), that is in the process of acquiring integral-field spectroscopic data for $\sim$ 10000 galaxies in the local universe ($0.01 < z < 0.15$) spanning all environments, morphologies and a stellar mass range $10^9 - 10^{11} M_\odot$ (Bundy et al., 2015). It utilises the Baryonic Oscillation Spectroscopic Survey spectrograph (BOSS) which provides a spectral resolution of $R \approx 2000$ ($\sigma_{inst} \approx 77$km s^{-1}) in the wavelength range $3600 - 10300$ Å (Smee et al., 2013). Target galaxies are chosen so the final sample has a flat distribution in i-band absolute magnitude, and uniform spatial coverage in units of effective radius R$_e$. To accomplish the science goals, about 2/3 of the sample is covered out to 1.5 R$_e$ (Primary sample), and 1/3 to 2.5R$_e$ (Secondary sample) (Yan et al., 2016).

The observations are performed using predrilled plates where a set of 17 hexagonal fiber-bundles IFU’s are pluged in. The diameter of each fiber is 2 arcsec. The number

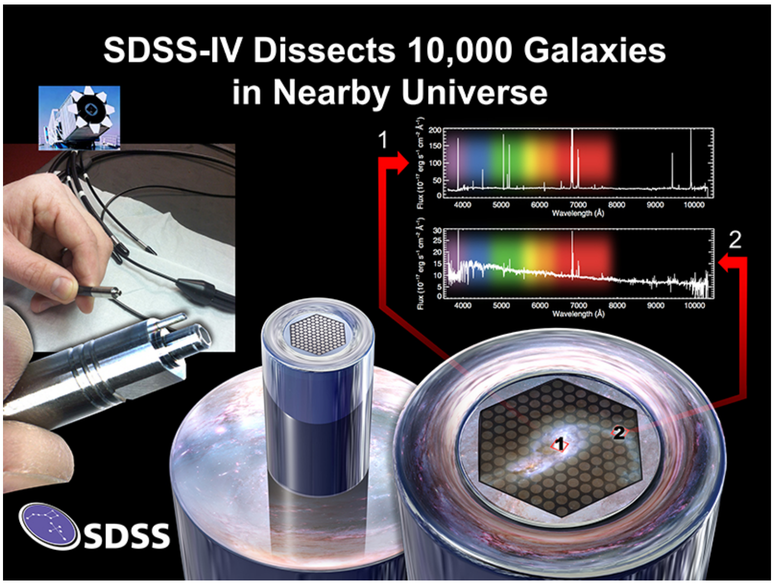

Figure 3: An image of a 127 fiber IFU, ready to be plugged into a SDSS plate. The right side illustrates how different regions in the galaxy have dramatically different spectra. Image Credit: Dana Berry / SkyWorks Digital Inc., David Law, and the SDSS collaboration.

of fibers in each bundle ranges from 19 to 127 (Drory et al., 2015). A 3-point dithering pattern is adopted to have total coverage of the field of view (Law et al., 2016). Figure 3 shows an image of a 127 fiber MaNGA IFU.

We will refer to the galaxies used in this work using the MaNGA identification number **manga-XXXX-YYYZZ**, where the first number (XXXX) is the PlateID, the second number (YYY) is the number of fibers of the IFU used, and the last number (ZZ) is used to distinguish between the IFU's with the same number of fibers.

1.6. The CALIFA survey

The CALIFA survey (Sánchez et al., 2012) has provided integral-field observations for 667 galaxies in the local universe ($0.005 < z < 0.03$), spanning a wide range of stellar masses, ionization conditions and morphological types (Sánchez et al., 2016a). The CALIFA data was obtained using the integral-field spectrograph PMAS (Roth et al., 2005) in the PPak configuration, which consists of 382 fibers of 2.7 arcsec diameter. Two different spectral setups were used for the observations. A low-resolution setup ($R = 850$ at 5000 Å) called V500 covering the range $3750 - 7300$ Å, and a medium-resolution setup ($R = 1650$ at 4500 Å) called V1200 from $3400 - 4750$ Å.

This thesis is organized as follow: In Chapter 2 we present our galaxy sample. In Chapter 3 we explain our methodology and the data analysis tools we used. In Chapter

4 we present our results, including the measurements of Ω_{bar}, R_{CR} and $\mathcal{R}$. In Chapter 5 we discuss our results. Finally in Chapter 6 we give our conclusions. Throughout this paper we estimated our distances using the cosmology $\mathrm{H_0} = 67.77\mathrm{km\,s^{-1}\,Mpc^{-1}}$, $\Omega_\mathrm{m} = 0.307$, $\Omega_\Lambda = 0.693$ (Planck Collaboration et al., 2016).

Capítulo 2

Sample selection

From an initial sample of $\approx$ 500 galaxies of all morphology types, we choose an initial sample of 59 MaNGA galaxies, that showed prominent bars. From this sample we discarded galaxies with inclinations $i < 20°$, since they are not well suited for a kinematic study, and high inclined galaxies $i > 70°$, since the projection uncertainties increase drastically. We also discarded galaxies with poor velocity maps or had field stars present in the MaNGA field.

We applied the TW-method to the remaining galaxies, and exclude those where the results did not made physical sense. For example, galaxies where the value of Ω_{bar} was higher that the disc angular velocity curve at all radius, or cases where the uncertainties were so large that we could not conclude anything significant. Most of these cases where galaxies were the bar PA was close to any of the disc axes. This is expected, since the TW-integrals tend to cancel out. We will discuss more about these cases in Chapter 5. The final MaNGA sample consists of 15 barred galaxies. In figure 4 we show the SDSS post-stamp of our MaNGA sample, with the observed hexagon.

In order to compare our results and find systematic errors in our methodology, we re-analysed a sub-sample of 3 galaxies studied by Aguerri et al. (2015). The main properties of our sample are shown in Table 1. These include the systemic velocity V_{sys}, measured from the stellar velocity maps, r_{50} obtained from the NASA-Sloan Atlas, stellar mass obtained from Pipe3D analysis (see Section 3.1.1), right ascension, declination and morphological type as classified by our group.

7495-12704

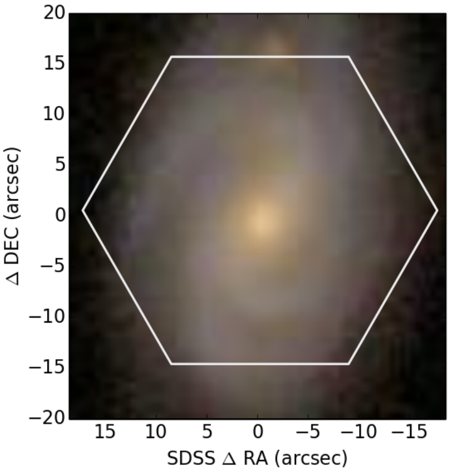

7962-12703

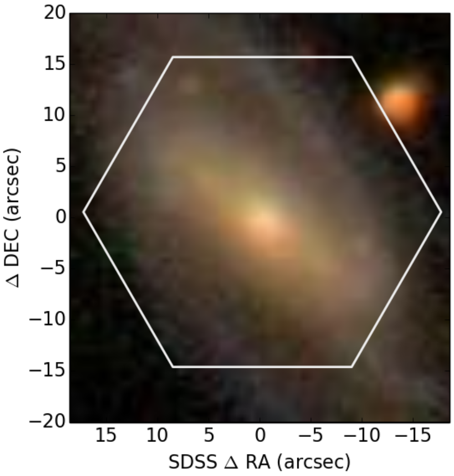

7990-12704

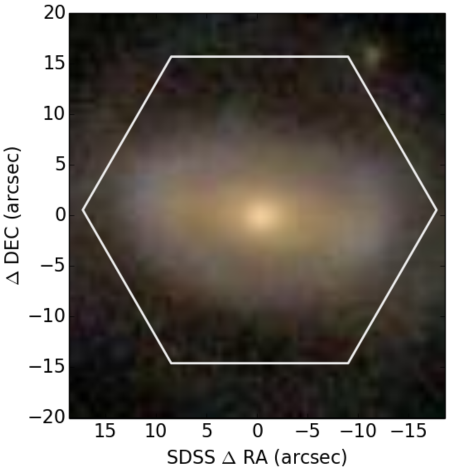

8135-6103

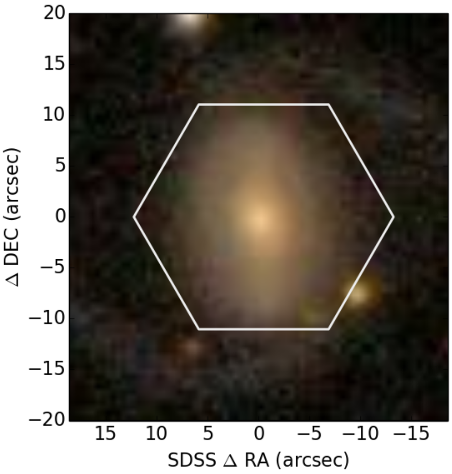

8243-12704

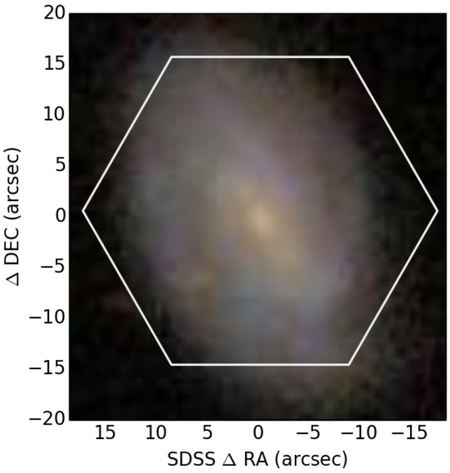

8256-6101

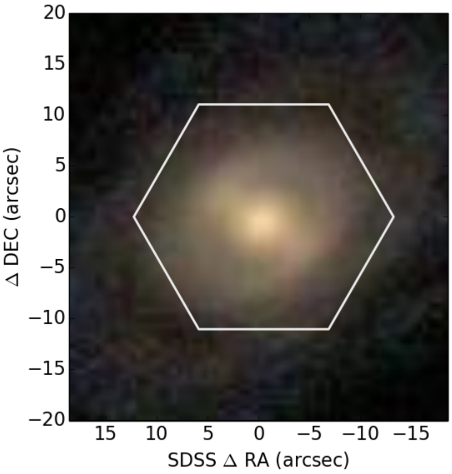

8257-3703

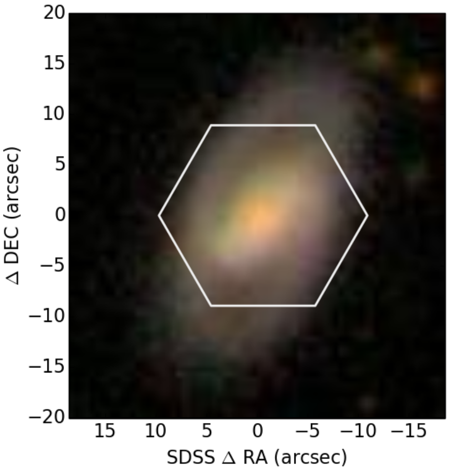

8312-12704

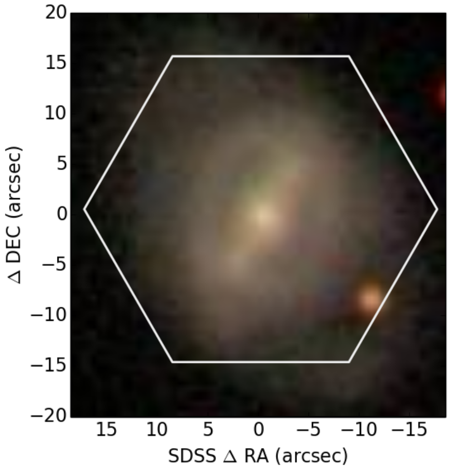

8313-9101

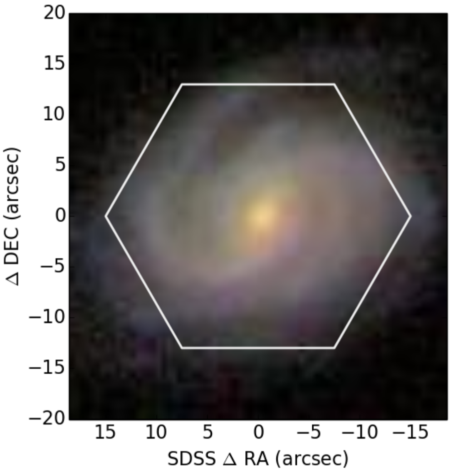

8317-12704

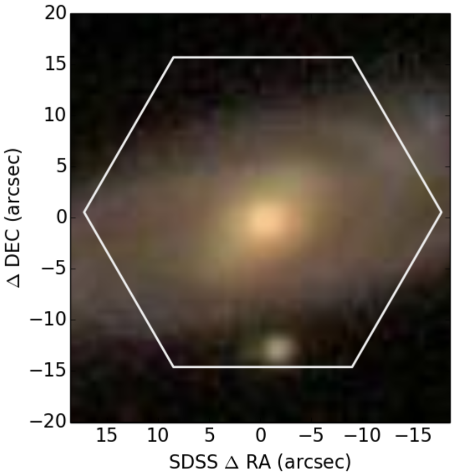

8318-12703

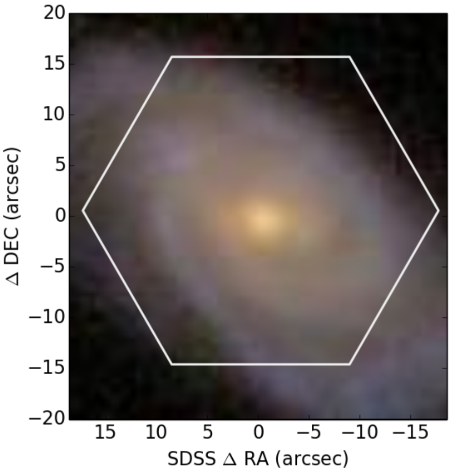

8341-12704

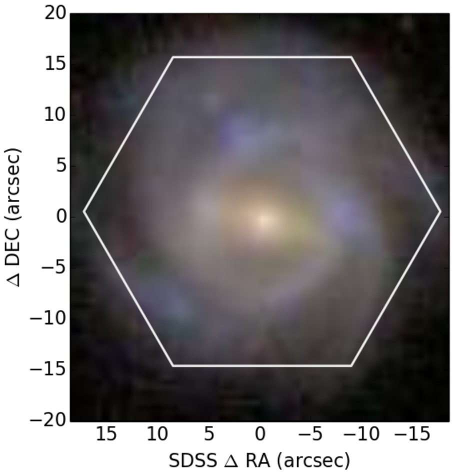

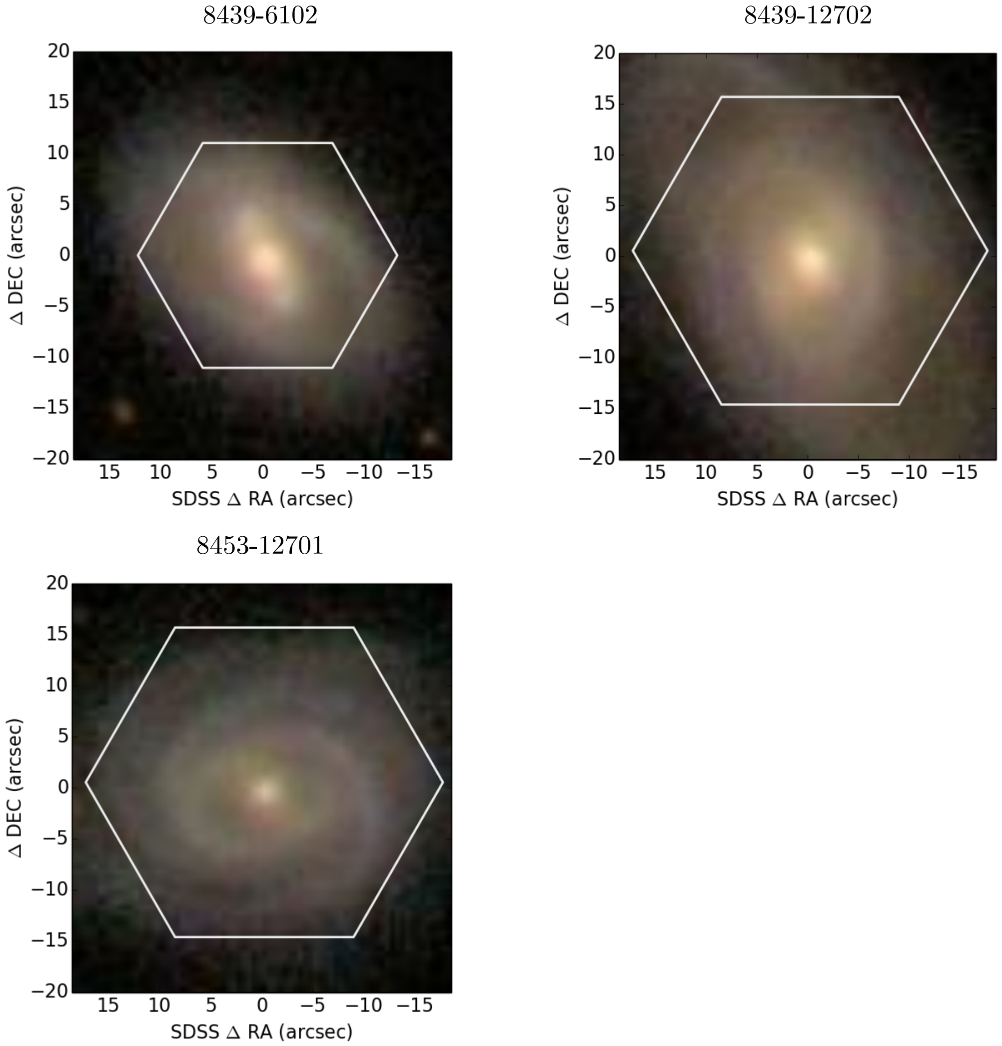

8439-6102

8439-12702

8453-12701

Figure 4: SDSS post stamps of the MaNGA sample. The white hexagon shows the area observed by MaNGA IFU.

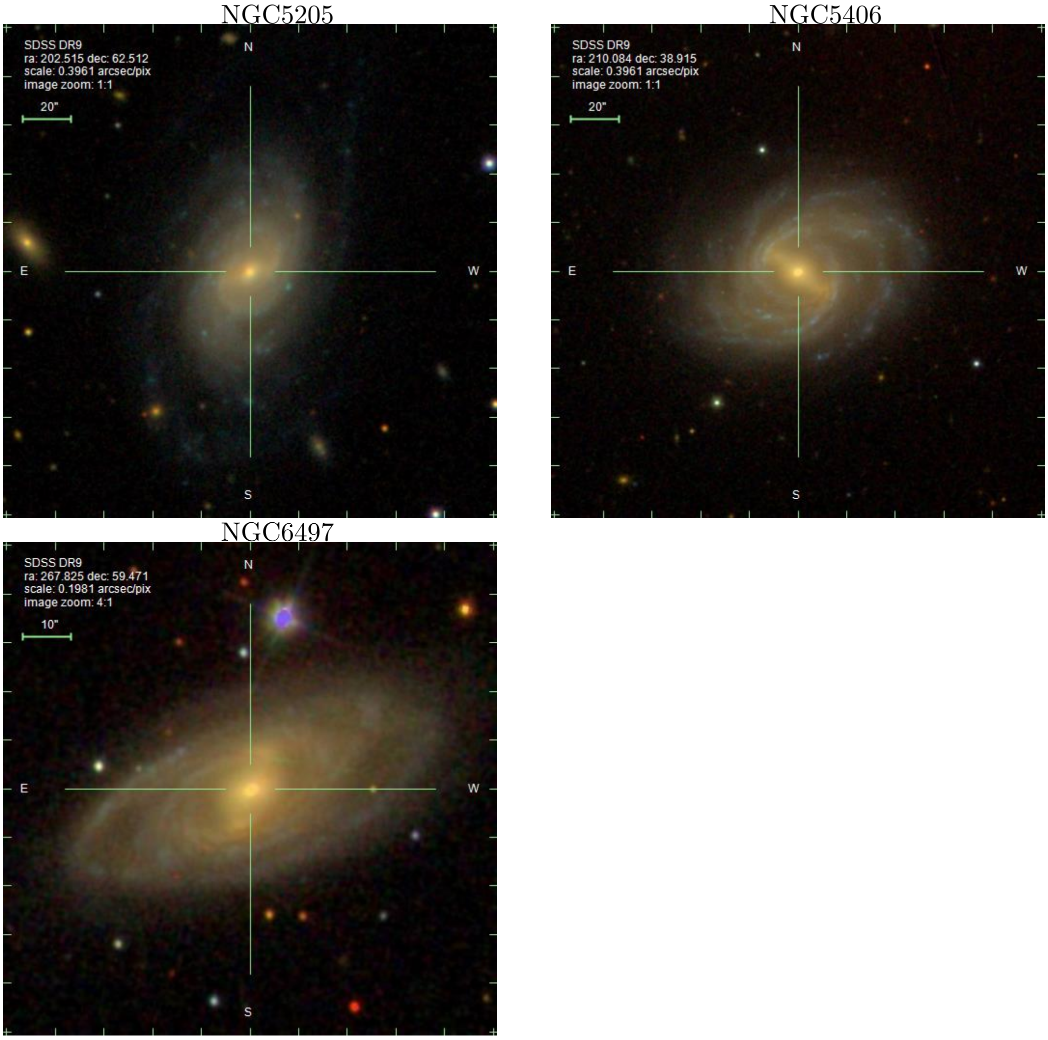

Figure 5: SDSS post stamps of the CALIFA subsample

Table 1: Main parameters of our sample

Galaxy (1)	V_{sys} [km s^{-1}] (2)	r_{50} [kpc] (3)	$log(M/M_{\odot})$ (4)	RA (hh:mm:ss) (5)	Dec (hh:mm:ss) (6)	Morph (7)
7495-12704	8763.9	7.6	10.8	13:41:45	27:00:16	SBbc
7962-12703	14421.9	14.5	11.2	17:24:52	28:04:42	SBbc
7990-12704	8120.4	9.3	10.6	17:29:57	58:23:51	SBa
8135-6103	14719.5	9.6	11.0	07:32:14	39:33:36	SBab
8243-12704	7265.3	5.6	10.9	08:44:40	53:57:04	SBbc
8256-6101	7490.1	4.2	10.4	10:54:56	41:29:54	SBb
8257-3703	7554.0	2.9	10.6	11:06:37	46:02:20	SBb
8312-12704	8974.0	6.3	10.5	16:29:13	41:09:03	SBa
8317-12704	16324.1	7.0	11.2	12:54:49	44:09:20	SBab
8313-9101	11689.1	20.6	10.9	15:58:47	41:56:17	SBbc
8318-12703	11864.3	11.1	11.1	13:04:56	47:30:13	SBbc
8341-12704	9237.4	6.1	10.7	12:36:51	45:39:04	SBbc
8439-6102	10239.4	5.5	10.9	09:31:07	49:04:47	SBb
8439-12702	8151.2	10.2	10.7	09:26:09	49:18:37	SBab
8453-12701	7607.5	6.5	10.4	10:05:14	46:39:03	SABc
NGC5205	1742.7	3.7	10.0	13:30:04	62:30:42	SBbc
NGC5406	5363.9	14.1	11.3	14:00:20	38:54:56	SBb
NGC6497	6028.0	9.2	11.3	17:51:18	59:28:15	SBab

Col. (1): Galaxy ID. Col. (2): Systemic velocity. Col. (3): Effective radius. Col. (4): Mass. Col. (5): Right ascension. Col. (6): Declination, Col. (7): Morphological type

Capítulo 3

Methodology

In this Chapter we discuss our methodology for estimating Ω_{bar}, and R_{CR} including a brief description of the software packages we used. In this chapter we also explain how we choose the number, separation and length of the psudo-slits to perform the TW integrals.

In order to use the TW method, we need a reliable way to obtain the stellar surface brightness and the stellar line-of-sight (LOS) velocity maps from the MaNGA and CALIFA datacubes. To recover these, we used the data analysis pipeline *Pipe3D*, a tool developed to analyse and characterize the stellar populations and the ionized gas of IFS datacubes (Sánchez et al., 2015, 2016b).

We modeled the rotation curves of our galaxies using the tool *velfit* which is able to model non-axisymmetric motions produced by bar-like perturbations (Spekkens & Sellwood, 2007; Sellwood & Sánchez, 2010). Once we have the rotation curve we can infer the the angular velocity curve dividing by the radius. Comparing this curve with Ω_{bar} we can measure the R_{CR}. Using the uncertainties of Ω_{bar} and we can repeat this experiment in a Monte Carlo simulation and obtain the distribution of possible R_{CR}. Combining this with the uncertainties of R_{bar} we can estimate the probabilities of the bar being slow, fast or ultra fast.

Various geometric parameters are needed throughout the procedure: (1) The disc PA and inclination are required for the TW method, (2) an estimation of the bar length is needed to compute the parameter $\mathcal{R}$ (3) to model the rotation curve we need a first guess of the bar PA and the disc inclination. To obtain these parameters we performed an isophote analysis using the IRAF task *Ellipse* over the r-band SDSS images (Jedrzejewski, 1987). The whole process is illustrated as a flow diagram in figure 6

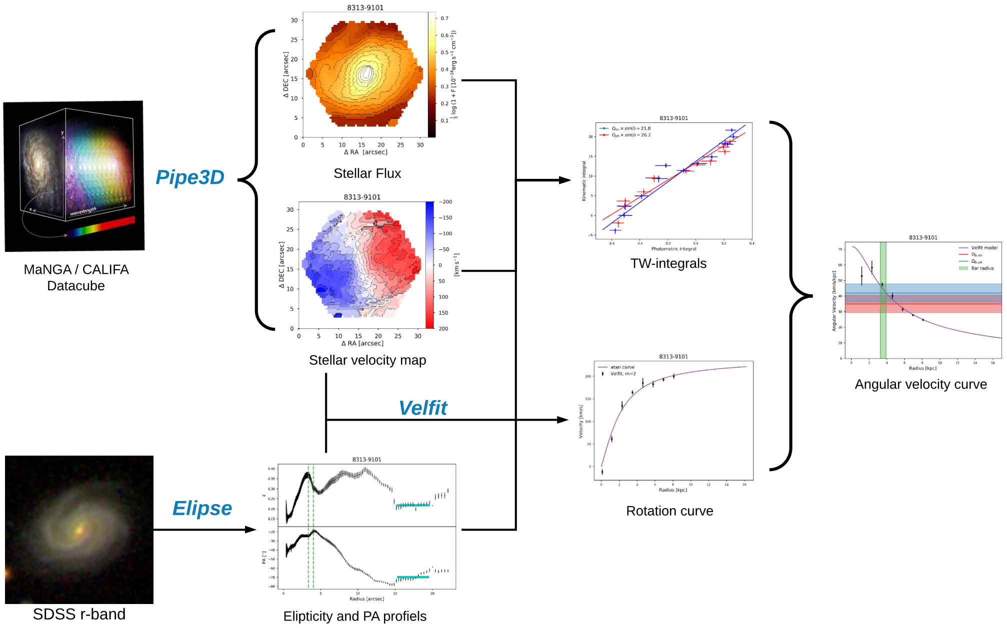

Figure 6: Our methodology. The MaNGA and CALIFA datacubes are analysed with the spectral fitting tool *Pipe3D*, to recover the stellar flux and velocity maps. An isophote analysis is performed using the *Ellipse* package over the SDSS r-band image to recover the geometric parameters of the galaxy. Using the velocity map, and the geometric parameters, we model the velocity curve using an m=2 model with *velfit*. We measure the kinematic orientation using the velocity map. We perform the TW method using the photometric and kinematic orientation, obtaining Ω_{bar}. The bar pattern speed is then compared with the angular velocity curve to get an estimation of R$_{CR}$ and classify the bar as a slow, fast or ultra-fast rotator.

3.1. Data analysis

3.1.1. Pipe3D

The observed spectra of a galaxy is the complex sum of various components that interact between each other, and contribute by emitting or absorbing light. Uncoupling the different contributions is not an easy process. Various non-linear process, degeneracies, and physical processes need to be taken into account.

One of the most important components of the galaxy spectra are the stellar populations. Their combined contribution is responsible of shaping the continuum. The spectra of a single star depends on various parameters such as the age, the mass and the metallicity. Its spectrum can also be blue or red-shifted depending on the galaxy kinematics. Another important component is the ionized gas, which emits at specific wavelengths described by the quantum mechanics. They are produced by different astrophysical processes such as the star formation, stellar winds from evolved stars or the galactic nuclear activity. These lines can also be shifted and broaden by the gas kinematics. Finally, the dust contributes by absorbing radiation in the optical and the ultraviolet, while emitting in the infrared.

Ideally to achieve the most complete description of the galaxy, the spectra of each spaxel should be analysed independently one by one. However, the signal-to-noise ratio (S/N) decreases dramatically as we move away from the center, causing poor quality spectra in the outskirts. To solve this problem, the information of consecutive spaxels can be added together until a S/N goal is reached. To choose which spaxels should be added together a binning algorithm is required to divide the galaxy efficiently (see e.g. Samet, 1984; Cappellari & Copin, 2003).

Pipe3D uses a binning algorithm that tries to reach a goal in S/N while adding together areas of the galaxy with similar physical properties (like spiral arms) by following the surface brightness. This is specially important for our purposes, since the TW method should only weight the non-axisymmetric of the bar. Once the segmentation is performed, the spectra within each spatial bin are co-added into a single spectrum. The stellar properties in each bin are derived by fitting the co-added spectra to a set of single stellar population (SSP) templates, using the fitting tool FIT3D (Sánchez et al., 2015). For a detailed description of the complete procedure, including the dust attenuation, uncertainties and S/N distribution see Sánchez et al. (2015, 2016b); Ibarra-Medel et al. (2016).

The resulting dataproducts are a set of maps for various physical or observational properties. For example, emission lines fluxes, stellar mass, stellar and gaseous velocity maps, star formation histories, etc. [1] In particular, for this work we are interested in the stellar flux and the stellar velocity maps, which are shown in figures 7 and 8 respectively. In both figures we show the pseudo-slits used for the TW method with solid black lines. A green solid line is used to highlight the orientation and length of the bar. In the LOS velocity maps we also show with gray dots the spaxels used to find the kinematic PA (PA_{kn}), which is shown with a dashed black line (see Section 3.1.4). The details on how we obtained all these geometric parameters will be described in the next section.

---

[1] A full description of the dataproducts can be found at: `https://data.sdss.org/datamodel/files/MANGA_PIPE3D/MANGADRP_VER/PIPE3D_VER/PLATE/manga.Pipe3D.cube.html`

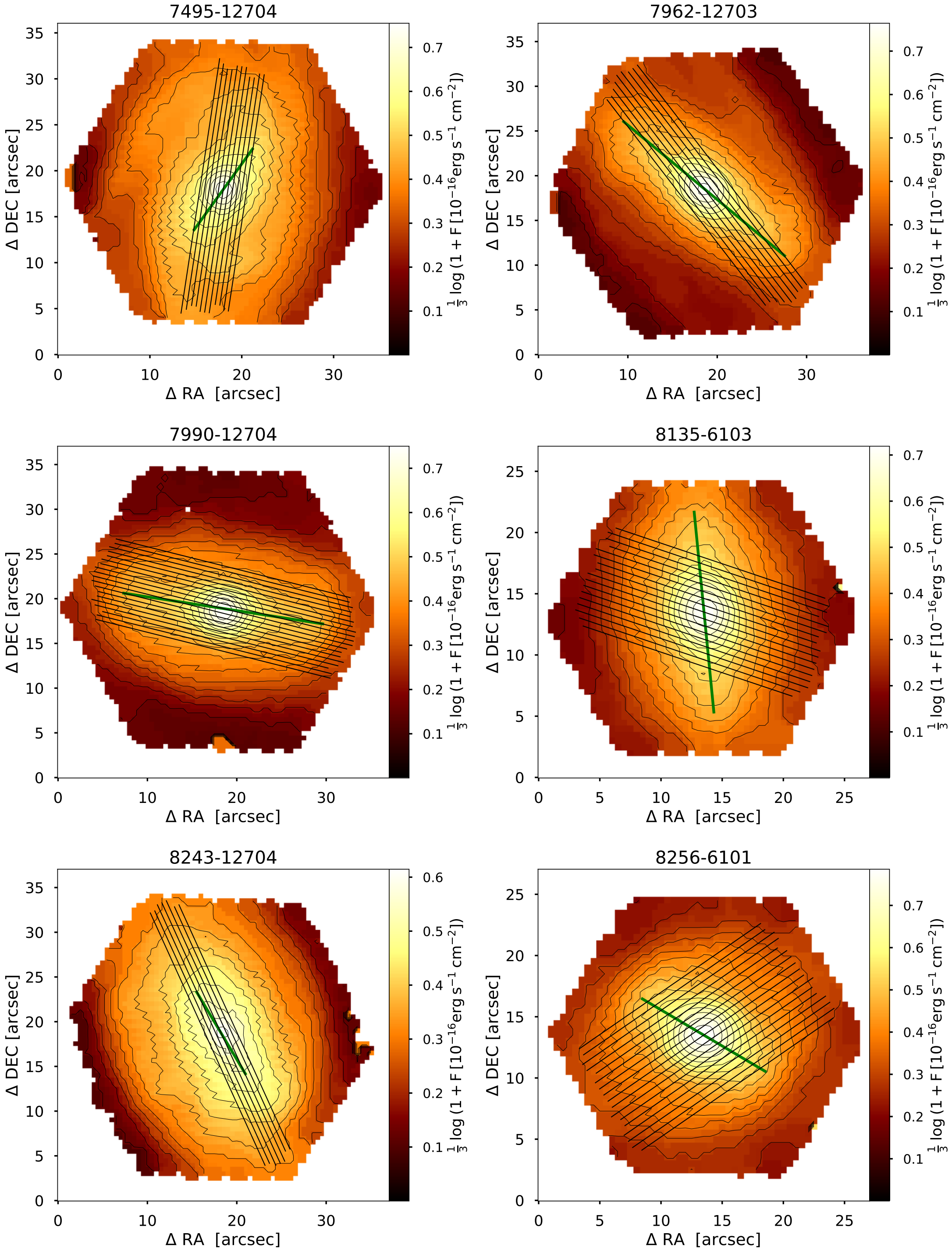
7495-12704
7962-12703
7990-12704
8135-6103
8243-12704
8256-6101
Δ DEC [arcsec]
Δ RA [arcsec]
$\frac{1}{3}\log(1+F\,[10^{-16}\mathrm{erg\,s^{-1}\,cm^{-2}}])$
0.1
0.2
0.3
0.4
0.5
0.6
0.7
0
5
10
15
20
25
30
35

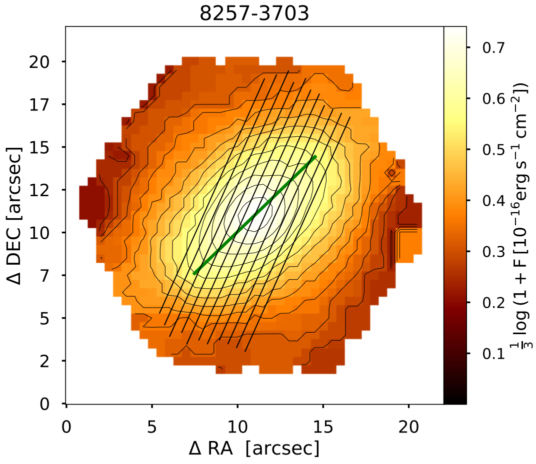
8257-3703
Δ DEC [arcsec]
Δ RA [arcsec]
0
2
5
7
10
12
15
17
20
0
5
10
15
20
0.1
0.2
0.3
0.4
0.5
0.6
0.7
$\frac{1}{3}\log(1+F\,[10^{-16}\mathrm{erg\,s^{-1}\,cm^{-2}}])$

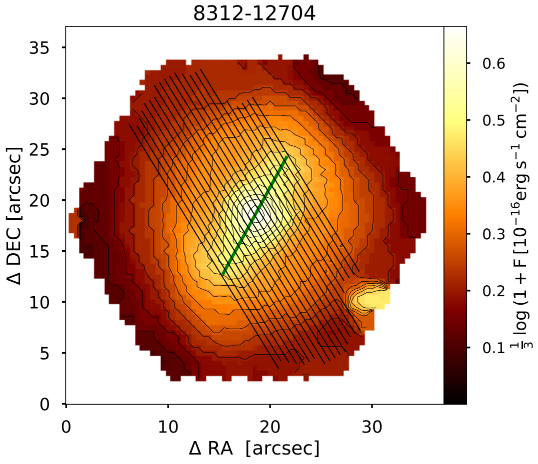
8312-12704
Δ DEC [arcsec]
Δ RA [arcsec]
0
5
10
15
20
25
30
35
0
10
20
30
0.1
0.2
0.3
0.4
0.5
0.6
$\frac{1}{3}\log(1+F\,[10^{-16}\mathrm{erg\,s^{-1}\,cm^{-2}}])$

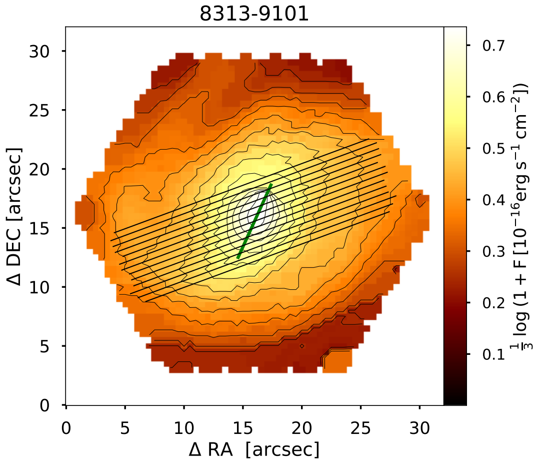
8313-9101
Δ DEC [arcsec]
Δ RA [arcsec]
0
5
10
15
20
25
30
0
5
10
15
20
25
30
0.1
0.2
0.3
0.4
0.5
0.6
0.7
$\frac{1}{3}\log(1+F\,[10^{-16}\mathrm{erg\,s^{-1}\,cm^{-2}}])$

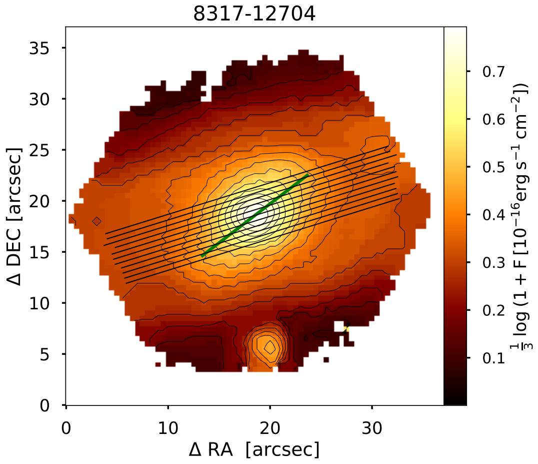
8317-12704
Δ DEC [arcsec]
Δ RA [arcsec]
0
5
10
15
20
25
30
35
0
10
20
30
0.1
0.2
0.3
0.4
0.5
0.6
0.7
$\frac{1}{3}\log(1+F\,[10^{-16}\mathrm{erg\,s^{-1}\,cm^{-2}}])$

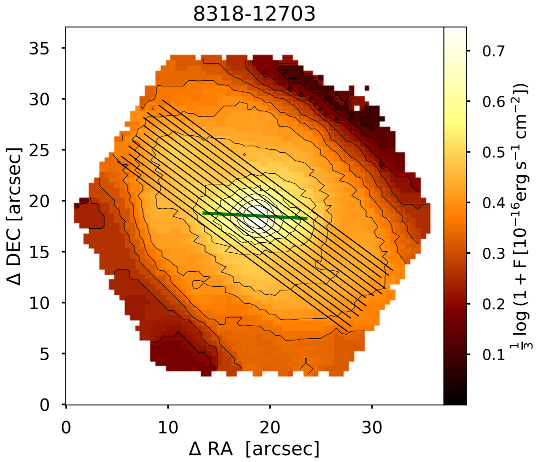
8318-12703
Δ DEC [arcsec]
Δ RA [arcsec]
0
5
10
15
20
25
30
35
0
10
20
30
0.1
0.2
0.3
0.4
0.5
0.6
0.7
$\frac{1}{3}\log(1+F\,[10^{-16}\mathrm{erg\,s^{-1}\,cm^{-2}}])$

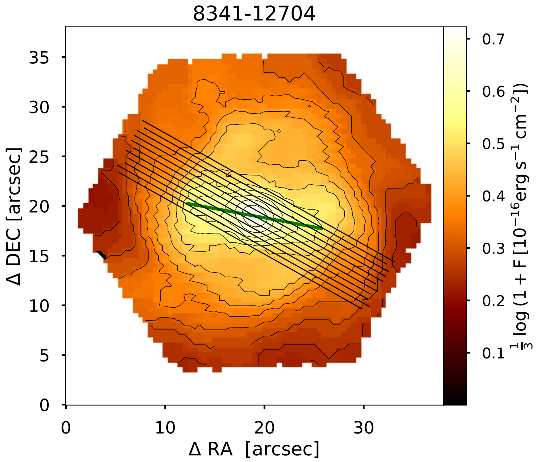
8341-12704
Δ DEC [arcsec]
Δ RA [arcsec]
0
5
10
15
20
25
30
35
0
10
20
30
0.1
0.2
0.3
0.4
0.5
0.6
0.7
$\frac{1}{3}\log(1+F\,[10^{-16}\mathrm{erg\,s^{-1}\,cm^{-2}}])$

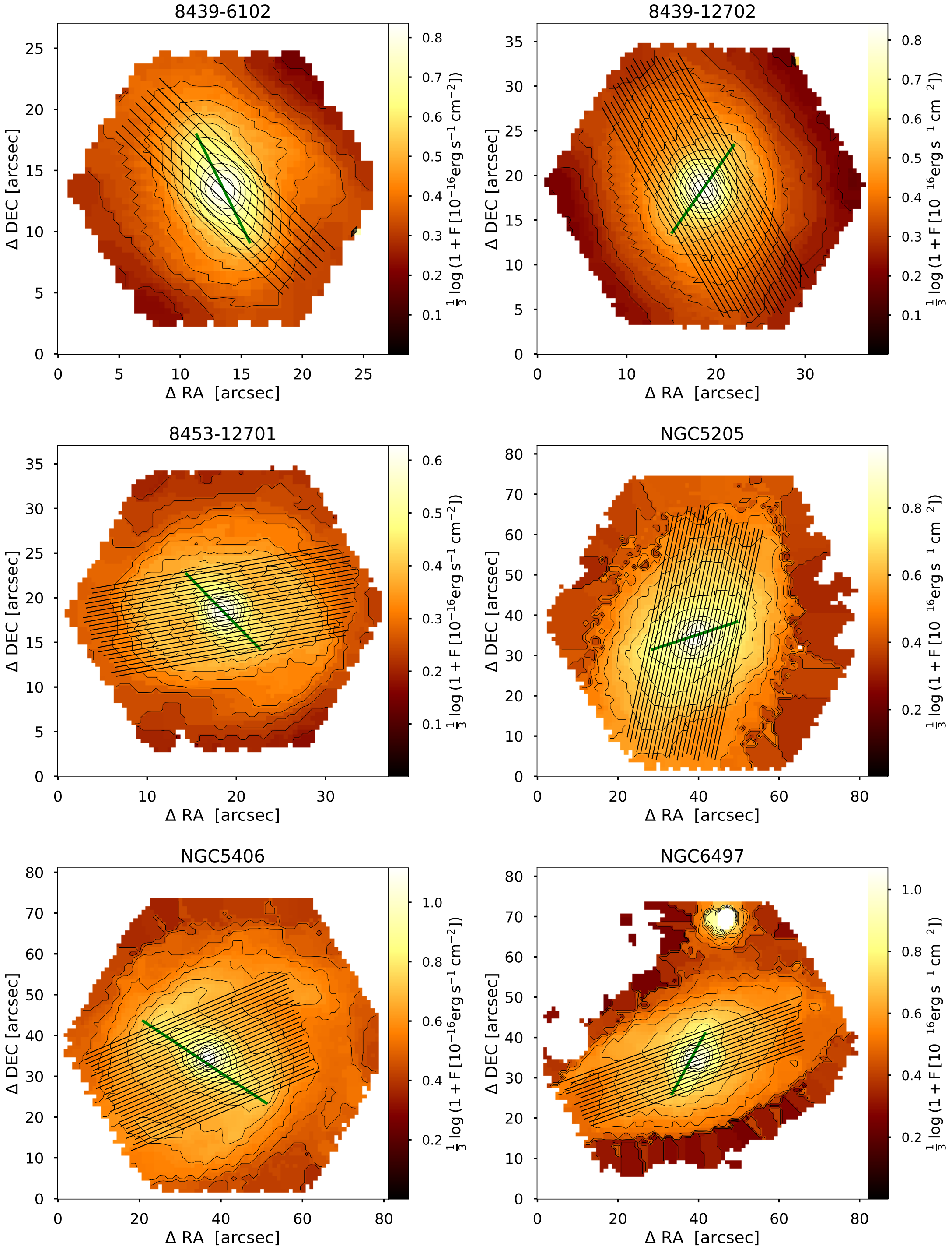

Figure 7: Stellar flux maps of our sample. The black solid lines show the pseudo slits used for the TW method, oriented towards the PA$_{ph}$. The green line is oriented towards the bar PA, and extends up to R$_{bar,1}$.

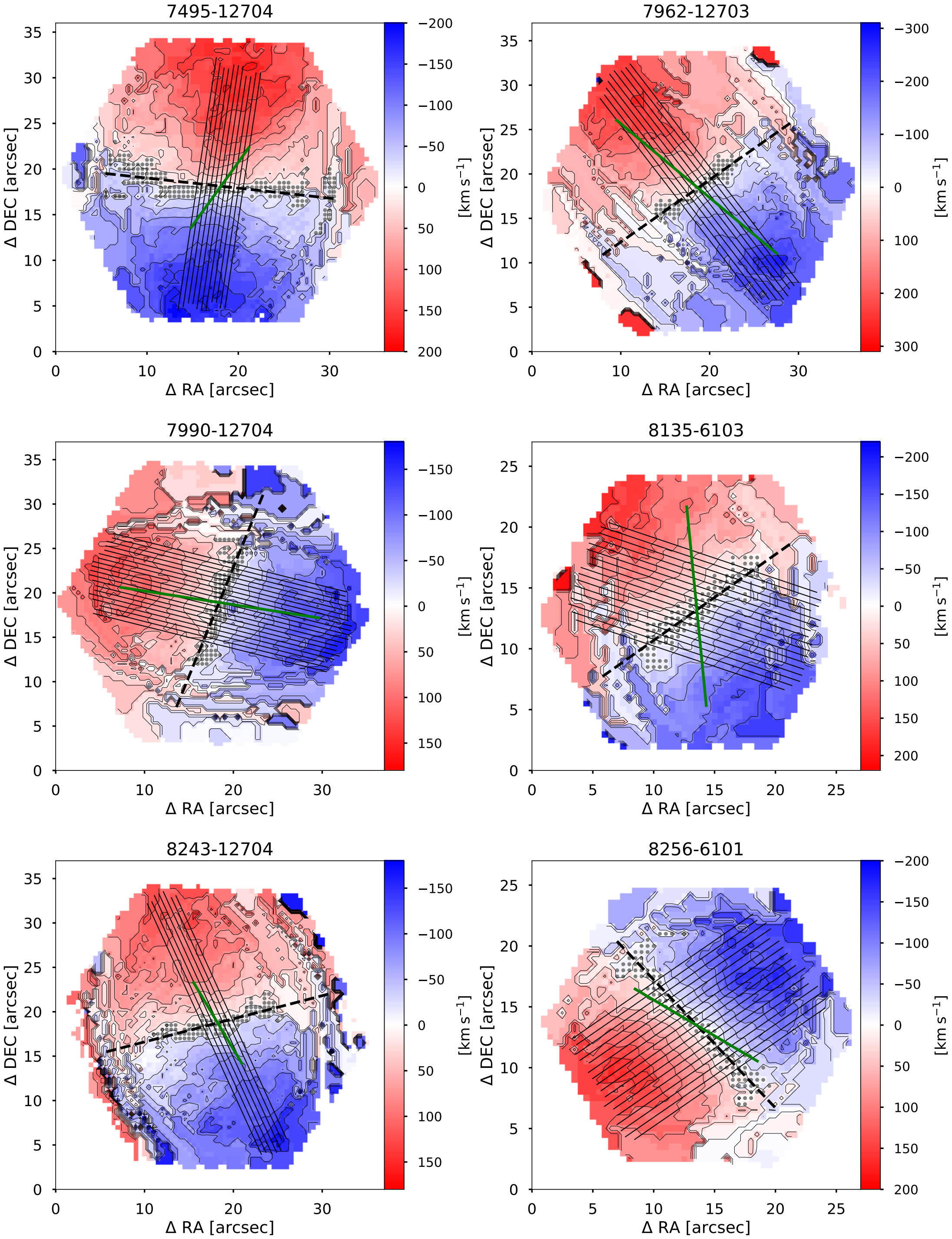
7495-12704
7962-12703
7990-12704
8135-6103
8243-12704
8256-6101
Δ DEC [arcsec]
Δ RA [arcsec]
[km s^{-1}]
0
5
10
15
20
25
30
35
−300
−200
−150
−100
−50
0
50
100
150
200
300

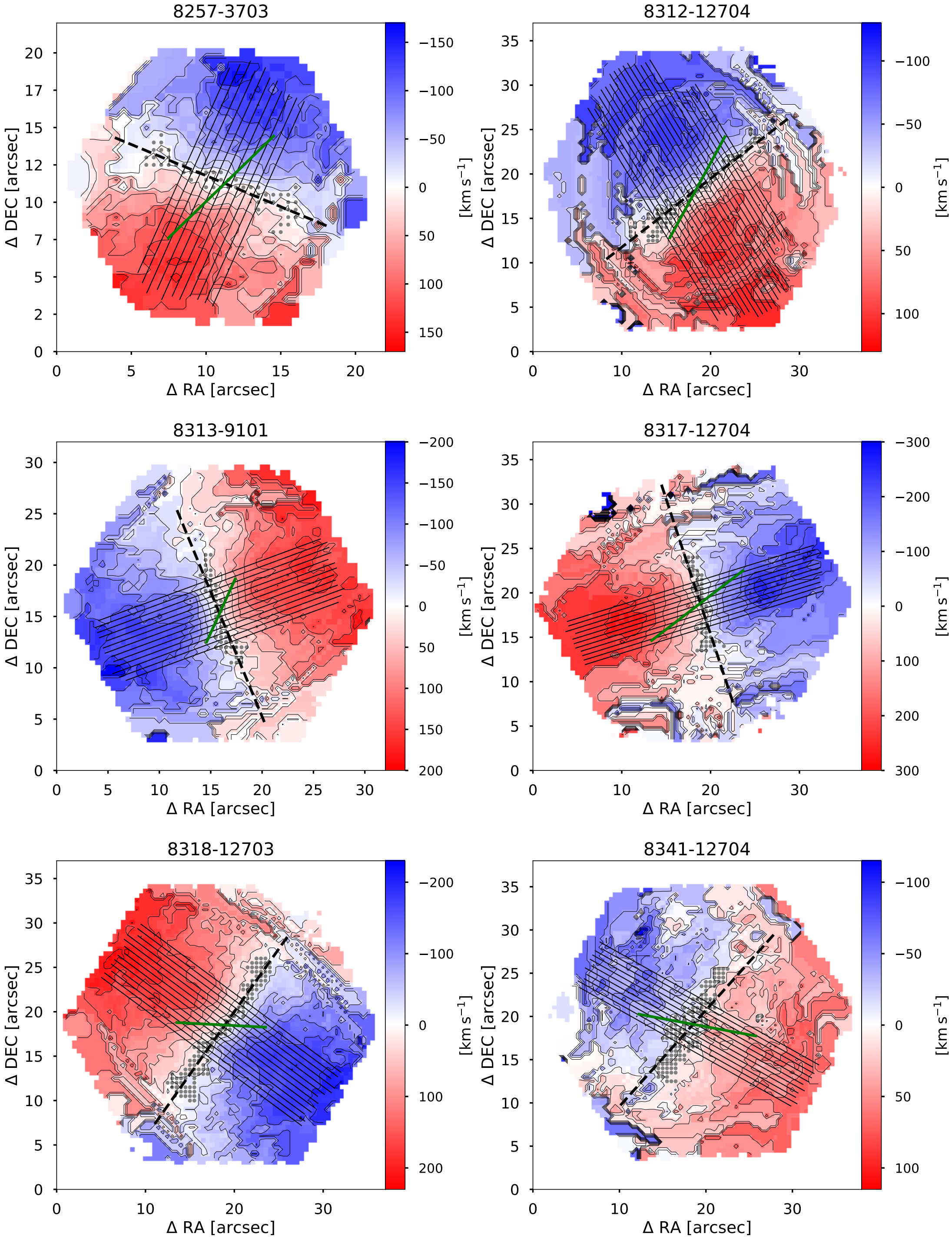
8257-3703
8312-12704
8313-9101
8317-12704
8318-12703
8341-12704
Δ DEC [arcsec]
Δ RA [arcsec]
[km s^{-1}]
−150
−100
−50
0
50
100
150
200
−200
−300
300

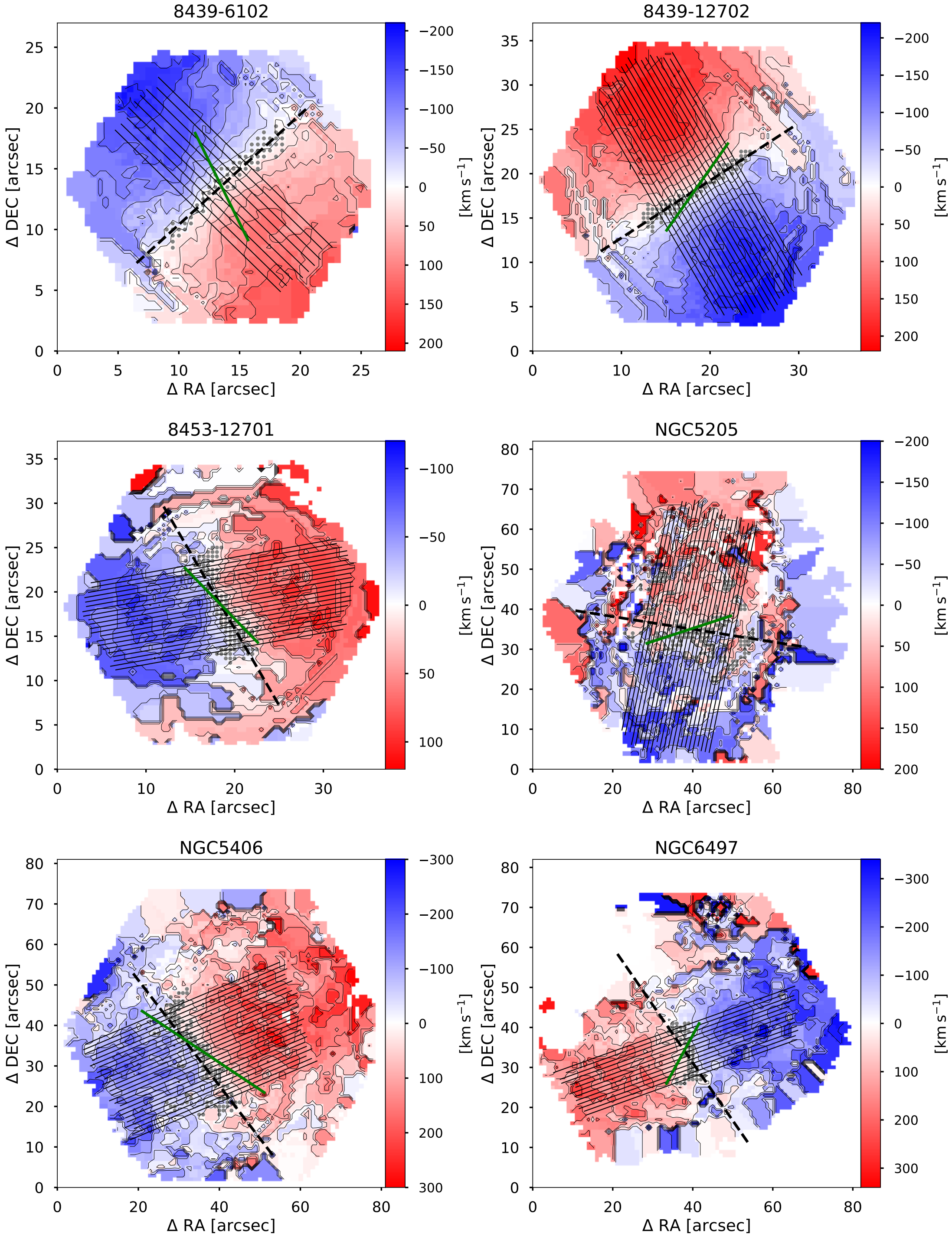

Figure 8: LOS velocity maps of our sample. Same as in Figure 7. The grey dots are the spaxels used to fit the zero-velocity line, which is shown with the segmented black line.

3.1.2. Geometric parameters

One of the most powerful and simple methods for studying the light distribution of extended objects is an isophote analysis. In the particular the symmetry in the light distribution of galaxies allows to approximate the isophotes as ellipses. These ellipses can be completely described with their ellipticity ($\epsilon = 1 - b/a$) and PA given by the orientation of the major axis. The resulting ellipticity and PA radial profiles provide significant information about the structure of the galaxy.

In particular, bars are characterized by a monotonically increasing elliptical radial profile, growing from almost zero at the center to a local maximum. The position of this local maximum gives a lower limit to the bar radius (Wozniak et al., 1995; Michel-Dansac & Wozniak, 2006). We will refer to this radius as $R_{bar,1}$. A signature of the bar can also be found in the PA profile, since the orientation of the major axis is roughly constant in the bar region. The bar length can be estimated as the radius at which the PA changes 5° with respect the value at the $R_{bar,1}$. (e.g. Wozniak et al., 1995; Marinova & Jogee, 2007; Aguerri et al., 2009, 2015). We will refer to this radius as $R_{bar,2}$.

At larger radii, the ellipse and PA profiles approach constant values corresponding to the disc ellipticity and PA (ϵ_d and PA_{ph}). Assuming a flat disc, ϵ_d is related to the inclination of the galaxy i by $\cos i = 1 - \epsilon_d$. We measure these parameters in regions where the S/N was close to 3. In figure 9 we show the ellipticity and PA profiles of our sample, obtained from performing an isophote analysis over the SDSS r-band image. The green dashed lines show the measurements of $R_{bar,1}$ and $R_{bar,2}$, the cyan line shows the measured ϵ_d and PA_{ph}.

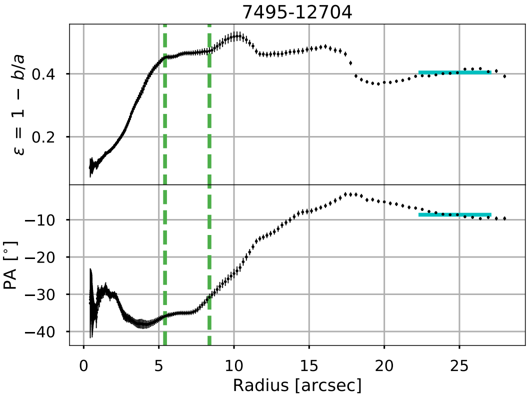
7495-12704

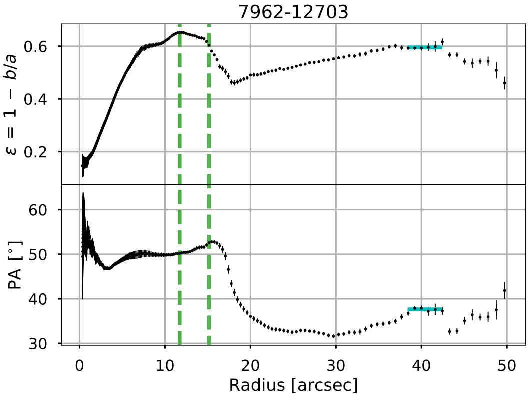
7962-12703

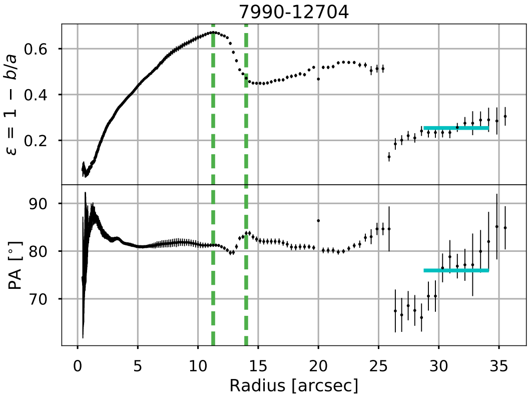
7990-12704

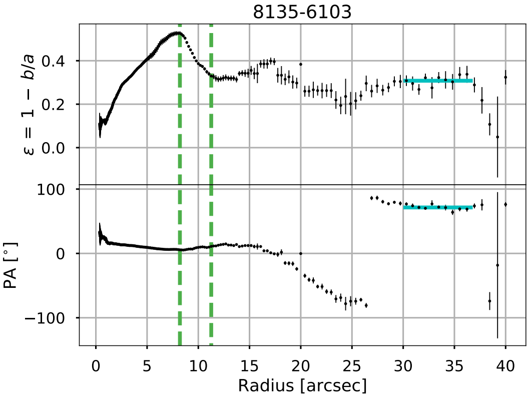
8135-6103

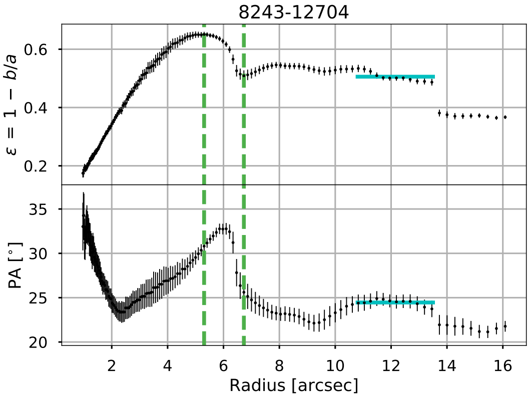
8243-12704

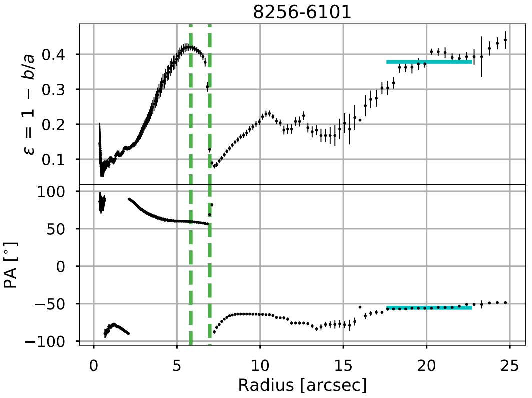
8256-6101

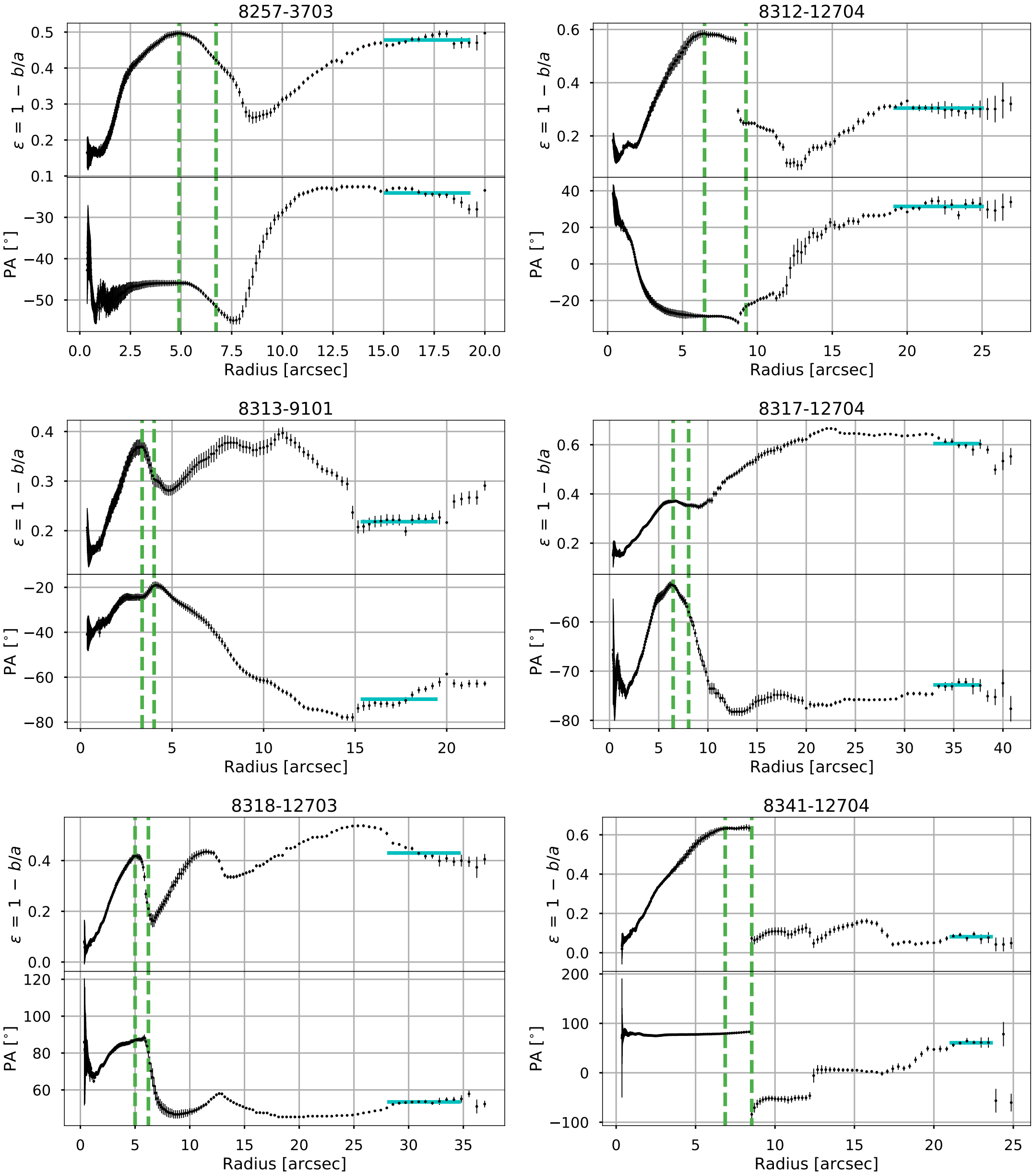
8257-3703
8312-12704
8313-9101
8317-12704
8318-12703
8341-12704
$\epsilon = 1 - b/a$
PA [°]
Radius [arcsec]

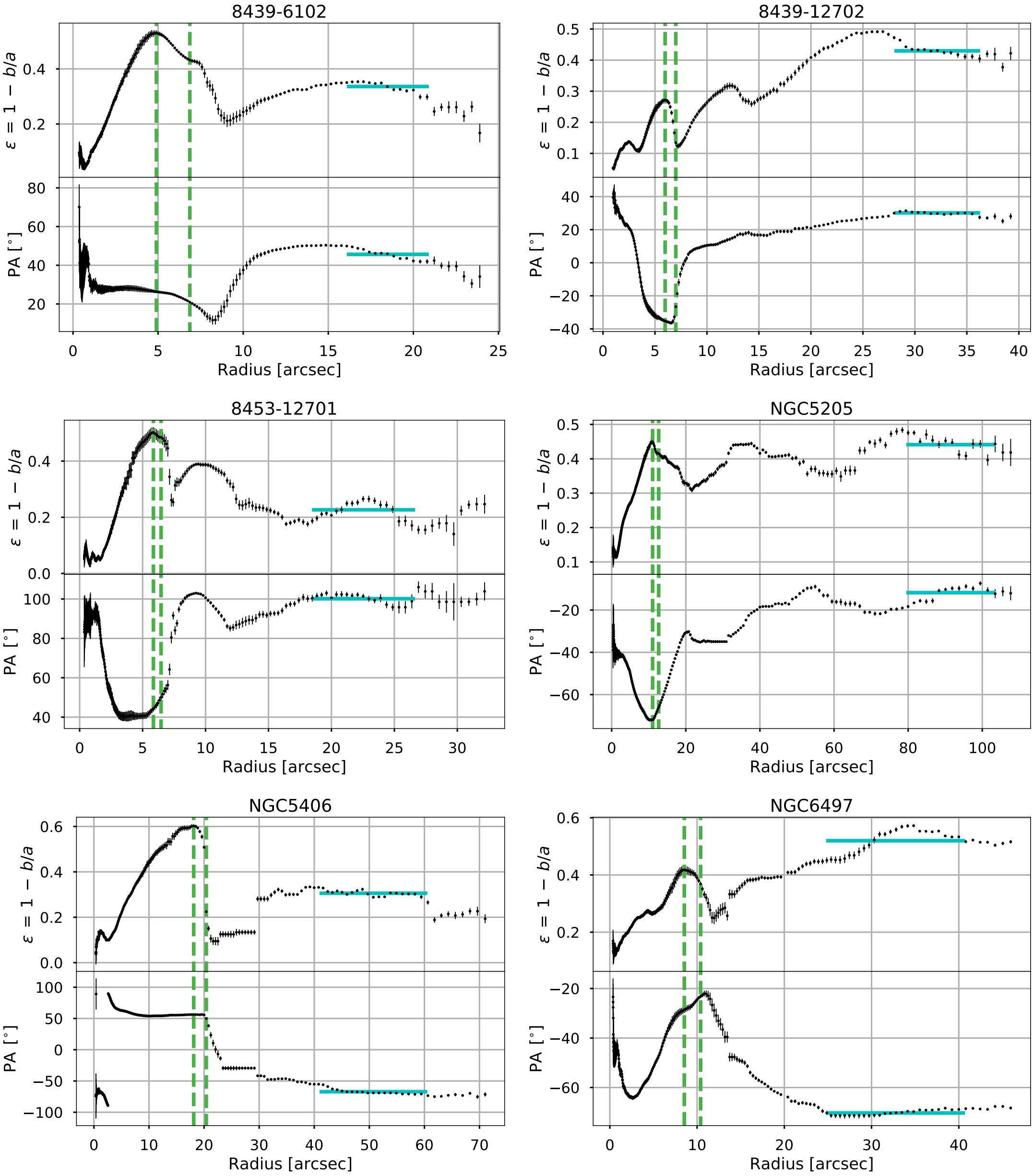

Figure 9: Ellipticity and PA profiles of our sample. The green dashed lines show the values of $R_{bar,1}$ (at maximum ellipticity) and $R_{bar,2}$ (at $\Delta PA > 5°$ with respect $R_{bar,1}$). The cyan solid lines show measured disc ellipticity and PA, over the radius used for estimating them.

3.1.3. Analytic deprojection of the bar

In order to get the bar measurements to their face-on values, we deprojected the bar using the analytic method described in Gadotti et al. (2007). The method assumes the bar can be described as a simple ellipse and has uncertainties $\sim 10\,\%$ at moderate inclination angles ($i \leq 60°$) (Zou et al., 2014). If a and b are the projected major and minor axes of the bar respectively and α is the angle between the bar PA and the disc PA, then the deprojected major axis is the maximum between $S1$ and $S2$:

$$S1 = \frac{2\left(AF^2 + CD^2 + GB^2 - 2BDF - ACG\right)}{(B^2 - AC)\left[(C-A)\sqrt{1 + \frac{4B^2}{(A-C)^2}} - (C+A)\right]} \tag{3.1}$$

$$S2 = \frac{2\left(AF^2 + CD^2 + GB^2 - 2BDF - ACG\right)}{(B^2 - AC)\left[(A-C)\sqrt{1 + \frac{4B^2}{(A-C)^2}} - (C+A)\right]} \tag{3.2}$$

where

$$A = \frac{\cos^2\alpha}{a^2} + \frac{\sin^2\alpha}{b^2} \tag{3.3}$$

$$B = \frac{\cos\alpha\sin\alpha\cos i}{a^2} - \frac{\cos\alpha\sin\alpha\cos i}{b^2} \tag{3.4}$$

$$C = \frac{\sin^2\alpha\cos^2 i}{a^2} + \frac{\cos^2\alpha\cos^2 i}{b^2} \tag{3.5}$$

$$D = F = 0 \tag{3.6}$$

$$G = -1 \tag{3.7}$$

We will refer to the deprojected values as $\mathrm{R}_{bar,1}^{dep}$ and $\mathrm{R}_{bar,2}^{dep}$. We used the Hubble law to estimate the distance to each galaxy, and transform our measurements from arcsec to kpc. In table 2, we show the measurements for the bar length before and after deprojection, as well as their PA.

Table 2: Bar length of our sample

Galaxy (1)	i [°] (2)	PA$_{bar}$ [°] (3)	R$_{bar,1}$ [arcsec] (4)	R$_{bar,2}$ [arcsec] (5)	R$^{dep}_{bar,1}$ [kpc] (6)	R$^{dep}_{bar,2}$ [kpc] (7)
7495-12704	53.4	-35.9	5.4	8.4	4.0	5.8
7962-12703	66.1	50.2	11.7	15.2	13.5	18.8
7990-12704	41.8	81.2	11.3	14.0	6.1	7.6
8135-6103	46.2	5.6	8.2	11.3	9.2	12.7
8243-12704	60.4	30.8	5.3	6.7	3.0	3.7
8256-6101	51.6	59.5	5.8	7.0	4.5	5.4
8257-3703	58.5	-45.9	4.9	6.7	3.1	4.8
8312-12704	45.9	-28.6	6.5	9.2	5.2	7.5
8313-9101	38.6	-24.4	3.4	4.0	3.1	3.7
8317-12704	66.7	-52.6	6.5	8.0	12.4	15.1
8318-12703	55.2	87.0	5.0	6.2	5.5	7.3
8341-12704	23.3	79.5	6.9	8.5	4.3	5.5
8439-6102	48.4	26.3	4.9	6.9	3.6	5.4
8439-12702	55.2	-35.2	6.0	7.0	5.5	6.4
8453-12701	39.3	44.4	5.9	6.5	3.6	3.9
NGC5205	56.0	-71.9	11.0	12.7	2.1	2.4
NGC5406	46.0	56.3	18.1	20.4	8.6	10.1
NGC6497	61.3	-28.5	8.5	10.4	5.9	7.6

Col. (1): Galaxy. Col. (2): Disc inclination Col. (3): Bar PA. Col. (4): Inner bar radius. Col. (5): Outer bar radius. Col. (6): Deprojected inner bar radius. Col. (7): Deprojected outer bar radius

3.1.4. Kinematic position angle

In practice, the measurement of these orientation parameters is not always straightforward. The presence of features like spiral arms, disc warps, field stars or companion galaxies can alter the orientation of the external isophotes. In those situations, a correct estimation of the orientation parameters should be self-consistent with the kinematic data (Fridman et al., 2005). There are numerous examples where the structural parameters of a galaxy obtained by a photometric analysis are not necessary the same as the ones obtained using its kinematics. Several examples have been found using integral-field spectroscopy data; (e.g. Emsellem et al., 2004; Krajnović et al., 2011; Barrera-Ballesteros et al., 2014, 2015; Allen et al., 2015; Jin et al., 2016).

To obtain a rough estimation of the disc PA$_{kn}$we look for the zero-velocity line (ZVL) (i.e. the line where the galaxy moves with velocity $\sim V_{sys}$) in the stellar LOS-velocity map. To fit this line we used spaxels close to the photometric center, and whose velocities were within a window of $\pm 0.08 V_{max}$ around V_{sys}, where V_{max} is the maximum velocity inside the LOS-velocity map. Other velocities windows were tested, however this value was more consistent between different galaxies. These spaxels are shown in Figure 8 as grey dots, and the ZVL as a segmented black line. PA$_{kn}$is obtained by rotating the ZVL 90°.

PA$_{kn}$provides the orientation of the disc in the central region, however can be heavily affected by the non-circular motions of the bar. For this reason, PA$_{ph}$should be more reliable, while the PA$_{kn}$should be used only to confirm the photometric measurement. If both PA$_{ph}$and PA$_{kn}$are similar, we can be confident in our estimation of Ω_{bar}. As we will see in next chapter, the cases where the difference in PA is greater than 5° can produce significantly different results in Ω_{bar}. In the Chapter 5 we will discuss in detail what causes these differences in PA. Table 3 shows the our measurements of both PA$_{ph}$and PA$_{kn}$as well as the difference between them.

Table 3: Disc photometric and kinematic PA of our sample

Galaxy (1)	PA_{ph} [°] (2)	PA_{kn} [°] (3)	ΔPA [°] (4)
7495-12704	-8.6 ± 0.4	-6.3 ± 0.7	2.4
7962-12703	37.6 ± 0.8	35.1 ± 1.3	2.6
7990-12704	75.9 ± 3.7	67.8 ± 1.4	8.1
8135-6103	71.5 ± 3.5	35.2 ± 1.3	36.2
8243-12704	24.5 ± 0.8	14.6 ± 1.0	9.9
8256-6101	-55.4 ± 1.3	-46.5 ± 1.1	8.9
8257-3703	-24.1 ± 0.7	-22.6 ± 1.4	1.5
8312-12704	31.4 ± 2.0	37.7 ± 1.0	6.3
8317-12704	-72.8 ± 0.9	-71.8 ± 2.1	1.0
8313-9101	-69.8 ± 1.6	-67.6 ± 1.7	2.2
8318-12703	53.5 ± 1.0	54.7 ± 0.7	1.2
8341-12704	60.7 ± 6.5	48.1 ± 2.0	12.6
8439-6102	45.6 ± 0.5	42.2 ± 1.0	3.4
8439-12702	30.2 ± 0.5	32.9 ± 0.8	2.8
8453-12701	-80.5 ± 2.0	-59.9 ± 2.0	20.7
NGC5205	-10.3 ± 1.5	-9.0 ± 3.3	1.2
NGC5406	-67.1 ± 0.7	-55.4 ± 1.3	11.7
NGC6497	-70.3 ± 0.7	-59.3 ± 3.6	11.0

Col. (1):Galaxy, Col. (2): Photometric PA. Col. (3): Kinematic PA. Col. (4): Difference in PA

3.1.5. Rotation curve analysis with Velfit

In general, the velocity of stars in the disc can be decomposed in a tangential V_t and radial V_r components, relative to any center (preferably the galaxy kinematic center). Any perturbation to the velocity field can be expressed in a Fourier series around a radius r:

$$V_t(r,\theta) = \bar{V}_t(r) + \sum_{m=1}^{\infty} V_{m,t} \cos\left[m\theta + \theta_{m,t}(r)\right] \tag{3.8}$$

$$V_r(r,\theta) = \bar{V}_r(r) + \sum_{m=1}^{\infty} V_{m,r} \cos\left[m\theta + \theta_{m,r}(r)\right] \tag{3.9}$$

where $\bar{V}_t$ and $\bar{V}_r$ are the mean orbital speeds, $V_{m,t}$ and $V_{m,r}$ are the amplitudes of the m distortions, θ is the azimuthal angle, and $\theta_{m,t}$ and $\theta_{m,r}$ are their relative phases (Schoenmakers et al., 1997). In particular bars produce strong bysymmetric distortions to the potential and dominate over the $m = 2$ terms.

A simple model for the rotation curve consist of using a single slit spectrum along the major axis of the galaxy and setting $V_{obs} = V_{sys} + V(r) \sin i$. However this assumes every perturbation is negligible, and there are no changes in the orientation of the field (van den Bosch & Swaters, 2001; Swaters et al., 2003; Rhee et al., 2004; de Blok, 2005). When a two-dimensional velocity map is available a tilted ring model (Rogstad et al., 1974; Begeman, 1987) provides a best-fit model with three free parameters: PA, inclination and circular velocity. The tilted ring model is ideal when modeling discs that may be warped but doesn't take into account non-cicular motions.

The tool *velfit* is able to model non-axisymmetric motions by assuming a flat disc (fixed inclination) and distortion with a fixed orientation (Spekkens & Sellwood, 2007; Sellwood & Sánchez, 2010). Based on these assumptions, *velfit* tries to fit equation 3.10, by minimizing the χ^2 function 3.11:

$$V_{model} = V_{sys} + \sin i \left[\, \bar{V}_t \cos\theta - V_{m,t} \cos m\,(\theta - \phi_b) \cos\theta - V_{m,r} \sin m\,(\theta - \phi_b) \sin\theta \,\right] \tag{3.10}$$

$$\chi^2 = \sum_{n=1}^{N} \left(\frac{V_{obs}(x,y) - \sum_{k=1}^{K} \omega_{k,n} V_k}{\sigma_n} \right) \tag{3.11}$$

where ϕ_b is the orientation of the distortion relative to the projected major axis, V_k are tabulated values of the model and $\omega_{k,n}$ are weights given by the interpolation between V_k and V_{obs}. To minimize χ^2 *velfit* searches the optimal center, the systemic velocity, the disc inclination and orientation and the distortion orientation. We used the geometric parameters obtained with *Ellipse* as a first guest for these parameters.

Velfit uses a Levenberg Marquardt (LM) algorithm as a minimization technique, which uses a maximum likelihood approach to answer the question: How likely is the data set given a set of geometric parameters?. This routine minimizes the χ^2 maximum likelihood estimator by using a gradient search through parameter space. The concern with least-squared approaches is that for data sets with less than optimal sampling, corresponding to many local minima in χ^2 space, the LM routine is sensitive to initial guesses and is easily trapped. To solve this problem we implement a Bayesian technique and a Markov-chain Monte Carlo (MCMC) that provides a method of surveying the parameter space that rapidly converges to the posterior probability distribution of the input parameters using the Metropolis Hastings algorithm.

As the galaxy evolves, the random velocities of the old stellar populations increase while the mean rotation velocity decrease. The difference between the circular velocity of a set of young stars with perfectly circular orbits and other populations is known as the *asymmetric drift*, which can account for a difference of $\approx 10-30\,\%$ of the maximum rotation speed (Martinsson et al., 2013). This is the reason why ionized gas is a better tracer for modeling the rotation curve. In this thesis we used the H_α velocity maps to model the rotation curve, except for manga-7990-12704 which had a poor quality map. Instead, for this particular galaxy we used the stellar velocity map.

The kinematic orientation obtained by the best *velfit* model depends on the size of the region of the galaxy to be fitted. If a small region around the center is used, the *velfit* orientation is closer to PA_{kn}. Extending the velfit model to outer radius changes the orientation to values closer to PA_{ph}. For this reason, we will only use $\mathrm{PA}_{kn}$and PA_{ph}, and use *velfit* only for the rotation curve model.

To extrapolate the data to further radius we modeled the rotation curve with a basic 2-parameters arctan function shown in equation 3.12 (Courteau, 1997). This simple model assumes the rotation curve flattens at a transition radius r_t, and reaches an asymptomatic velocity V_c. We fitted the model curve using the LM algorithm. The resulting rotation curves for our sample are shown in Figure 10.

$$V(r) = V_{sys} + \frac{2}{\pi} V_c \ \mathrm{arctan}\left(\frac{r - r_0}{r_t}\right) \tag{3.12}$$

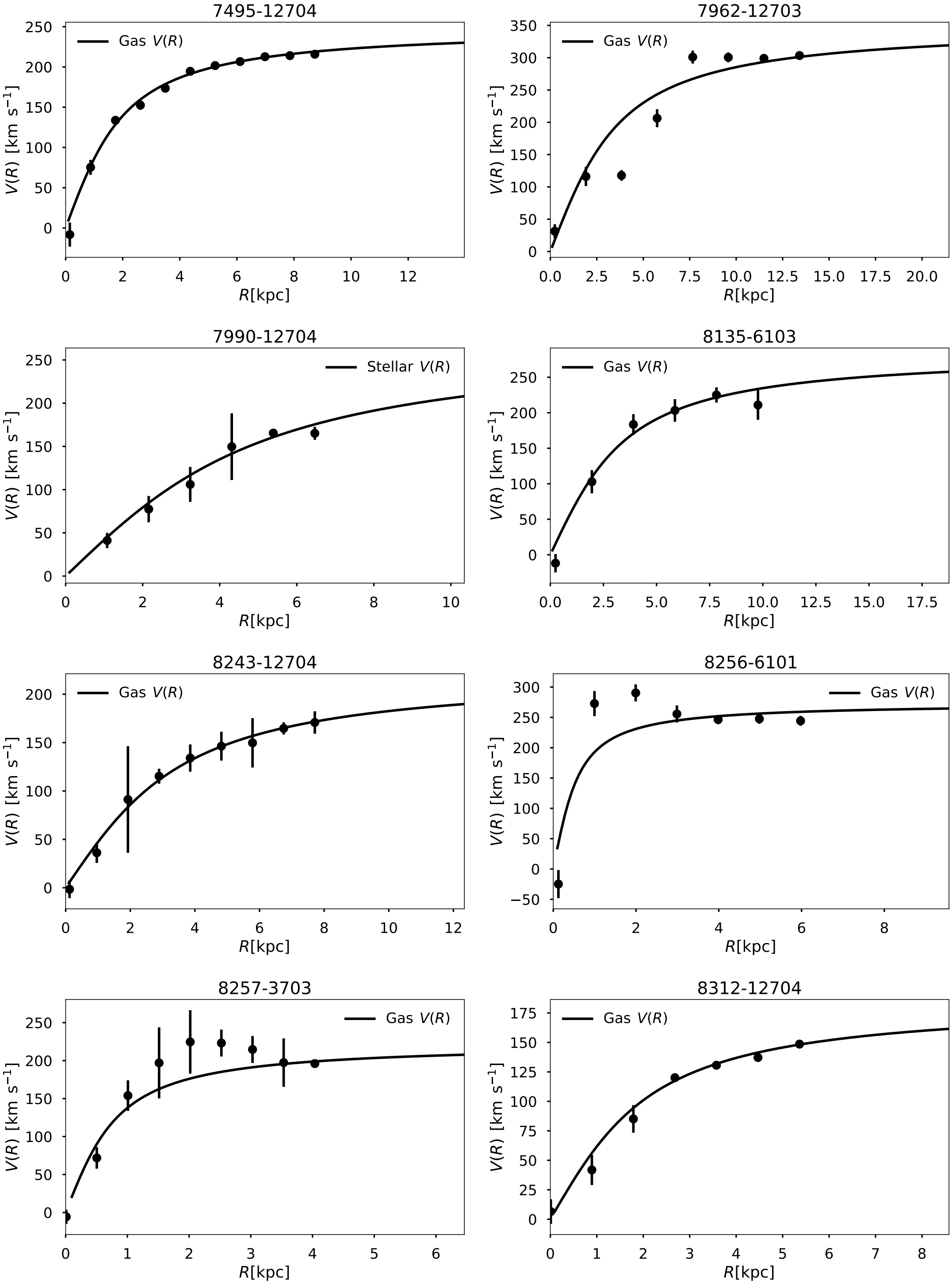
7495-12704
Gas $V(R)$
7962-12703
Gas $V(R)$
7990-12704
Stellar $V(R)$
8135-6103
Gas $V(R)$
8243-12704
Gas $V(R)$
8256-6101
Gas $V(R)$
8257-3703
Gas $V(R)$
8312-12704
Gas $V(R)$
$V(R)$ [km s^{-1}]
R[kpc]

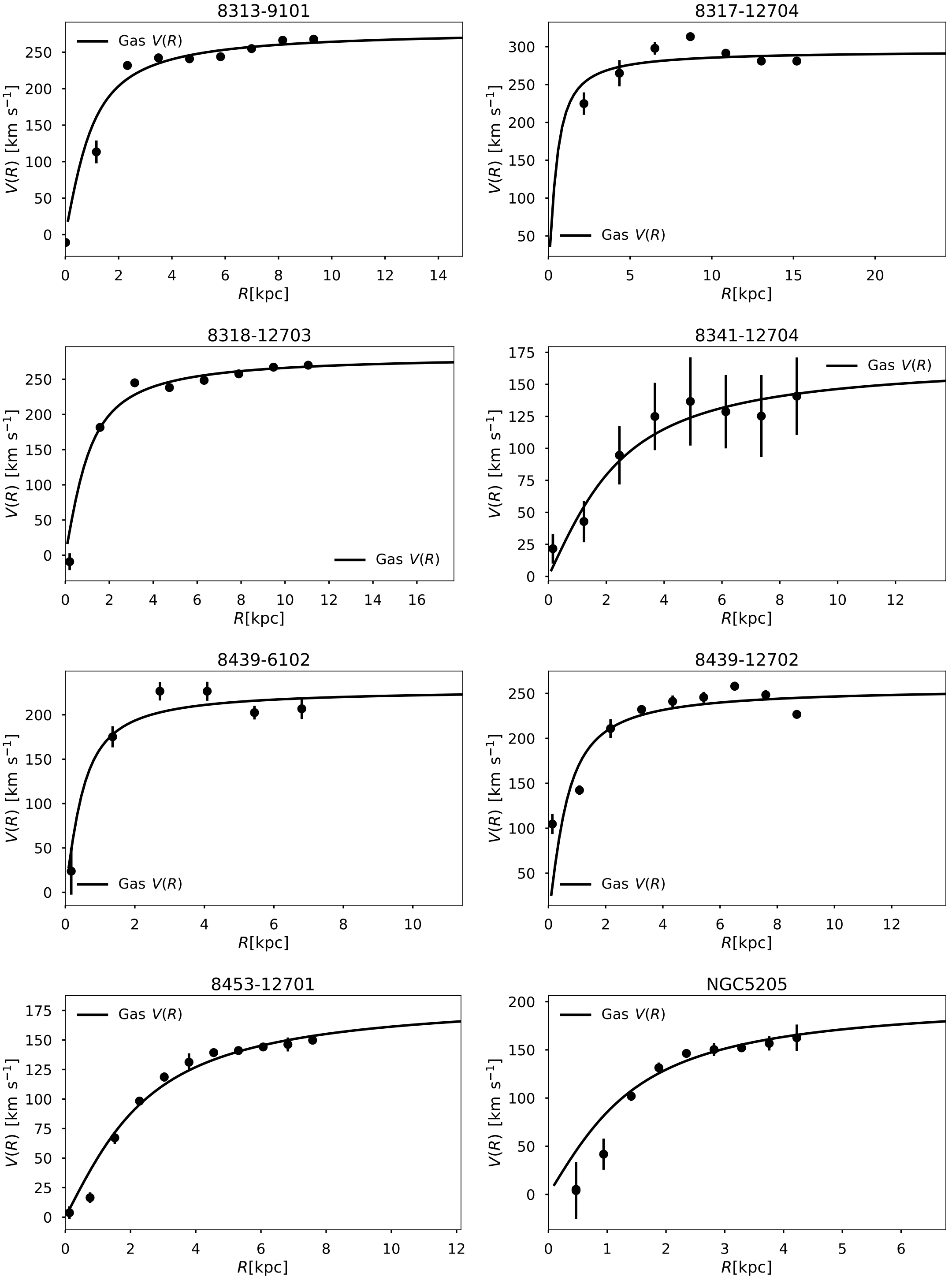
8313-9101
8317-12704
8318-12703
8341-12704
8439-6102
8439-12702
8453-12701
NGC5205
Gas $V(R)$
$V(R)$ [km s^{-1}]
R[kpc]

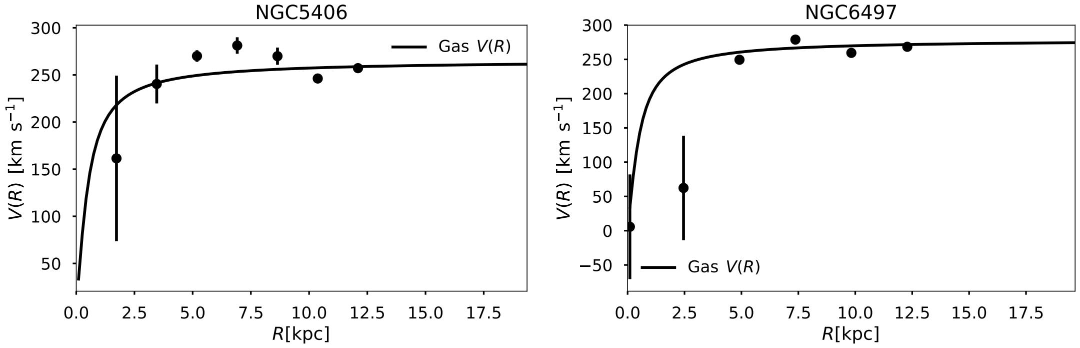

Figure 10: Rotation curves of our sample. The black points show the best *velfit* at different radius, taking into account a bysymmetric perturbation in the mode $m = 2$. The rotation cuve was fitted using basic 2-parameters arctan function. All models were perfomed over the H_α velocity maps, except for manga-7990-12704 were the stellar velocity map was used.

3.2. Number, length and separation between pseudo slits

Choosing the number, length and separation between pseudo slits is not trivial. In principle, we want to maximize the number of slits to perform the TW integrals to have more points to fit Ω_{bar}. We also want to maximize the length to reach the axisymmetric disc where the TW integrals cancel out. Finally the slits should be separated enough to prevent the use of repeated information that could reduce artificially the error.

To estimate the TW integrals we performed a numerical integration over the stellar flux and velocity maps. We have to take into account that these maps are formed over a 2D array of spaxels and that the orientation of the slits with respect this grid can have some important effects. For example, the integration step should be small enough to pick up the contribution from spaxels that cross the slits marginally. In this work we used an integration step of 0.1 spaxels. Another example is the separation between slits. When these are aligned with the grid, a separation of 1 spaxel is enough to prevent repeated spaxels between two consecutive pseudo slits. However at other orientations we choose to increase de separation by $1/\cos\theta$ where

$$\theta = \begin{cases} PA - 90, & \text{if } 45^\circ < PA < 90^\circ \\ PA, & \text{if} - 45^\circ < PA < 45^\circ \\ PA + 90, & \text{if} - 90^\circ < PA < -45^\circ \end{cases} \tag{3.13}$$

This separation guarantees a separation of 1 spaxel when the psudo-slits are aligned with the grid of spaxels, and increases to $\sqrt{2}$ when these are oriented 45° with respect to the grid.

We considered keeping the pseudo slits length constant, however this procedure presented two problems: (1) Increasing the number of slits requires reducing the length, so all of them can fit inside the MaNGA and CALIGA hexagons and (2) by reducing the length we are losing valuable information at the edges of the hexagons. Instead we choose to keep the length variable, letting each pseudo slit to extend as far as the hexagon allows minus 3 spaxels. Is important to keep the length equal to both sides, so the symmetry of the TW integrals is preserved.

Increasing the number of pseudo slits reduces the least square fitting error to determine Ω_{bar}. However in most galaxies the TW integrals usually stop following a linear trend at outer radius. This mostly happens when the pseudo slits reach the outside of the bar region, approximately at $R_{bar,1}$. Thus the number of pseudo slits we used was the minimum between n: the maximum number of slits where the TW integrals follow a linear trend, and m: the maximum number of pseudo slits that can be placed inside a circle with radius $R_{bar,1}$

Capítulo 4

Results

In this chapter we will discuss our main results, including our measurements of Ω_{bar}, and the corotation radius. The TW method is well known for having big uncertainties. Noticed by Debattista (2003) an error in the PA of $\delta PA = 5°$ can produce errors in Ω_{bar} of 50 %. One of the main advantages of using IFU data is that we can repeat the measurement of the TW integrals changing slightly various parameters. Among our sample we found three main sources of uncertainty applying the TW method (1) the PA error, (2) the galaxy center, and (3) the pseudo slits length. To disentangle these errors and estimate their magnitude we performed various test changing these parameters individually.

Once we have an accurate estimation for Ω_{bar} we can compare it with the angular rotation curve of the disc and find the corotation radius. We performed a monte carlo simulation using the uncertainties in Ω_{bar} and R_{bar}^{dep} to find the probability distribution function (PDF) of the parameter $\mathcal{R}$. All galaxies in our sample are consistent with hosting a fast bar.

4.1. The uncertainty sources

4.1.1. The centering error

We found the galaxy center using the center of mass weighting the stellar flux. In all our sample the associated error to this center was less than 0.5 spaxels. However in some orientations, this small error could change the value of the TW integrals significantly. To estimate this error, we changed the center 1000 times, using a 2D Gaussian distribution with $\sigma = 1$ spaxels. Then we compute both TW integrals while keeping the PA, the number of slits and the length of the slits constant.

In Figure 11 we show the resulting KI and PI measured at PA_{ph}(in blue) and PA_{kn}(in red). The plotted values are the median and the error bars correspond to the first and third quartiles of each slit. In most galaxies the associated error to the KI and PI are similar and relatively small. However, in some cases the PI error presents a significantly bigger dispersion than the KI. Using this error we used a weighted least squares fit to measure $\Omega_{bar} \times \sin i$. From here after, we will refer to the the associated error of the fit as $\delta\Omega_{Cen}$.

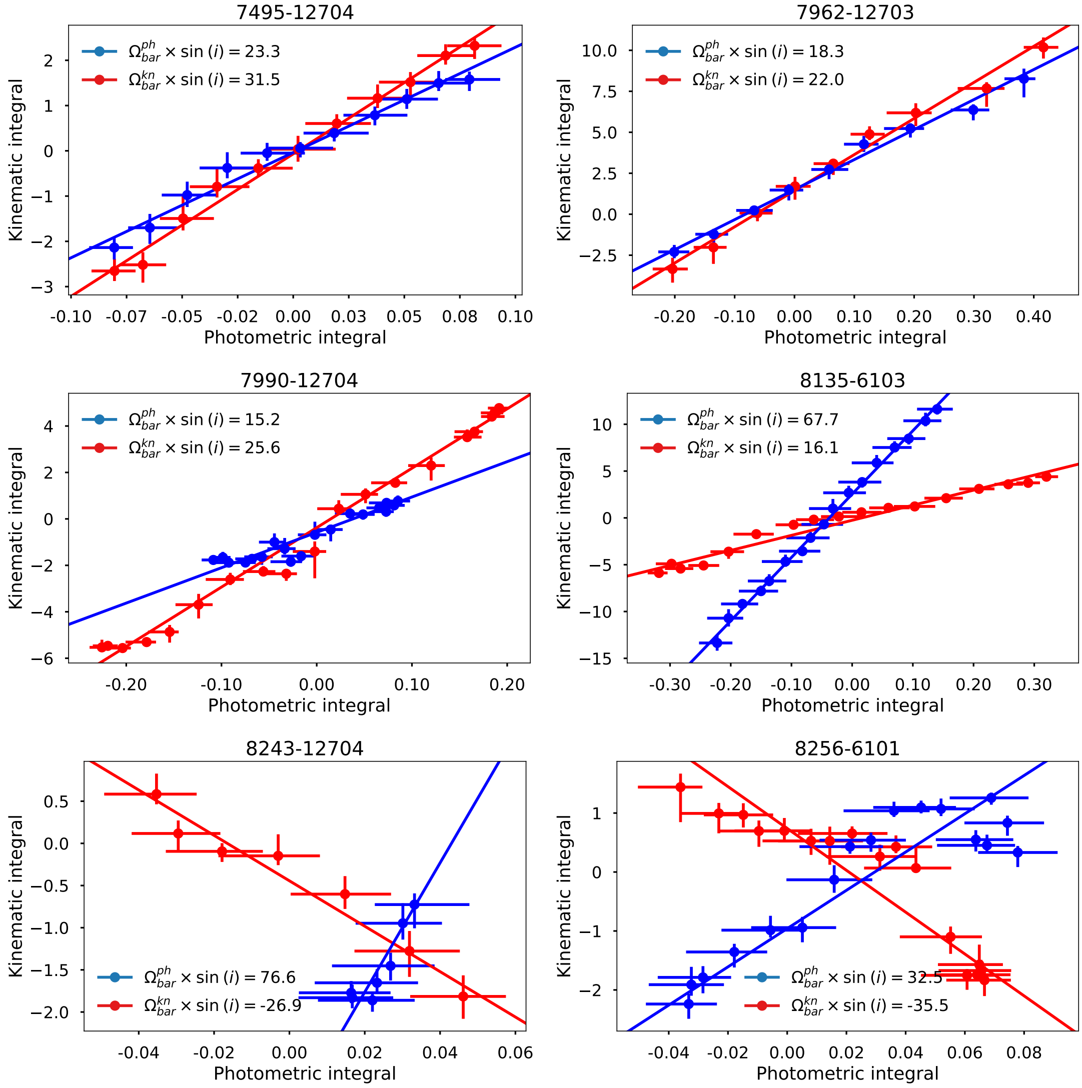

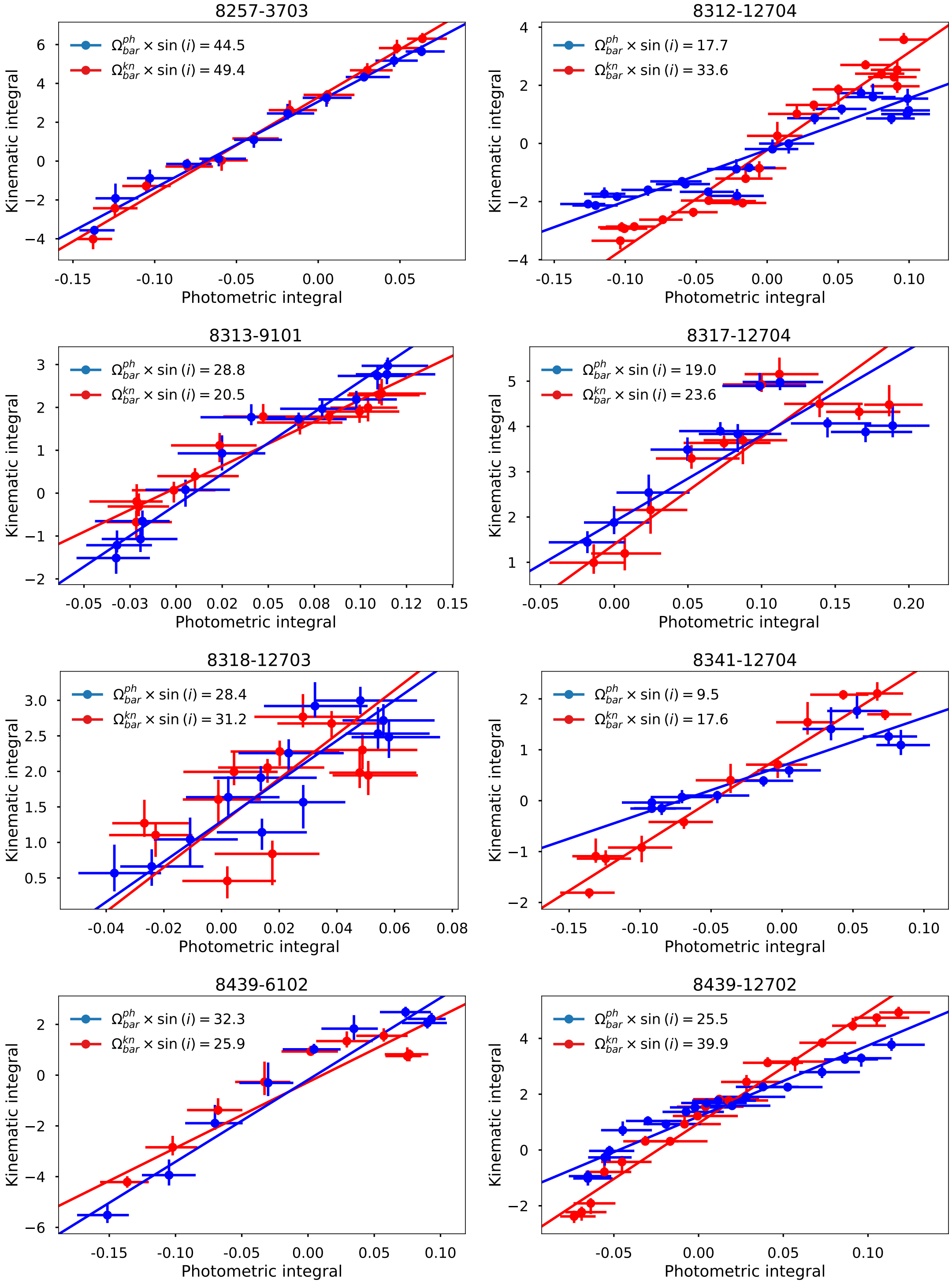
8257-3703
$\Omega_{bar}^{ph} \times \sin(i) = 44.5$
$\Omega_{bar}^{kn} \times \sin(i) = 49.4$
8312-12704
$\Omega_{bar}^{ph} \times \sin(i) = 17.7$
$\Omega_{bar}^{kn} \times \sin(i) = 33.6$
8313-9101
$\Omega_{bar}^{ph} \times \sin(i) = 28.8$
$\Omega_{bar}^{kn} \times \sin(i) = 20.5$
8317-12704
$\Omega_{bar}^{ph} \times \sin(i) = 19.0$
$\Omega_{bar}^{kn} \times \sin(i) = 23.6$
8318-12703
$\Omega_{bar}^{ph} \times \sin(i) = 28.4$
$\Omega_{bar}^{kn} \times \sin(i) = 31.2$
8341-12704
$\Omega_{bar}^{ph} \times \sin(i) = 9.5$
$\Omega_{bar}^{kn} \times \sin(i) = 17.6$
8439-6102
$\Omega_{bar}^{ph} \times \sin(i) = 32.3$
$\Omega_{bar}^{kn} \times \sin(i) = 25.9$
8439-12702
$\Omega_{bar}^{ph} \times \sin(i) = 25.5$
$\Omega_{bar}^{kn} \times \sin(i) = 39.9$
Kinematic integral
Photometric integral

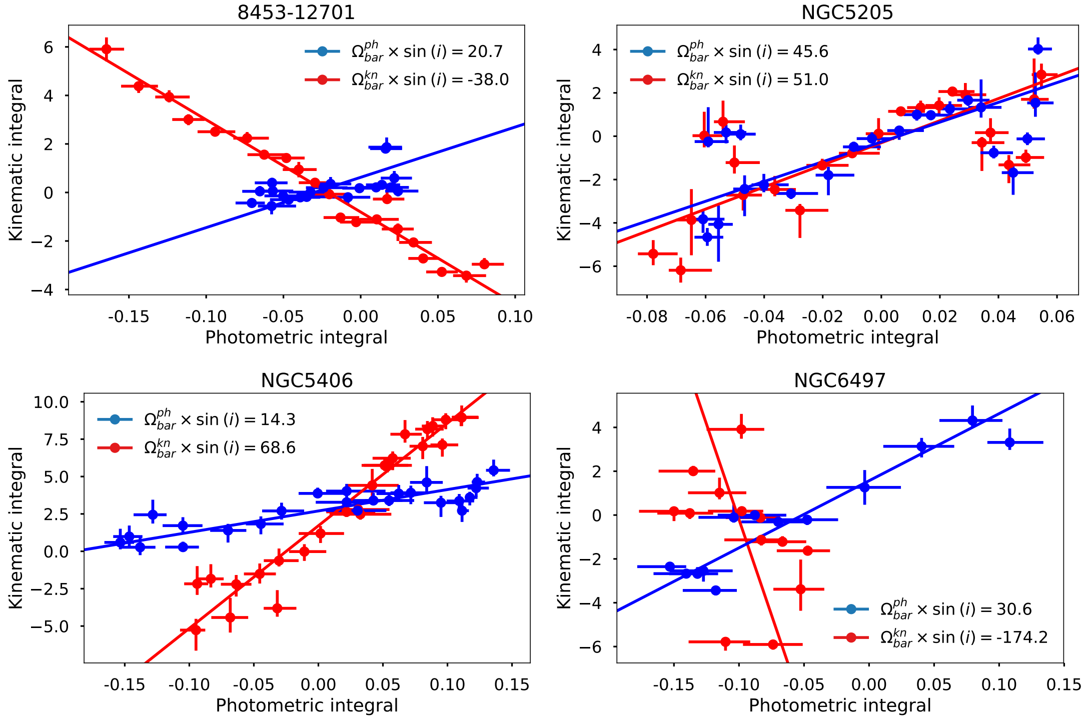

Figure 11: Kinematic integral vs. Photometric integral. The ploted values correspond to the median, and the first and third quartiles after randomly changing the center 1000 times. The measurements performed at PA$_{ph}$and PA$_{kn}$are shown with blue and red respectively.

4.1.2. The PA error

We repeated the measurement of Ω_{bar} for 200 angles equally spaced between the minimum and maximum of PA$_{ph}$and PA$_{kn}$±7°. This range provides a good sample to study the behaviour of Ω_{bar} within the errors associated to both PAs. At each angle we first estimated $\delta\Omega_{Cen}$ with the procedure described above. We will call Ω_{bar}^{ph} and Ω_{bar}^{kn} the median value of Ω_{bar} at the regions enclosed by PA$_{ph}$and PA$_{kn}$within their respective errors. We used the standard deviation at this regions to estimate the PA error. From hereafter we will refer to it as $\delta\Omega_{PA}$.

In Figure 12 we show Ω_{bar} vs PA for each galaxy in our sample. The orange dots show the best least square fit for Ω_{bar}, and the orange shaded regions shows the associated error $\delta\Omega_{Cen}$. The blue and red lines show the values of Ω_{bar}^{ph} and Ω_{bar}^{kn} respectively. The shaded regions show the standard deviation in these regions.

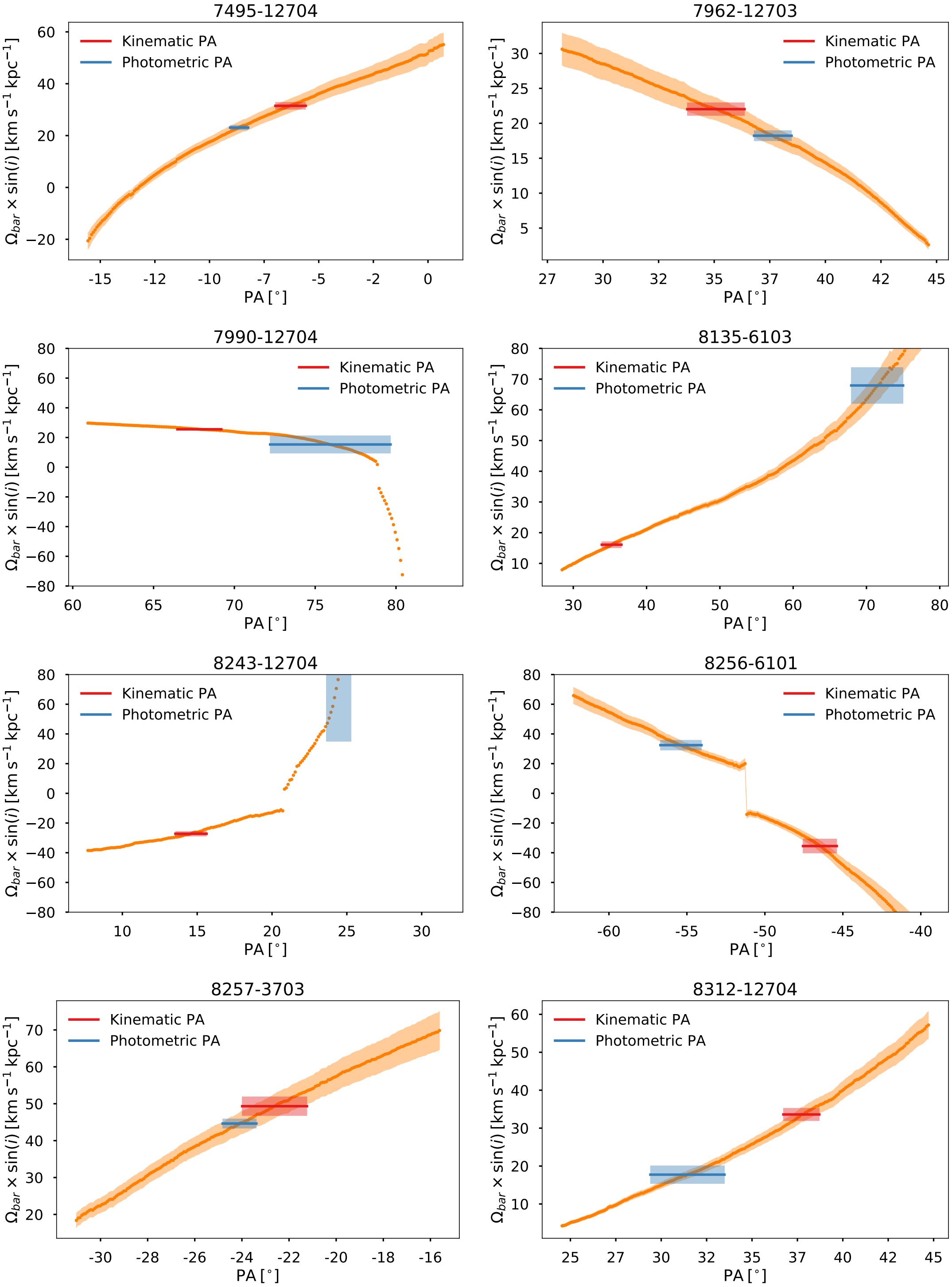
7495-12704
Kinematic PA
Photometric PA
$\Omega_{bar} \times \sin(i)$ [km s^{-1} kpc^{-1}]
60
40
20
0
−20
-15
-12
-10
-7
-5
-2
0
PA [°]
7962-12703
Kinematic PA
Photometric PA
$\Omega_{bar} \times \sin(i)$ [km s^{-1} kpc^{-1}]
30
25
20
15
10
5
27
30
32
35
37
40
42
45
PA [°]
7990-12704
Kinematic PA
Photometric PA
$\Omega_{bar} \times \sin(i)$ [km s^{-1} kpc^{-1}]
80
60
40
20
0
−20
−40
−60
−80
60
65
70
75
80
PA [°]
8135-6103
Kinematic PA
Photometric PA
$\Omega_{bar} \times \sin(i)$ [km s^{-1} kpc^{-1}]
80
70
60
50
40
30
20
10
30
40
50
60
70
80
PA [°]
8243-12704
Kinematic PA
Photometric PA
$\Omega_{bar} \times \sin(i)$ [km s^{-1} kpc^{-1}]
80
60
40
20
0
−20
−40
−60
−80
10
15
20
25
30
PA [°]
8256-6101
Kinematic PA
Photometric PA
$\Omega_{bar} \times \sin(i)$ [km s^{-1} kpc^{-1}]
80
60
40
20
0
−20
−40
−60
−80
-60
-55
-50
-45
-40
PA [°]
8257-3703
Kinematic PA
Photometric PA
$\Omega_{bar} \times \sin(i)$ [km s^{-1} kpc^{-1}]
70
60
50
40
30
20
-30
-28
-26
-24
-22
-20
-18
-16
PA [°]
8312-12704
Kinematic PA
Photometric PA
$\Omega_{bar} \times \sin(i)$ [km s^{-1} kpc^{-1}]
60
50
40
30
20
10
25
27
30
32
35
37
40
42
45
PA [°]

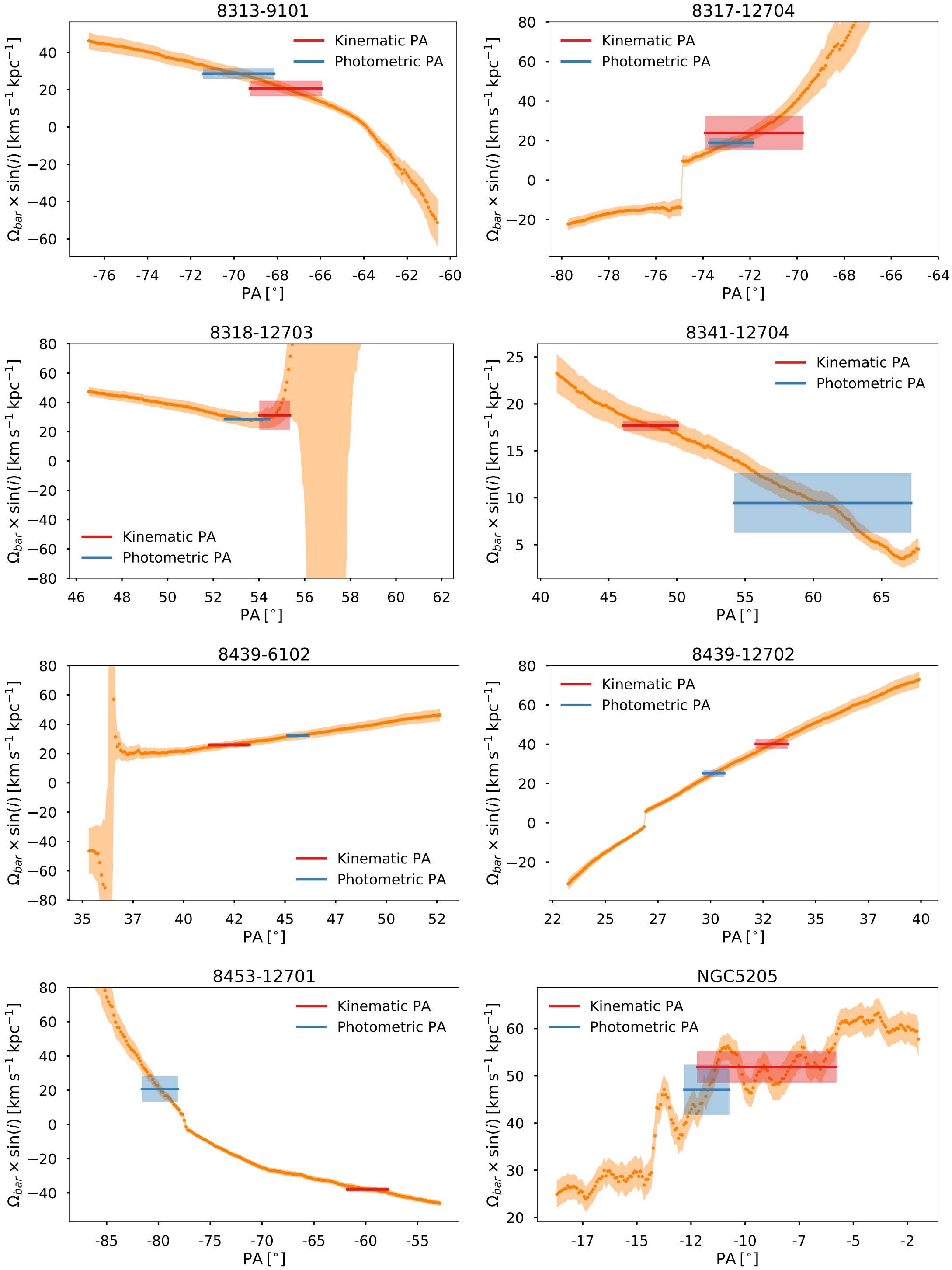
8313-9101
$\Omega_{bar} \times \sin(i)$ [km s^{-1} kpc^{-1}]
40
20
0
−20
−40
−60
Kinematic PA
Photometric PA
-76
-74
-72
-70
-68
-66
-64
-62
-60
PA [°]
8317-12704
80
60
40
20
0
−20
Kinematic PA
Photometric PA
-80
-78
-76
-74
-72
-70
-68
-66
-64
PA [°]
8318-12703
80
60
40
20
0
−20
−40
−60
−80
Kinematic PA
Photometric PA
46
48
50
52
54
56
58
60
62
PA [°]
8341-12704
25
20
15
10
5
Kinematic PA
Photometric PA
40
45
50
55
60
65
PA [°]
8439-6102
80
60
40
20
0
−20
−40
−60
−80
Kinematic PA
Photometric PA
35
37
40
42
45
47
50
52
PA [°]
8439-12702
80
60
40
20
0
−20
Kinematic PA
Photometric PA
22
25
27
30
32
35
37
40
PA [°]
8453-12701
80
60
40
20
0
−20
−40
Kinematic PA
Photometric PA
-85
-80
-75
-70
-65
-60
-55
PA [°]
NGC5205
60
50
40
30
20
Kinematic PA
Photometric PA
-17
-15
-12
-10
-7
-5
-2
PA [°]

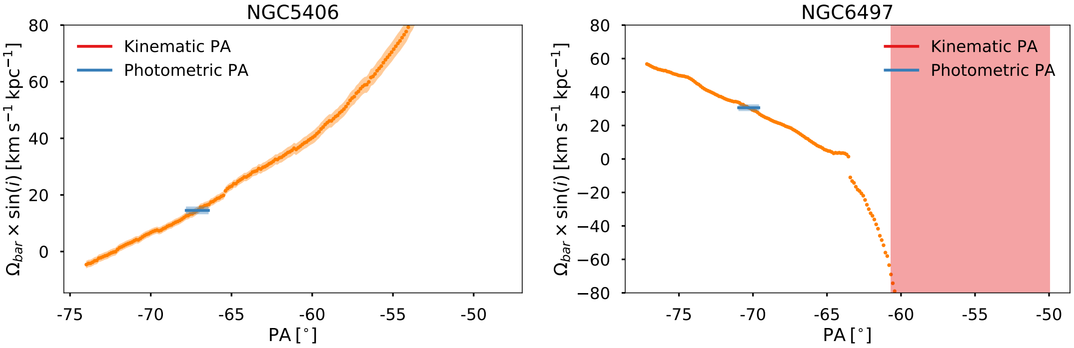

Figure 12: Bar pattern speed vs. position angle of our sample. The orange region show the measurement of Ω_{bar} with the uncertainty estimated as described at Section 4.1.1. The blue and red regions show the median value of Ω_{bar} and the standard deviation at the regions enclosed by the uncertainties of PA$_{ph}$and PA$_{kn}$.

We found along our sample that the sensibility to the PA is different for each galaxy. In some cases, the ratio between the TW integrals tends to an asymptote (7990-12704, 8243-12704, 8318-12703, 8439-6102, 8453-12701, NGC6497). In other galaxies, Ω_{bar} changes sign abruptly, while keeping the same magnitude (7990-12704, 8243-12704, 8256-6101, 8317-12704, 8439-6102, 8439-12702, NGC5406, NGC6497). Both behaviours can increase $\delta\Omega_{PA}$ dramatically. When selecting our sample we exclude galaxies were this behaviour was present exactly at the PA measured. In general the centring error increases at orientations where the asymptotes happen.

In most galaxies of our sample, the photometric and kinematic results are similar, however in some cases one of the measurements lies close to an asymptote and the resulting Ω_{bar} does not make physical sense (manga-8135-6102, manga-8243-12704, NGC5406, NGC6407). In the next Chapter we will discuss what causes this behaviour with more detail. From hereafter we will refer only to the photometric results, except for manga-8135-6103 and manga-8243-12704 were only the kinematic results makes physical sense.

4.1.3. The pseudo slits length error

In principle the TW integrals should cancel out when $X \to \infty$, when the axisymmetric part of the disc is reached and the stellar flux has decreased to zero. However since the MaNGA has a radial coverage between 1.5 and 2.5 effective radius, we can expect a systematic error due the length of the pseudo slits. To estimate this error, we performed the following test:

Let L_0 be the maximum length of the pseudo slits that can be fitted inside the observed hexagon as described in Section 3.2. In Figure 13 we show the relative error in Ω_{bar} produced by reducing the pseudo slits length L to different fractions of L_0. The

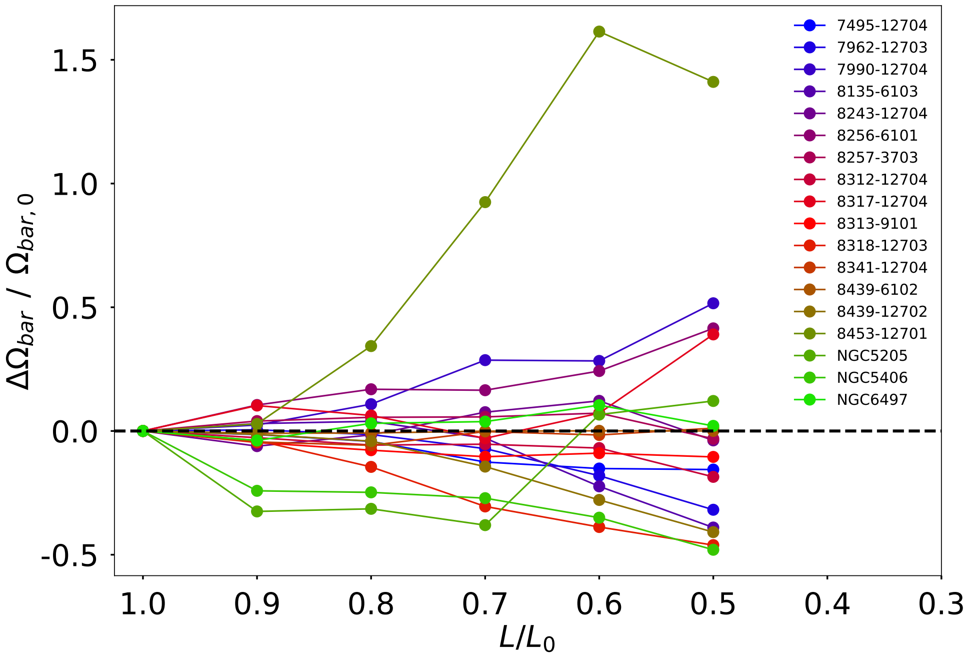

Figure 13: Relative error in Ω_{bar} vs. fractional pseudo slits length for our sample. The standard deviation at each step is $0.0, 0.07, 0.10, 0.16, 0.24, 0.28$.

standard deviation of the relative errors increases from 0.07 when pseudo slits are cut at $0.9L_0$ to 0.28 at $0.5L_0$.

The origin of this error is not clear. In principle, this error should be less important in galaxies where the ratio between the pseudo slits length and the bar radius ($L_0/R_{bar,1}$) is greatest. In those cases the the axisymmetric disc should be reached, and the TW integrals cancel out. To see if this was the case, we plotted in Figure 14 the relative error $\Delta\Omega_{bar}/\Omega_{bar,0}$ vs. $L_0/R_{bar,1}$, where $\Omega_{bar,0}$ is the bar pattern speed measured with the maximum pseudo slit length L_0. Galaxies less affected by the length error appear to be those with ratio $L_0/R_{bar,1} > 1.7$. In the next Chapter we will discuss the possible causes for this behaviour. For simplicity we used the relative error at $L = 0.8L_0$ for the length error and we will call it form hereafter as $\delta\Omega_{Len}$. These values are shown in Figure 14 with black stars.

All the uncertainty sources we found arise from the geometric nature of the TW method, are galaxy dependent and change at different PA. Given the complexity of the problem, we choose to add in quadrature each error source for the final estimation of $\delta\Omega_{bar}$. In table 4 we show the measurement of Ω_{bar} and the different error sources $\delta\Omega_{Cen}$, $\delta\Omega_{PA}$ and $\delta\Omega_{Len}$. In parenthesis we show their relative error. The dominant error source is different for each galaxy. Same as the figures 13 and 14, in this table we show Ω^{ph}_{bar}, except for manga-8135-6103 and manga-8243-12704, where we used Ω^{kn}_{bar}.

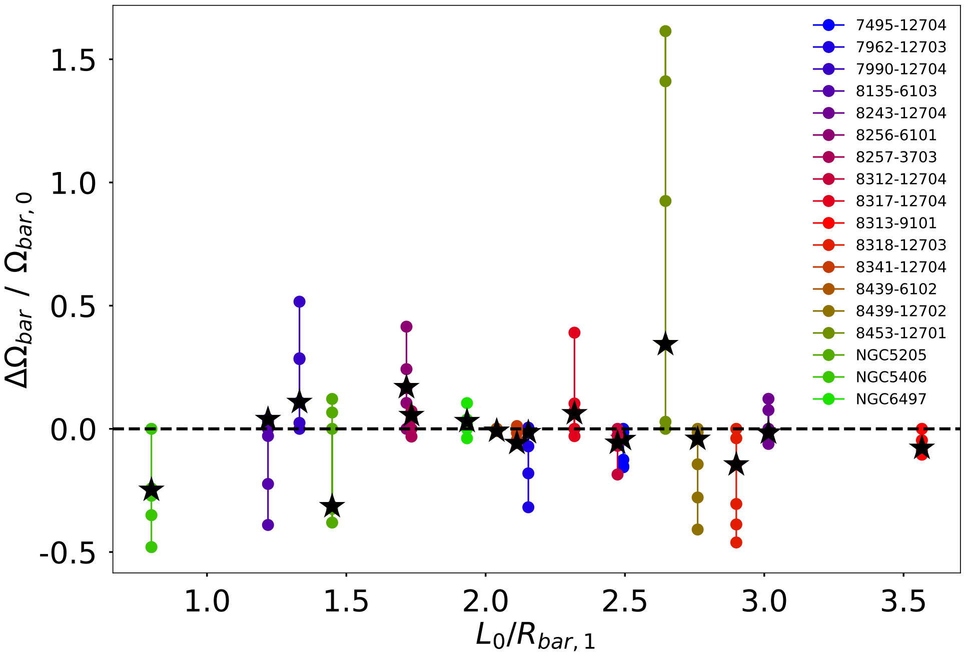

Figure 14: Reltive error vs $L_0/R_{bar,1}$. As in Figure 13, each point represent a measurement of Ω_{bar} using different fractions of pseudo slit length. Galaxies less afected by the length error are those with $L_0/R_{bar,1} > 1.7$. The black stars show the relative error when the pseudo slits measure $0.8L_0$.

Table 4: Bar pattern speed and the main error sources for our sample.

Galaxy	Ω_{bar} km s^{-1} kpc^{-1}	$\delta\Omega_{Cen}$ $\left(\frac{\delta\Omega_{Cen}}{\Omega_{bar}}\right)$ km s^{-1} kpc^{-1}	$\delta\Omega_{PA}$ $\left(\frac{\delta\Omega_{PA}}{\Omega_{bar}}\right)$ km s^{-1} kpc^{-1}	$\delta\Omega_{Len}$ $\left(\frac{\delta\Omega_{Len}}{\Omega_{bar}}\right)$ km s^{-1} kpc^{-1}
(1)	(2)	(3)	(4)	(5)
7495-12704	28.7 ± 3.2	2.8(0.10)	1.1(0.04)	-1.2(0.04)
7962-12703	19.9 ± 1.7	1.5(0.07)	0.8(0.04)	-0.3(0.01)
7990-12704	23.0 ± 9.3	1.4(0.06)	8.8(0.38)	2.5(0.11)
8135-6103	22.3 ± 1.8	0.8(0.04)	1.4(0.06)	0.9(0.04)
8243-12704	-31.3 ± 6.8	6.5(0.21)	1.9(0.06)	-0.5(0.02)
8256-6101	41.4 ± 9.2	4.1(0.10)	4.2(0.10)	7.0(0.17)
8257-3703	52.3 ± 4.8	3.5(0.07)	1.5(0.03)	2.9(0.06)
8312-12704	24.7 ± 3.8	1.4(0.06)	3.3(0.13)	-1.4(0.06)
8313-9101	46.0 ± 7.4	5.1(0.11)	4.5(0.10)	2.9(0.06)
8317-12704	20.5 ± 4.4	3.1(0.15)	2.6(0.13)	-1.6(0.08)
8318-12703	34.9 ± 7.9	6.0(0.17)	1.1(0.03)	-5.1(0.15)
8341-12704	23.9 ± 8.6	2.9(0.12)	8.0(0.34)	-1.4(0.06)
8439-6102	43.0 ± 3.8	3.7(0.09)	0.7(0.02)	-0.3(0.01)
8439-12702	30.7 ± 3.4	2.4(0.08)	2.0(0.07)	-1.3(0.04)
8453-12701	32.7 ± 17.0	4.8(0.15)	11.9(0.36)	11.2(0.34)
NGC5205	56.8 ± 19.3	3.6(0.06)	6.4(0.11)	-17.9(0.31)
NGC5406	20.2 ± 5.6	1.7(0.08)	1.8(0.09)	-5.0(0.25)
NGC6497	34.9 ± 3.8	3.1(0.09)	2.1(0.06)	1.1(0.03)

Col.(1) Galaxy. Col.(2) Bar pattern speed. Col.(3) Centering error. Col.(4) Position angle error. Col.(5) Pseudo slit length error. In parenthesis we show the relative error. For simplicity, we added in quadrature each error to estimate the final uncertainty of Ω_{bar}.

4.2. Corotation radius and parameter ℛ

To find R_{CR} we look for the intersection between Ω_{bar} and the disc angular velocity curve $V(R)/R$ as shown in Figure 15. In consistency with previous plots, the blue and red regions represent the photometric and kinematic measurements of Ω_{bar} respectively. The green region shows the deprojected bar radius, limited by $R^{dep}_{bar,1}$ and $R^{dep}_{bar,2}$.

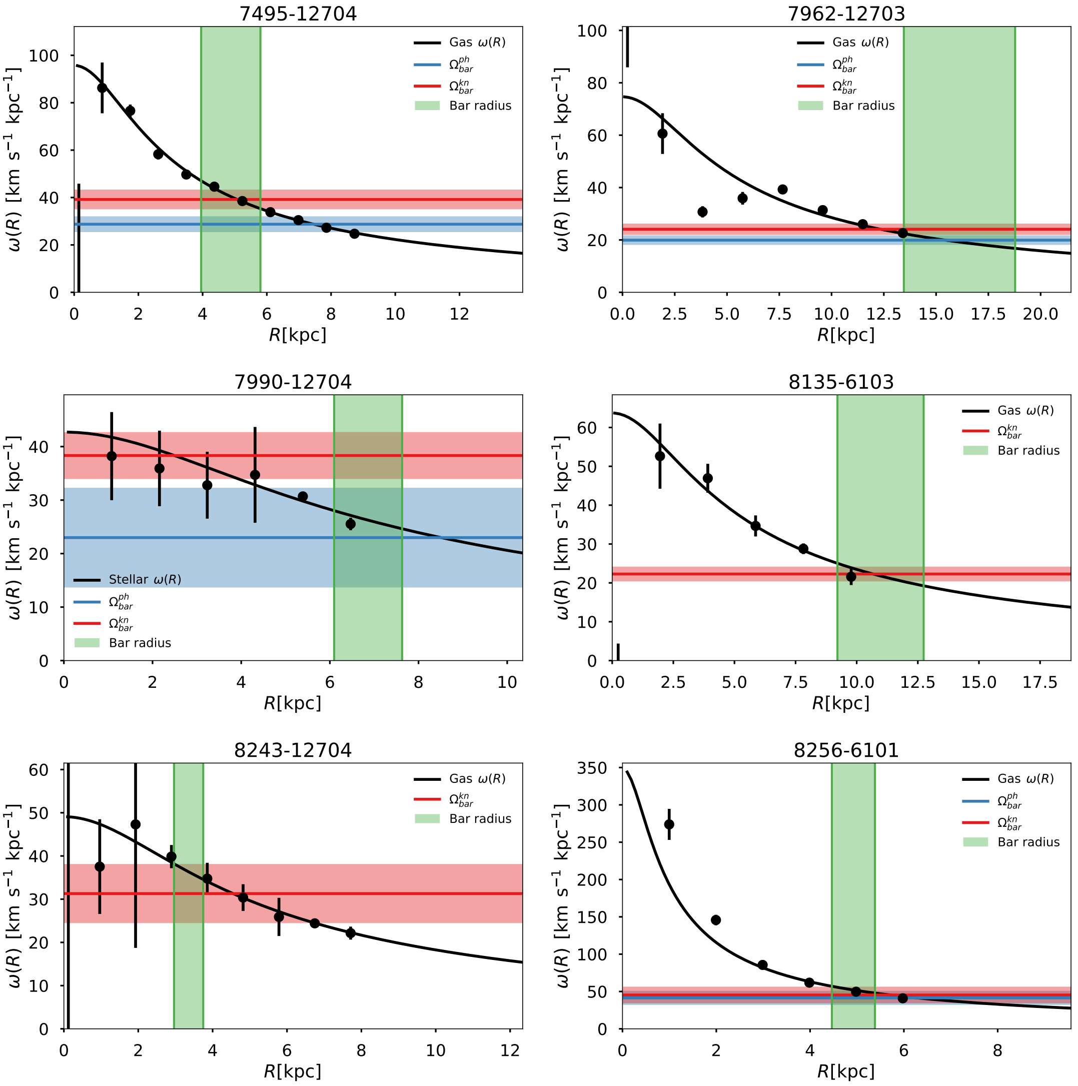

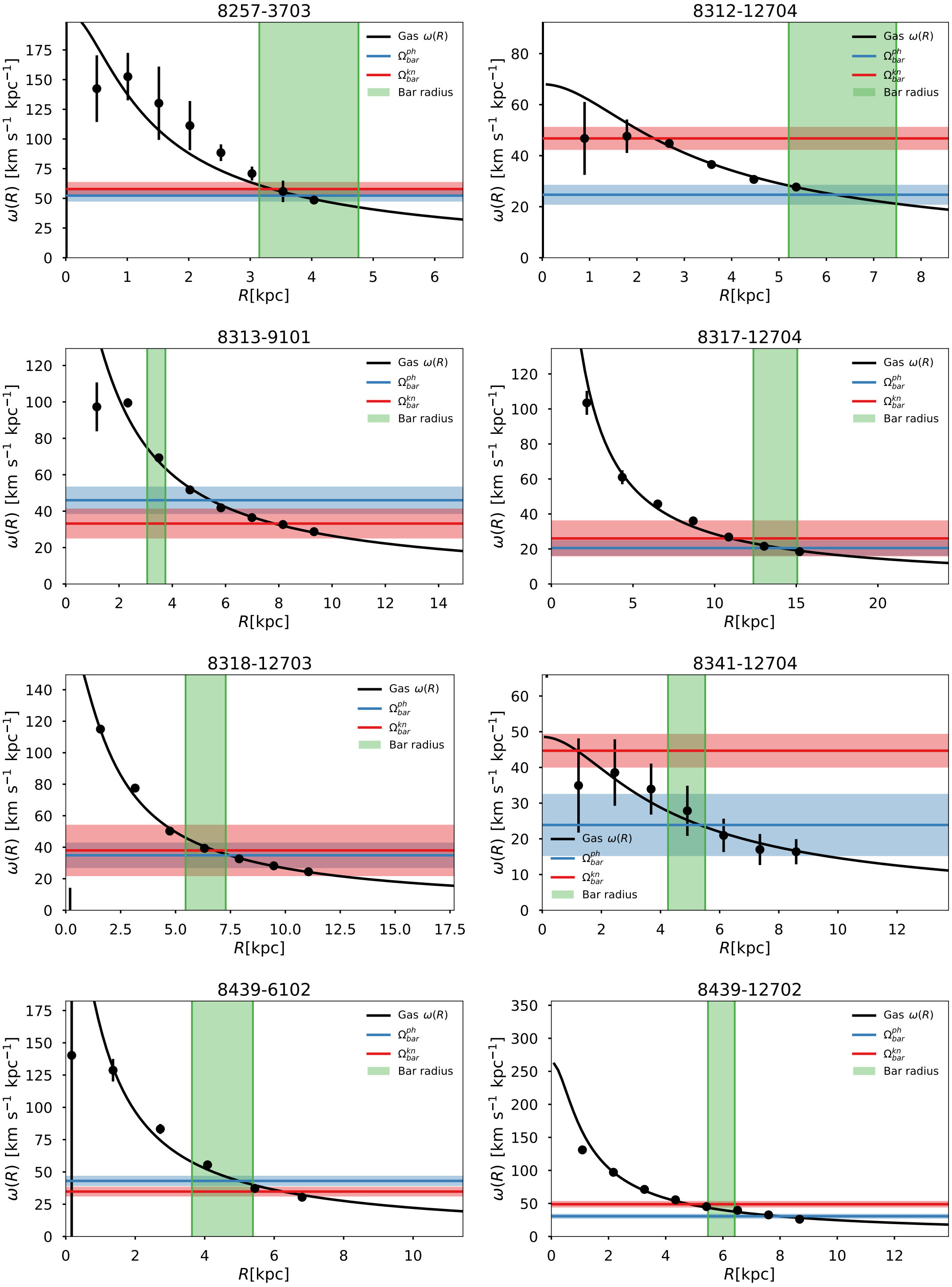
8257-3703
$\omega(R)$ [km s^{-1} kpc^{-1}]
0
25
50
75
100
125
150
175
0
1
2
3
4
5
6
R[kpc]
Gas $\omega(R)$
Ω_{bar}^{ph}
Ω_{bar}^{kn}
Bar radius
8312-12704
$\omega(R)$ [km s^{-1} kpc^{-1}]
0
20
40
60
80
0
1
2
3
4
5
6
7
8
R[kpc]
Gas $\omega(R)$
Ω_{bar}^{ph}
Ω_{bar}^{kn}
Bar radius
8313-9101
$\omega(R)$ [km s^{-1} kpc^{-1}]
0
20
40
60
80
100
120
0
2
4
6
8
10
12
14
R[kpc]
Gas $\omega(R)$
Ω_{bar}^{ph}
Ω_{bar}^{kn}
Bar radius
8317-12704
$\omega(R)$ [km s^{-1} kpc^{-1}]
0
20
40
60
80
100
120
0
5
10
15
20
R[kpc]
Gas $\omega(R)$
Ω_{bar}^{ph}
Ω_{bar}^{kn}
Bar radius
8318-12703
$\omega(R)$ [km s^{-1} kpc^{-1}]
0
20
40
60
80
100
120
140
0.0
2.5
5.0
7.5
10.0
12.5
15.0
17.5
R[kpc]
Gas $\omega(R)$
Ω_{bar}^{ph}
Ω_{bar}^{kn}
Bar radius
8341-12704
$\omega(R)$ [km s^{-1} kpc^{-1}]
0
10
20
30
40
50
60
0
2
4
6
8
10
12
R[kpc]
Gas $\omega(R)$
Ω_{bar}^{ph}
Ω_{bar}^{kn}
Bar radius
8439-6102
$\omega(R)$ [km s^{-1} kpc^{-1}]
0
25
50
75
100
125
150
175
0
2
4
6
8
10
R[kpc]
Gas $\omega(R)$
Ω_{bar}^{ph}
Ω_{bar}^{kn}
Bar radius
8439-12702
$\omega(R)$ [km s^{-1} kpc^{-1}]
0
50
100
150
200
250
300
350
0
2
4
6
8
10
12
R[kpc]
Gas $\omega(R)$
Ω_{bar}^{ph}
Ω_{bar}^{kn}
Bar radius

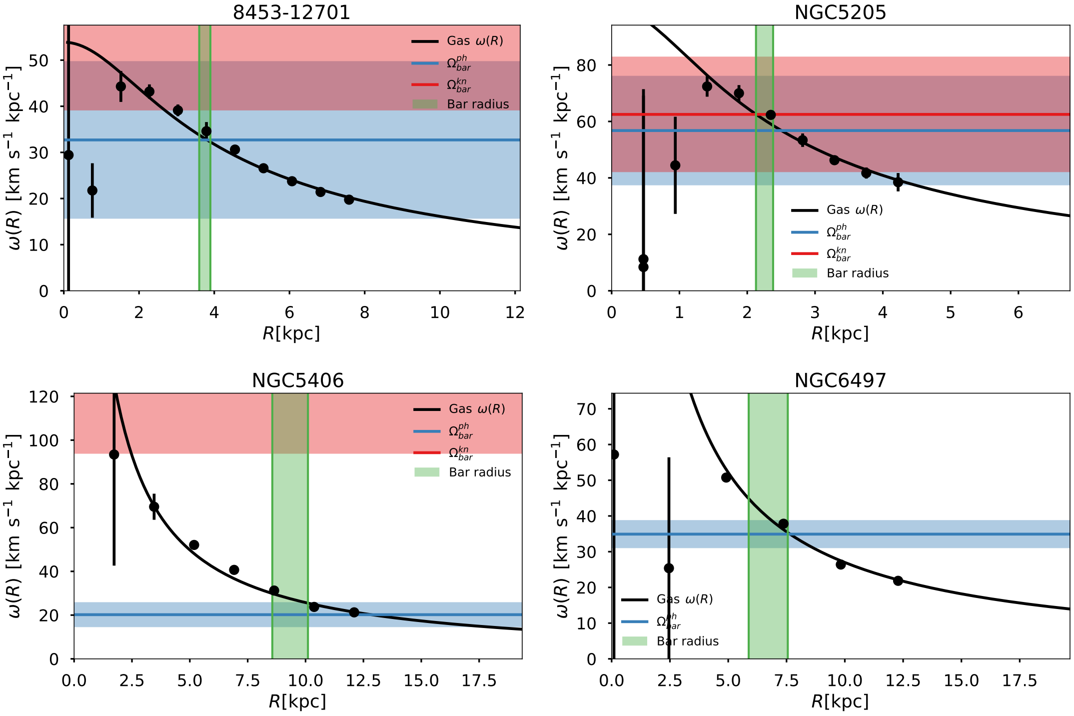

Figure 15: Angular velocity curve for our sample obtained from the *velfit* model. The blue and red lines show the values of Ω_{bar}^{ph} and Ω_{bar}^{kn} respectively. The blue and red regions show their uncertainties after adding in quadrature all sources of error. The green region shows the deprojected bar radius.

The exact value of R_{CR} depends on the shape of the angular rotation curve and the errors in Ω_{bar}. To obtain an accurate value of R_{CR} we performed a Monte Carlo simulation using the uncertainties of Ω_{bar}, gaussianly distributed, and looked for their intersections with the angular velocity curve. Similarly, to obtain the probability distribution of the parameter $\mathcal{R}$, we divided the distribution of R_{CR} with another random gaussian distribution of R_{bar}^{dep}. In Figure 16 we show the resulting probability distribution of $\mathcal{R}$ for all our sample. The area under the curve is coloured depending on the bar classification: ultrafast in green, fast in red, and slow in blue. The black solid line shows the median value of the distribution, and the dashed lines show the $1-\sigma$ dispersion. In Table 5 we show our measurements for R_{CR}, $\mathcal{R}$, and the different probabilities of bar classification.

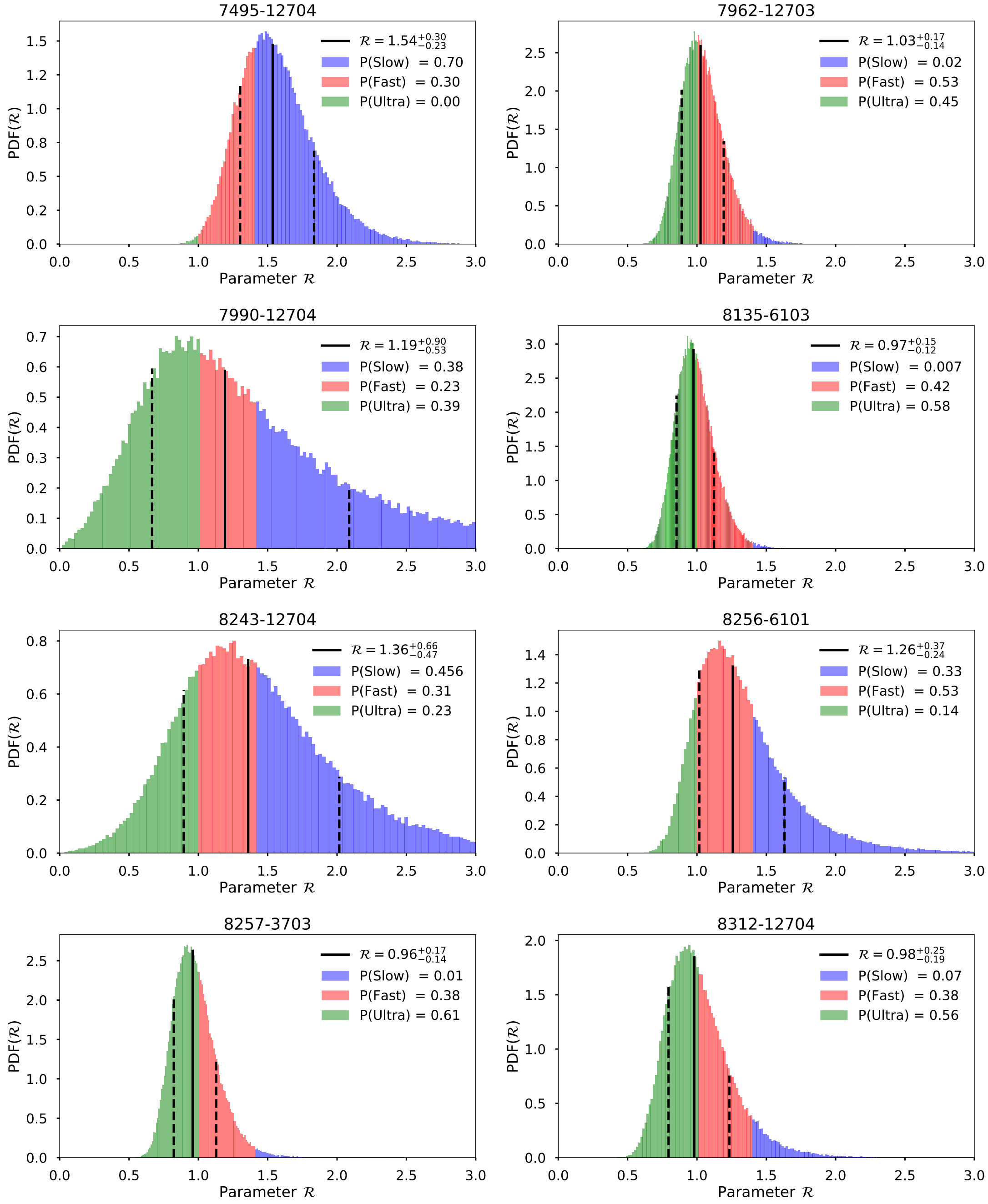
7495-12704
$\mathcal{R} = 1.54^{+0.30}_{-0.23}$
P(Slow) = 0.70
P(Fast) = 0.30
P(Ultra) = 0.00
7962-12703
$\mathcal{R} = 1.03^{+0.17}_{-0.14}$
P(Slow) = 0.02
P(Fast) = 0.53
P(Ultra) = 0.45
7990-12704
$\mathcal{R} = 1.19^{+0.90}_{-0.53}$
P(Slow) = 0.38
P(Fast) = 0.23
P(Ultra) = 0.39
8135-6103
$\mathcal{R} = 0.97^{+0.15}_{-0.12}$
P(Slow) = 0.007
P(Fast) = 0.42
P(Ultra) = 0.58
8243-12704
$\mathcal{R} = 1.36^{+0.66}_{-0.47}$
P(Slow) = 0.456
P(Fast) = 0.31
P(Ultra) = 0.23
8256-6101
$\mathcal{R} = 1.26^{+0.37}_{-0.24}$
P(Slow) = 0.33
P(Fast) = 0.53
P(Ultra) = 0.14
8257-3703
$\mathcal{R} = 0.96^{+0.17}_{-0.14}$
P(Slow) = 0.01
P(Fast) = 0.38
P(Ultra) = 0.61
8312-12704
$\mathcal{R} = 0.98^{+0.25}_{-0.19}$
P(Slow) = 0.07
P(Fast) = 0.38
P(Ultra) = 0.56
PDF($\mathcal{R}$)
Parameter $\mathcal{R}$
0.0
0.5
1.0
1.5
2.0
2.5
3.0

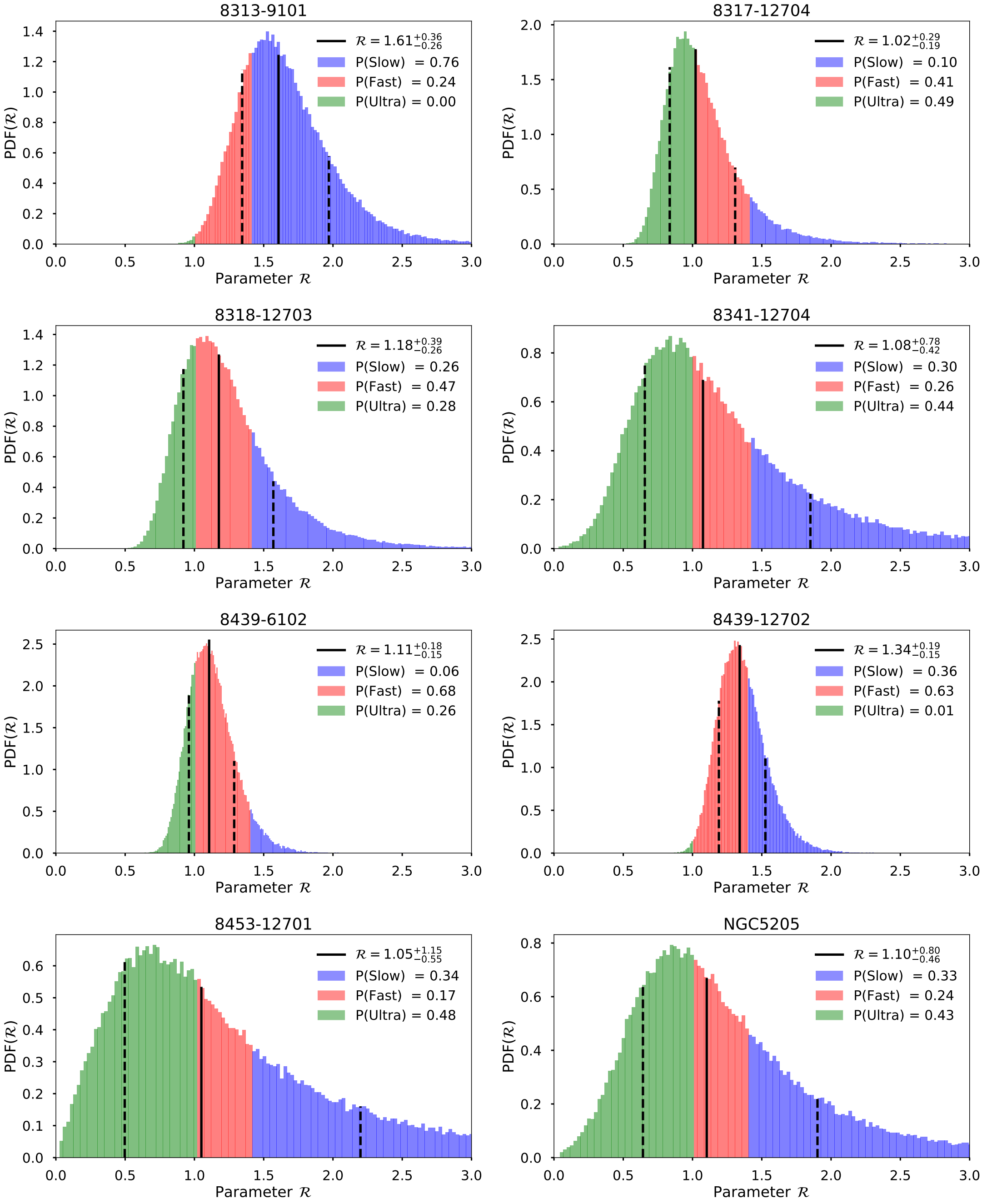
8313-9101
$\mathcal{R} = 1.61^{+0.36}_{-0.26}$
P(Slow) = 0.76
P(Fast) = 0.24
P(Ultra) = 0.00
8317-12704
$\mathcal{R} = 1.02^{+0.29}_{-0.19}$
P(Slow) = 0.10
P(Fast) = 0.41
P(Ultra) = 0.49
8318-12703
$\mathcal{R} = 1.18^{+0.39}_{-0.26}$
P(Slow) = 0.26
P(Fast) = 0.47
P(Ultra) = 0.28
8341-12704
$\mathcal{R} = 1.08^{+0.78}_{-0.42}$
P(Slow) = 0.30
P(Fast) = 0.26
P(Ultra) = 0.44
8439-6102
$\mathcal{R} = 1.11^{+0.18}_{-0.15}$
P(Slow) = 0.06
P(Fast) = 0.68
P(Ultra) = 0.26
8439-12702
$\mathcal{R} = 1.34^{+0.19}_{-0.15}$
P(Slow) = 0.36
P(Fast) = 0.63
P(Ultra) = 0.01
8453-12701
$\mathcal{R} = 1.05^{+1.15}_{-0.55}$
P(Slow) = 0.34
P(Fast) = 0.17
P(Ultra) = 0.48
NGC5205
$\mathcal{R} = 1.10^{+0.80}_{-0.46}$
P(Slow) = 0.33
P(Fast) = 0.24
P(Ultra) = 0.43
PDF($\mathcal{R}$)
Parameter $\mathcal{R}$
0.0
0.5
1.0
1.5
2.0
2.5
3.0

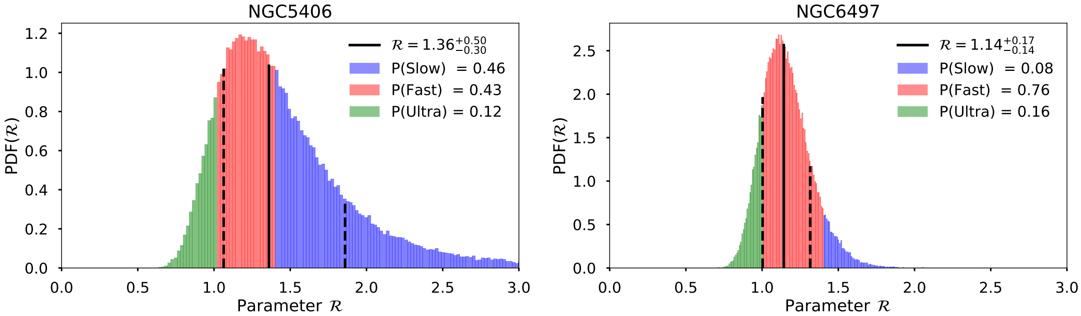

Figure 16: Probability distribution of the Parameter R in our sample. The area under the curve is coloured depending on the bar kinematic classification. The black solid line shows the median, and the dashed lines show the 1-σ deviations.

Table 5: Corotation radius and parameter $\mathcal{R}$ of our sample

Galaxy (1)	R_{CR} [kpc] (2)	$\mathcal{R}$ (3)	P(Slow) (4)	P(Fast) (5)	P(Ultra) (6)
7495-12704	$7.4^{+0.7}_{-0.6}$	$1.5^{+0.3}_{-0.2}$	0.70	0.30	0.00
7962-12703	$16.5^{+1.3}_{-1.2}$	$1.0^{+0.2}_{-0.1}$	0.02	0.53	0.45
7990-12704	$7.6^{+3.8}_{-2.9}$	$1.2^{+0.9}_{-0.5}$	0.38	0.23	0.39
8135-6103	$10.7^{+0.8}_{-0.7}$	$1.0^{+0.1}_{-0.1}$	0.01	0.42	0.58
8243-12704	$4.5^{+1.4}_{-1.1}$	$1.4^{+0.7}_{-0.5}$	0.45	0.30	0.25
8256-6101	$6.2^{+1.1}_{-0.8}$	$1.3^{+0.4}_{-0.2}$	0.33	0.53	0.14
8257-3703	$3.8^{+0.3}_{-0.3}$	$1.0^{+0.2}_{-0.1}$	0.01	0.38	0.61
8312-12704	$6.2^{+0.9}_{-0.7}$	$1.0^{+0.3}_{-0.2}$	0.07	0.38	0.56
8313-9101	$5.4^{+0.8}_{-0.6}$	$1.6^{+0.4}_{-0.3}$	0.76	0.24	0.00
8317-12704	$14.0^{+2.4}_{-1.8}$	$1.0^{+0.3}_{-0.2}$	0.10	0.41	0.49
8318-12703	$7.5^{+1.5}_{-1.1}$	$1.2^{+0.4}_{-0.3}$	0.26	0.47	0.28
8341-12704	$5.2^{+2.3}_{-1.5}$	$1.1^{+0.8}_{-0.4}$	0.30	0.26	0.44
8439-6102	$5.0^{+0.3}_{-0.3}$	$1.1^{+0.2}_{-0.1}$	0.06	0.68	0.26
8439-12702	$8.0^{+0.7}_{-0.6}$	$1.3^{+0.2}_{-0.2}$	0.36	0.63	0.01
8453-12701	$3.4^{+2.7}_{-1.9}$	$1.1^{+1.1}_{-0.6}$	0.34	0.17	0.48
NGC5205	$2.5^{+1.1}_{-0.8}$	$1.1^{+0.8}_{-0.5}$	0.33	0.24	0.43
NGC5406	$12.6^{+2.8}_{-2.0}$	$1.4^{+0.5}_{-0.3}$	0.46	0.43	0.12
NGC6497	$7.6^{+0.6}_{-0.5}$	$1.1^{+0.2}_{-0.1}$	0.08	0.76	0.16

Col.(1) Galaxy ID. Col.(2) Corotation radius. Col.(3) Parameter $\mathcal{R}$. Col.(4) Slow bar probability. Col.(5) Fast bar probability. Col.(6) Ultrafast bar probability

In Figure 17 we show R_{CR} vs. R_{bar}^{dep} of our sample and the division between the slow, fast and ultra-fast rotating bars. Each galaxy is coloured according to their most probable value. Using the median value of the $\mathcal{R}$ distribution our sample is composed of 2 slow, 13 fast and 3 ultrafast bars. However in all cases we cannot rule out other interpretations. In fact we can only classify 4 galaxies with probabilities greater than

$1-\sigma$ ($P > 0.683$): manga-7495-12704 and manga-8313-9101 as a slow bars, 8439-6102 and NGC6497 as fast bars. The mean value of $\mathcal{R}$ in our sample is 1.17, and the standard deviation is 0.17.

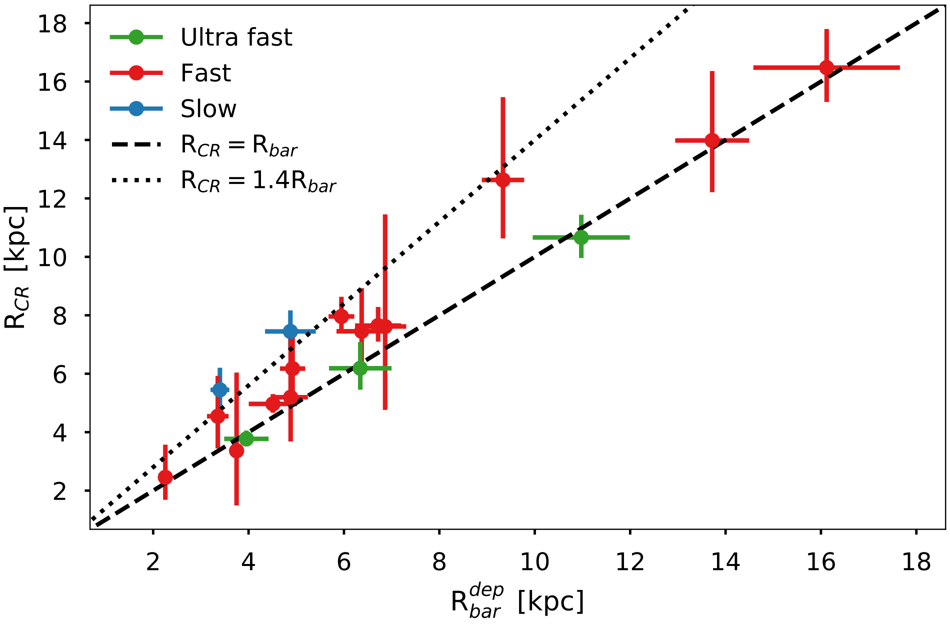

Figure 17: Corotation radius vs. deprojected bar radius of our sample. The segmented line shows the division between fast and ultrafast bars, which are illustrated with red and green points respectively. The dotted line shows the division between fast and slow bars, where the latter are shown with blue dots.

Capítulo 5

Discussion

5.1. Photometric vs kinematic PA

The sensibility of the TW method to the PA, lead us to estimate this quantity with two different methods. (1) The traditional approach, which consist of performing an isophote analysis and observing the orientation and shape of the outermost isophotes. (2) A kinematic approach were we fit the ZLV to the stellar velocity maps. However in our sample, we found examples were both methods are not always reliable.

The photometric PA failed to give meaningful results in the cases of manga-8135-6103 and manga-8243-12704, since Ω_{bar}^{ph} did not intersect the angular velocity curve at any radius. The case of manga-8135-6103 is easily explained by its prominent spiral arms, that extend to the outermost radius and bais the measurement.

The case of manga-8243-12704 is more complex. In principle the TW method should not work for this galaxy since the difference between PA_{bar} and PA_{ph} is just 6.3°, causing the asymptotic behaviour in Figure 12. However, when using the kinematic PA the difference increases to 16.2°, which is well suited for the TW method. It is not clear what causes the difference between PA$_{ph}$and PA$_{kn}$, however we decided to include this galaxy in our sample since the kinematic result predicts a fast rotating bar, that does make physical sense.

On the other hand, the galaxies manga-8341-12704, manga-8453-12701, NGC5406 and NGC6497 have problems using the kinematic orientation. In particular manga-8341-12704 and manga-8453-12701 are two cases with low inclinations at $i = 23.3°$ for the former and $i = 39.9$ for the later. At low inclinations the kinematic information is lost, making PA$_{kn}$more uncertain. The velocity map of manga-8453-12701 also appears to be richer in substructure. This could be due the non-axisymmetric motions the spiral arms and a possible ring that can be seen in the SDSS post-stamp image. Another possibility is the low S/N ratio this particular galaxy has. In order to achieve the goal of 50 S/N ratio, the binning used by Pipe3D could be producing a more lumpy map. This rich substructure is probably also the reason this galaxy has the greatest psudo-slit length error in the sample. Finally, every CALIFA galaxy presents the same problem: the velocity map, produced by Pipe3D shows a lot of substructure and wiggles, probably due the segmentation used, or the lower spectral resolution in comparison with MaNGA. Using a Voronoi segmentation and a penalized pixel-fitting (pPXF) (Cappellari & Emsellem, 2004) could provide a better velocity map to determine PA$_{kn}$in these cases, however this is beyond the scope of this thesis and will be treated in the future. Understanding how the kinematic PA changes at different radius in barred galaxies could provide some light on how these differences arise.

There are two other galaxies where the difference in PA is significant, however both values for Ω_{bar} intersect the angular velocity curve. The first one is manga-7990-12704 which has a difference of $\Delta PA = 6.3°$, however this particular galaxy has one of the smallest PA error. Nonetheless, Ω_{bar}^{kn} predicts an ultra-fast rotating bar which is physically unlikely. The case of manga-8256-6101 is interesting; it has a $\Delta PA = 8.6°$, however the sign of Ω_{bar} changes abruptly between both PA's.

5.2. Comparing the CALIFA results

The main objective of re-analysing a subsample of 3 CALIFA galaxies was to find any systematic errors in our procedure and to compare with the results obtained by Aguerri et al. (2015). There are three main difference in our procedure. The first one is the procedure to determine the TW integrals. As we explained in Chapter 3 we used the stellar flux and stellar velocity maps from Pipe3D, and integrate over them. In contrast, Aguerri et al. (2015) used two different approaches to determine the photometric integral: integrating over a flux map obtained by summing the flux of the datacube at 4575 $\AA$ in a wavelength window of 150 $\AA$, and integrating over mass maps obtained with the fossil record method. They also used two different approaches for the kinematic integral: integrating over velocity maps produced with the penalised pixel-fitting method (pPXF) (Cappellari & Emsellem, 2004), and performing a weighted sum of the spectra along the psudo-slits and then analyse it with the pPXF method. Thus in total, they got four different values for Ω_{bar}.

The second difference comes from the determination of R_{CR}. Aguerri et al. (2015) first determined $V_{c,flat}$ using the stellar-streaming velocity along their photometric major axis and corrected for the asymmetric drift. Then $R_{CR} = V_{c,flat}/\Omega_{bar}$. However this procedure assumes R_{CR} lies in the region where the rotation curve has flatted.

The third difference is the number of psudo-slits used. We tried to fill the bar region with psudo-slits as described in 3.2. Aguerri et al. (2015) used three or five psudo-slits separated by two spaxels to prevent the use of repeated information. However this difference only changes slightly the fitting error.

Finally, there are slight differences in the measurement of the PA. In table 6 we show our measurements of $\mathcal{R}_{ph}$ and $\mathcal{R}_{kn}$ and compare with the ones obtained by them. We also show the difference in PA.

In general our results, predict slower bars than those measured by Aguerri et al. (2015), and our best match ocurrs with $\mathcal{R}_3$. Nonetheless, our results agree within the

Table 6: Comparison of the parameter $\mathcal{R}$ with Aguerri et al. (2015)

Galaxy (1)	$\mathcal{R}_{ph}$ (2)	$\mathcal{R}_{kn}$ (3)	$\mathcal{R}_1$ (4)	$\mathcal{R}_2$ (5)	$\mathcal{R}_3$ (6)	$\mathcal{R}_4$ (7)	PA$_{ph}$ [°] (8)	PA [°] (9)
NGC5205	$1.1^{+0.8}_{-0.5}$	$1.0^{+0.7}_{-0.4}$	$0.6^{+0.2}_{-0.1}$	$0.7^{+0.2}_{-0.1}$	$0.9^{+0.3}_{-0.2}$	$0.7^{+0.1}_{-0.1}$	-10.3 ± 1.5	-9.9 ± 1.6
NGC5406	$1.4^{+0.5}_{-0.3}$	-	$0.7^{+0.6}_{-0.2}$	$0.5^{+0.2}_{-0.1}$	$1.4^{+1.5}_{-0.6}$	$1.3^{+0.7}_{-0.4}$	-67.1 ± 0.7	-62.8 ± 0.8
NGC6497	$1.1^{+0.2}_{-0.1}$	-	$0.4^{+0.1}_{-0.1}$	$0.3^{+0.1}_{-0.1}$	$0.6^{+0.2}_{-0.1}$	$0.5^{+0.1}_{-0.1}$	-70.3 ± 0.7	-68.0 ± 0.4

Col.(1) Galaxy ID. Col.(2) This work, photometric $\mathcal{R}$ Col.(3) This work, kinematic $\mathcal{R}$ Col.(4) Aguerri, light-weight and velocity maps Col.(5) Aguerri, light-weight and summed spectra. Col.(6) Aguerri, mass-weight and velocity maps Col.(7) Aguerri, mass-weight and summed spectra. Col.(8) This work, photometric PA. Col.(9) Aguerri, photometric PA

error bars, except for NGC6497, were we obtain a fast bar, in comparison with them who obtain an ultrafast in all their measurements. Its not clear what causes this difference. It cannot be attributed to the PA difference, since at their orientation we obtain an even slower bar (see in Figure 12).

5.3. The PA error

The PA error is one of the most important error sources of the TW method. Recognized by Debattista (2003), an error of 5 % can produce an error of ≈ 50 % in Ω_{bar}. Luckily, the uncertainties in PA are much smaller. The mean error from the isophote analysis in our sample is $\approx 1.3°$, taking into account the intrinsic errors of the *Ellipse* routine, and the dispersion over the region we used to measure. This PA error accounted for ≈ 12 % of relative error in Ω_{bar} in our sample.

As we saw in Figure 12 in section 4.1.2, Ω_{bar} can tend to an asympthote at certain orientations, and in some cases can change sign abruptly while keeping the same magnitude. Asympthotes, seem to occur at orientations where the PI becomes symmetrical. This happens when the pseudo-slits are oriented towards any of the axes of the bar.

The sign change is more complex, and we do not have a clear answer to explain this behaviour. In the case of manga-8256-6101 the change of signs seems to be related to the bar being close to the semi-minor axis of the disc. When this happens the center of the slits can change sign in velocity and consequently the whole pseudo-slit. However this does not happen in other galaxies. Another possibility could be that the outermost pseudo-slits stop weighting the bar contribution when changing their orientation. This could be the case in galaxies like manga-8317-12704 or NGC5406. Changing the number of pseudo-slits at different orientations, depending on how the bar region is filled could potentially solve this problem, and should be tested in a future work.

5.4. The centering error

In principle, the even parity of the surface brightness makes the TW method insensitive to the centering errors. To test if this was the case for our sample, we repeated the measurement of the TW integrals 1000 times using changing slightly the center of the slits. We used a random radius with a Gaussian distribution with $\sigma = 1$spaxel and a random angle with a uniform distribution.

After fitting Ω_{bar} with a error weighted least square, we found that this error was comparable in magnitude with the PA error and the psudo-slit length error, accounting for $\approx 10\,\%$ of relative error in Ω_{bar}. However, the only cases where this error was dramatic (accounting for $> 15\,\%$ of the relative error) was when the pseudo-slits were oriented close to an asymptote in the $\Omega_{bar} vs.$PA diagram. In those cases, the PA error was also significant.

A different focus can be used to test the centering error. Instead of fitting a single Ω_{bar} using the TW integrals with different dispersions, we could fit Ω_{bar} for every random center, and look at the dispersion of Ω_{bar}. If the only difference between different centres is the zero-point of the relation, then the centring error should be smaller, potentially being neglectful as the theory says. However, this test will be performed in a future work.

5.5. The length error

In section 4.1.3 we found empirically that the pseudo-slit length error is less important for galaxies with $L_0/R_{bar} > 1.7$. Meanwhile, galaxies with smaller ratio seem to be more sensible to this error. In those galaxies, reducing the pseudo-slit length probably makes the TW integrals miss non-axisymmetric contributions from the bar, changing the measurement of Ω_{bar}.

However not all galaxies with $L_0/R_{bar} > 1.7$ have small errors. Considering the TW integrals cancel out the axi-symmetric disc, is possible that some pseudo-slits are weighting non-axisymmetric contributions from other sources, like spiral arms, rings or local perturbations. This is potentially the cause that manga-8453-12701 has the greatest error as we discuss in Section 5.1. Another possibility comes from the psuedo-slits orientation. If these are not aligned correctly with the disc PA, the TW integrals do not cancel out the axisymmetric contribution and can produce an artificial pattern speed like we showed in Figure 2. If that is the case, increasing the psudo-slits length could amplify this error.

Is difficult to estimate the real uncertainty this error could produce. For simplicity, we choose to estimate this error by using the relative error when cutting the pseudo-slits to 80 % of their maximum length. This accounted for ≈ 10 % of error in Ω_{bar}. Our sample is probably not big enough to make a clear cut, but for future works, we suggest using pseudo-slits whose lengths is closer to the ratio $L_0/R_{bar} \approx 2$. Using mass maps in late type galaxies could also potentially reduce this error, since the contribution from spiral arms is diluted.

5.6. Bar classification

According to the median value of $\mathcal{R}$, in our sample we have 2 slow ($\mathcal{R} > 1.4$), 13 fast ($1 < \mathcal{R} < 1.4$) and 3 ultra fast ($\mathcal{R} < 1$) bars. Ultra fast bars theoretically should not exist since the stellar orbits become chaotic and unstable beyond R_{CR} (Contopoulos & Papayannopoulos, 1980). However all our ultra fast bars are close to $\mathcal{R} = 1$ and their uncertainties are consistent with them being fast bars rotating up to their R_{CR}. Classifying galaxies with the adimensional parameter $\mathcal{R}$ can be sometimes misleading, since in absolute terms, a slow bar in a small galaxy could have a greater Ω_{bar} than a fast or ultrafast bar in a bigger galaxy.

Numerous N-body and hydrodynamical simulations have shown that as the bar evolves, the exchange of angular momentum with the different components slows down the bar. In the process the bar becomes longer and stronger. In Figure 18, we show Ω_{bar} vs R_{bar}^{dep} of our sample, without rescaling. A clear trend can be seen, where as the bars become longer, the bar slows down, independently of the bar classification. These results are similar to those presented by Font et al. (2017) suggesting large bars can only rotate with low Ω_{bar} while short bars can rotate fast and slow.

Previous works using N-body and hydrodinamical simulations have suggested that early-type galaxies should host fast bars, while late-type should be slow (Combes & Elmegreen, 1993; Rautiainen et al., 2008). Figure 19 shows the parameter $\mathcal{R}$ against the morphological type of our sample. Our results however are in agreement with Aguerri et al. (2015) since we do not see a clear trend with the morphological type.

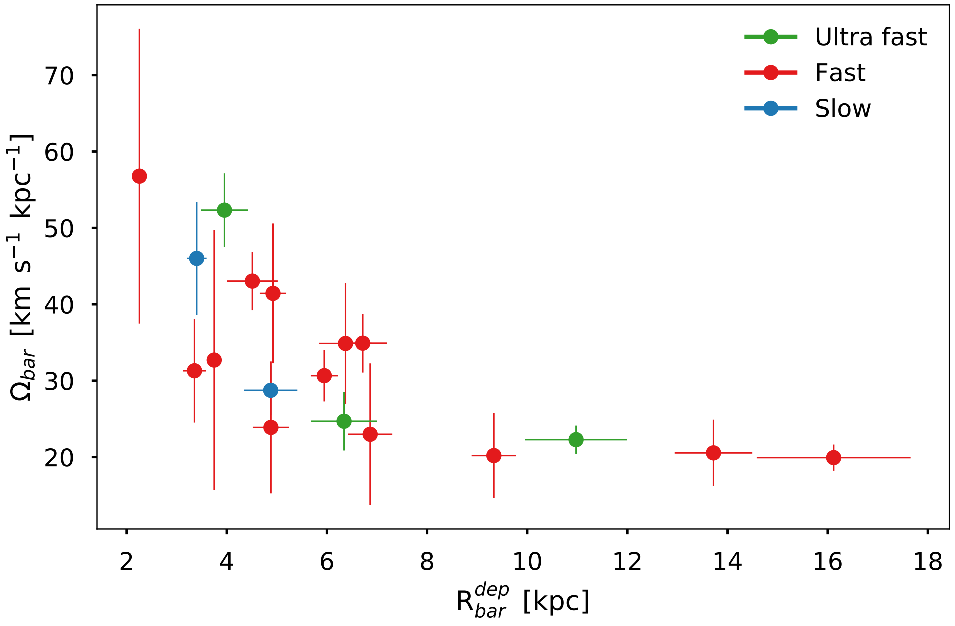

Figure 18: Bar pattern speed vs. deprojected bar radius of our sample.

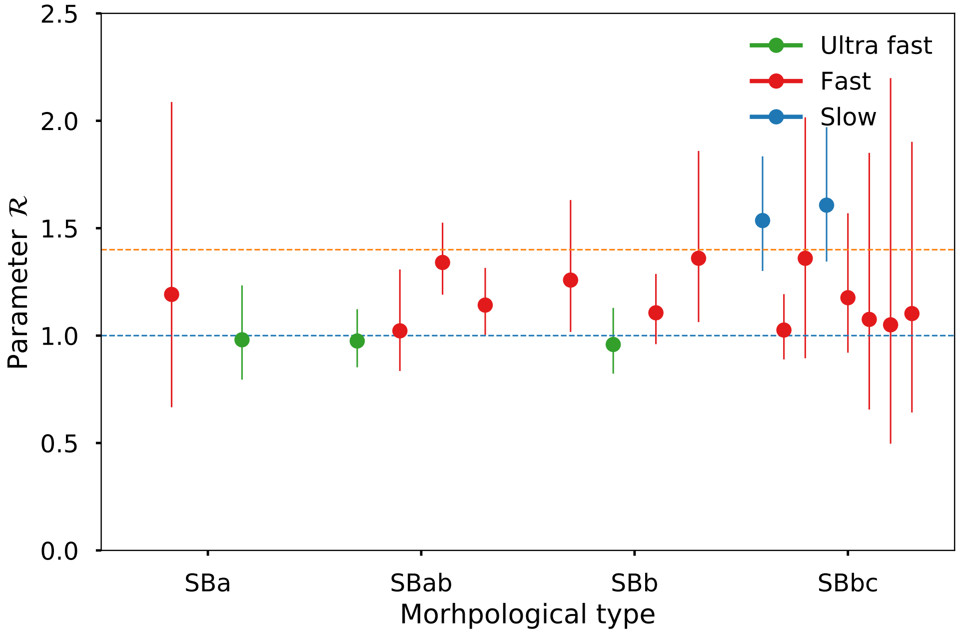

Figure 19: Bar pattern speed vs. deprojected bar radius of our sample.

Capítulo 6

Conclusions

In this thesis we have used the TW method to determine Ω_{bar} for a sample of 15 MaNGA galaxies and 3 CALIFA galaxies. To achieve this, we required the use of various tools:

- **Pipe3D** allowed us to disentangle the spectra of MaNGA and CALIFA and recover stellar flux and velocity maps, where we performed the TW integrals.
- **Ellipse** was used to recover the geometric parameters from our sample. These include R_{bar}, R_{bar}^{dep}, ϵ_d and PA$_{ph}$.
- **Velfit** was used to model the rotation curves from the H_{alpha} velocity maps, taking into account the non-axisymmetric motions produced by the bars. This rotation curves were used to determine the R_{CR}, and classify our sample as slow, fast or ultrafast rotators.

We identified three main sources of error, all of which arise from the geometric nature of the TW method: the PA error ($\delta\Omega_{PA}$), the centering error ($\delta\Omega_{Cen}$) and the slit length error ($\delta\Omega_{Len}$). We performed various test to estimate and constrain the relative error of each source.

- **The PA error:** A well known source of error for the TW method. To estimate this error we studied the behaviour of Ω_{bar} as a function of the PA in an interval that contains both PA$_{ph}$and PA$_{kn}$. This error behaves differently for each galaxy. In some cases Ω_{bar} tends to an asymptote, whereas in some cases can change sign abruptly. The former is caused when the photometric integral becomes symmetrical, specially when the pseudo-slits are oriented towards a bar axes. The later is more difficult to explain. It could be caused when the pseudo-slits are perpendicular to PA_{bar}, or by the number of pseudo-slits being kept constant at different orientations. In our sample, this was the dominant source of uncertainty accounting for $\approx 10.5\,\%$ of the error in Ω_{bar}.
- **The centering error:** An error that in principle the TW method should be insensitive. We test this by repeating the TW integrals 1000 times changing the

center slightly, using a random radius with a 2D gaussian distribution with $\sigma =$ 1spaxel. Then we fitted a the median values of the TW integrals using a weighted least squares. Surprisingly, this accounted for $\approx 9\,\%$ of the uncertainty in Ω_{bar}. In general this error is small and only becomes important when the pseudo-slits are close to an asymptote in the Ω_{bar}vs.PA diagram, where the PA error also increases drastically. Thus, these two errors are correlated.

- **The psudo-slit length error:** A systematic error we should take into account due the limited spatial extension of MaNGA. Empirically we found this error is dependant in the ratio L_0/R_{bar}. For galaxies where $L_0/R_{bar} > 1.7$ the error is less important. For galaxies where $L_0/R_{bar} < 1.7$ the TW integrals do not weight all the non-axisymmetric contributions of the bar affecting the measurement of Ω_{bar}. Finally, in some galaxies where $L_0/R_{bar} > 1.7$ the TW integrals could be weighting other non-axisymmetric contributions from spiral arms, rings or local perturbations. Also, if the PA is erroneous, the axisymmetric disc do not cancel out and creates a fictitious Ω_{bar}. For simplicity we estimate this error using the relative error when cutting the pseudo-slits to $80\,\%$ of their maximum length. This accounted for $\approx 10\,\%$ of error in Ω_{bar}

Measuring the PA with two different methods we found that neither PA$_{ph}$nor PA$_{kn}$are always reliable.

- The photometric PA could give an erroneous orientation if the isophotes are bias by prominent spiral arms, companion galaxies or other structures, which was the case for manga-8135-6103.
- The PA$_{kn}$is more uncertain in galaxies with low inclination, due the poor kinematic information.
- In general the kinematic orientation give us less realistic measurements for Ω_{bar}, probably due the perturbations of the bar itself. However it was useful in the two cases where the photometric orientation failed.

Comparing our results with those obtained by Aguerri et al. (2015), we found a good agreement with their $\mathcal{R}_3$, where they weight using mass maps and integrate over their velocity maps. However in the case of NGC6497 we found a fast bar while they obtained an ultrafast. To this moment, it is not clear what could be causing this difference.

Classifying our bars using the median value of the $\mathcal{R}$ distribution we have 2 slow, 13 fast and 3 ultrafast bars without a clear trend between different Hubble morphologies. However with the current uncertanties all our bars are consistent with other interpretations. Only 3 galaxies can be classified with a probability higher than $1-\sigma$: (1) manga-8313-9101 as a slow bar, (2)manga-8439-6102 and (3)NGC6497 as fast bars.

Finally, there are still various projects and ideas that could be applied in future projects:

- Include measurements of the bar strength into the analysis

- An study for the change of the kinematic PA in barred galaxies could provide a better constrain for estimating the PA in galaxies where the photometry fails.
- Apply the TW method to estimate the spiral pattern speed.
- Apply the TW method in dwarf galaxies and weak bars, in search for more slow bars.
- A comparison of applying the TW method using stellar flux, stellar mass or gas flux maps.
- Some of the errors we found could behave differently by changing some details in our test as we described in 5.

Bibliografía

Abraham, R. G., & Merrifield, M. R. 2000, AJ, 120, 2835 3

Aguerri, J. A. L., Beckman, J. E., & Prieto, M. 1998, AJ, 116, 2136 4

Aguerri, J. A. L., Debattista, V. P., & Corsini, E. M. 2003, MNRAS, 338, 465 3, 4

Aguerri, J. A. L., Elias-Rosa, N., Corsini, E. M., & Muñoz-Tuñón, C. 2005, A&A, 434, 109 1

Aguerri, J. A. L., Méndez-Abreu, J., & Corsini, E. M. 2009, A&A, 495, 491 3, 26

Aguerri, J. A. L., et al. 2015, A&A, 576, A102 v, vi, 4, 11, 26, 60, 61, 63, 66

Aguerri, J. A. L., Muñoz-Tuñón, C., Varela, A. M., & Prieto, M. 2000, A&A, 361, 841 3

Allen, J. T., et al. 2015, MNRAS, 451, 2780 32

Athanassoula, E. 1992, MNRAS, 259, 345 3, 4

Athanassoula, E. 2003, MNRAS, 341, 1179 3

Barden, S. C., & Wade, R. A. 1988, in Astronomical Society of the Pacific Conference Series, Vol. 3, Fiber Optics in Astronomy, ed. S. C. Barden, 113 7

Barrera-Ballesteros, J. K., et al. 2014, A&A, 568, A70 32

Barrera-Ballesteros, J. K., et al. 2015, A&A, 582, A21 32

Begeman, K. G. 1987, Ph.D. thesis, Kapteyn Institute, (1987) 34

Binney, J., & Tremaine, S. 2008, Galactic Dynamics: Second Edition (Princeton University Press) 1, 2, 3

Blanton, M. R., et al. 2017, AJ, 154, 28 7

Bundy, K., et al. 2015, ApJ, 798, 7 7

Buta, R., & Block, D. L. 2001, ApJ, 550, 243 3

Buta, R., & Combes, F. 1996, Fundamentals Cosmic Phys., 17, 95 3, 4

Buta, R. J. 2017, MNRAS, 470, 3819 3

Cappellari, M., & Copin, Y. 2003, MNRAS, 342, 345 19

Cappellari, M., & Emsellem, E. 2004, PASP, 116, 138 60

Cappellari, M., et al. 2007, MNRAS, 379, 418 2

Chemin, L., & Hernandez, O. 2009, A&A, 499, L25 4

Combes, F., & Elmegreen, B. G. 1993, A&A, 271, 391 63

Contopoulos, G., & Papayannopoulos, T. 1980, A&A, 92, 33 3, 4, 63

Corsini, E. M. 2011, Memorie della Societa Astronomica Italiana Supplementi, 18, 23 4

Corsini, E. M., Aguerri, J. A. L., Debattista, V. P., Pizzella, A., Barazza, F. D., & Jerjen, H. 2007, ApJ, 659, L121 4

Corsini, E. M., Debattista, V. P., & Aguerri, J. A. L. 2003, ApJ, 599, L29 4

Courteau, S. 1997, AJ, 114, 2402 35

de Blok, W. J. G. 2005, ApJ, 634, 227 34

Debattista, V. P. 2003, MNRAS, 342, 1194 5, 41, 61

Debattista, V. P., Corsini, E. M., & Aguerri, J. A. L. 2002, MNRAS, 332, 65 4

Debattista, V. P., & Sellwood, J. A. 1998, ApJ, 493, L5 3

Debattista, V. P., & Williams, T. B. 2004, ApJ, 605, 714 4

Drory, N., et al. 2015, AJ, 149, 77 8

Elmegreen, B. G., Elmegreen, D. M., & Hirst, A. C. 2004, ApJ, 612, 191 3

Emsellem, E., et al. 2011, MNRAS, 414, 888 2

Emsellem, E., et al. 2004, MNRAS, 352, 721 32

Emsellem, E., Fathi, K., Wozniak, H., Ferruit, P., Mundell, C. G., & Schinnerer, E. 2006, MNRAS, 365, 367 4

Erwin, P. 2005, MNRAS, 364, 283 3

Erwin, P. 2018, MNRAS, 474, 5372 3

Eskridge, P. B., et al. 2000, AJ, 119, 536 3

Fathi, K., Beckman, J. E., Piñol-Ferrer, N., Hernandez, O., Martínez-Valpuesta, I., & Carignan, C. 2009, ApJ, 704, 1657 4

Fathi, K., Toonen, S., Falcón-Barroso, J., Beckman, J. E., Hernandez, O., Daigle, O., Carignan, C., & de Zeeuw, T. 2007, ApJ, 667, L137 4

Font, J., Beckman, J. E., Epinat, B., Fathi, K., Gutiérrez, L., & Hernandez, O. 2011, ApJ, 741, L14 4

Font, J., et al. 2017, ApJ, 835, 279 4, 63

Fridman, A. M., Afanasiev, V. L., Dodonov, S. N., Khoruzhii, O. V., Moiseev, A. V., Sil'chenko, O. K., & Zasov, A. V. 2005, A&A, 430, 67 32

Gabbasov, R. F., Repetto, P., & Rosado, M. 2009, ApJ, 702, 392 4

Gadotti, D. A., Athanassoula, E., Carrasco, L., Bosma, A., de Souza, R. E., & Recillas, E. 2007, MNRAS, 381, 943 30

Gerssen, J., & Debattista, V. P. 2007, MNRAS, 378, 189 4

Gerssen, J., Kuijken, K., & Merrifield, M. R. 1999, MNRAS, 306, 926 4

Hernandez, O., Wozniak, H., Carignan, C., Amram, P., Chemin, L., & Daigle, O. 2005, ApJ, 632, 253 4

Hernquist, L., & Mihos, J. C. 1995, ApJ, 448, 41 3

Hubble, E. P. 1926, ApJ, 64 1

Hunter, J. H., Jr., England, M. N., Gottesman, S. T., Ball, R., & Huntley, J. M. 1988, ApJ, 324, 721 4

Ibarra-Medel, H. J., et al. 2016, MNRAS, 463, 2799 19

Jedrzejewski, R. I. 1987, MNRAS, 226, 747 17

Jin, Y., et al. 2016, MNRAS, 463, 913 32

Jogee, S., et al. 2004, ApJ, 615, L105 3

Kent, S. M. 1987, AJ, 93, 1062 4

Kormendy, J., & Kennicutt, R. C., Jr. 2004, ARA&A, 42, 603 3

Krajnović, D., et al. 2011, MNRAS, 414, 2923 32

Laine, S., Shlosman, I., Knapen, J. H., & Peletier, R. F. 2002, ApJ, 567, 97 3

Laurikainen, E., & Salo, H. 2002, MNRAS, 337, 1118 3

Laurikainen, E., Salo, H., & Buta, R. 2005, MNRAS, 362, 1319 3

Law, D. R., et al. 2016, AJ, 152, 83 8

Lindblad, P. A. B., & Kristen, H. 1996, A&A, 313, 733 4

Marinova, I., & Jogee, S. 2007, ApJ, 659, 1176 3, 26

Martin, P. 1995, AJ, 109, 2428 3

Martinet, L., & Friedli, D. 1997, A&A, 323, 363 3

Martinez-Valpuesta, I., Shlosman, I., & Heller, C. 2006, ApJ, 637, 214 3

Martinsson, T. P. K., Verheijen, M. A. W., Westfall, K. B., Bershady, M. A., Schechtman-Rook, A., Andersen, D. R., & Swaters, R. A. 2013, A&A, 557, A130 35

Melvin, T., et al. 2014, MNRAS, 438, 2882 3

Méndez-Abreu, J., Sánchez-Janssen, R., Aguerri, J. A. L., Corsini, E. M., & Zarattini, S. 2012, ApJ, 761, L6 3

Menéndez-Delmestre, K., Sheth, K., Schinnerer, E., Jarrett, T. H., & Scoville, N. Z. 2007, ApJ, 657, 790 3

Merrifield, M. R., & Kuijken, K. 1995, MNRAS, 274, 933 4, 5

Michel-Dansac, L., & Wozniak, H. 2006, A&A, 452, 97 26

Ohta, K., Hamabe, M., & Wakamatsu, K.-I. 1990, ApJ, 357, 71 3

Patsis, P. A., Skokos, C., & Athanassoula, E. 2003, MNRAS, 346, 1031 4

Planck Collaboration, et al. 2016, A&A, 594, A13 9

Puerari, I., & Dottori, H. 1997, ApJ, 476, L73 4

Rand, R. J., & Wallin, J. F. 2004, ApJ, 614, 142 4

Rautiainen, P., & Salo, H. 2000, A&A, 362, 465 3, 4

Rautiainen, P., Salo, H., & Laurikainen, E. 2008, MNRAS, 388, 1803 4, 63

Rhee, G., Valenzuela, O., Klypin, A., Holtzman, J., & Moorthy, B. 2004, ApJ, 617, 1059 34

Rogstad, D. H., Lockhart, I. A., & Wright, M. C. H. 1974, ApJ, 193, 309 34

Roth, M. M., et al. 2005, PASP, 117, 620 8

Samet, H. 1984, ACM Comput. Surv., 16, 187 19

Sánchez, S. F., et al. 2016a, A&A, 594, A36 8

Sánchez, S. F., et al. 2012, A&A, 538, A8 8

Sánchez, S. F., et al. 2016b, ArXiv e-prints 17, 19

Sánchez, S. F., et al. 2015, ArXiv e-prints 17, 19

Sánchez-Menguiano, L., Pérez, I., Zurita, A., Martínez-Valpuesta, I., Aguerri, J. A. L., Sánchez, S. F., Comerón, S., & Díaz-García, S. 2015, MNRAS, 450, 2670 4

Sanders, R. H., & Tubbs, A. D. 1980, ApJ, 235, 803 4

Schoenmakers, R. H. M., Franx, M., & de Zeeuw, P. T. 1997, MNRAS, 292, 349 34

Schwarz, M. P. 1981, ApJ, 247, 77 3, 4

Sellwood, J. A. 2014, Reviews of Modern Physics, 86, 1 3

Sellwood, J. A., & Sánchez, R. Z. 2010, MNRAS, 404, 1733 17, 34

Sellwood, J. A., & Wilkinson, A. 1993, Reports on Progress in Physics, 56, 173 3

Sheth, K., et al. 2008, ApJ, 675, 1141 3

Sheth, K., Regan, M. W., Scoville, N. Z., & Strubbe, L. E. 2003, ApJ, 592, L13 3

Smee, S. A., et al. 2013, AJ, 146, 32 7

Spekkens, K., & Sellwood, J. A. 2007, ApJ, 664, 204 v, vi, 17, 34

Swaters, R. A., Madore, B. F., van den Bosch, F. C., & Balcells, M. 2003, ApJ, 583, 732 34

Teuben, P. J., & Sanders, R. H. 1985, MNRAS, 212, 257 3

Tremaine, S., & Weinberg, M. D. 1984, ApJ, 282, L5 v, vi, 4

van den Bosch, F. C., & Swaters, R. A. 2001, MNRAS, 325, 1017 34

Weinberg, M. D. 1985, MNRAS, 213, 451 3

Whyte, L. F., Abraham, R. G., Merrifield, M. R., Eskridge, P. B., Frogel, J. A., & Pogge, R. W. 2002, MNRAS, 336, 1281 3

Wozniak, H., Friedli, D., Martinet, L., Martin, P., & Bratschi, P. 1995, A&AS, 111, 115 3, 26

Yan, R., et al. 2016, ArXiv e-prints 7

Zimmer, P., Rand, R. J., & McGraw, J. T. 2004, ApJ, 607, 285 4

Zou, Y., Shen, J., & Li, Z.-Y. 2014, ApJ, 791, 11 30